22 5/4/81 T. 5

①

R4021

SAND80-1156
Unlimited
UC-25

MASTER

COMPUTATIONAL AND EXPERIMENTAL ANALYSIS OF A U-6w/oNb VACUUM CONSUMABLE ARC REMELTED INGOT - A Progress Report for the Sandia Macrosegregation Study

F. J. Zanner and L. A. Bertram

Prepared by Sandia Laboratories, Albuquerque, New Mexico 87185
and Livermore, California 94550 for the United States Department of
Energy under Contract DE-AC04-76DP00789.

April 1981

Sandia National Laboratories

SF 2900-Q(3-80)

DISTRIBUTION OF THIS DOCUMENT IS UNLIMITED

Issued by Sandia National Laboratories, operated for the United States Department of Energy by Sandia Corporation.

Printed in the United States of America
Available from
National Technical Information Service
U. S. Department of Commerce
5285 Port Royal Road
Springfield, VA 22161
Price: Printed Copy $9.00; Microfiche $3.00

COMPUTATIONAL AND EXPERIMENTAL ANALYSIS OF A U-6w/oNb VACUUM CONSUMABLE ARC REMELTED INGOT*

A Progress Report for the Sandia Macrosegregation Study

F. J. Zanner and L. A. Bertram
Sandia National Laboratories**
Albuquerque, New Mexico 87185

ABSTRACT

A computer code (ZAP) has been developed to simulate the thermodynamic, magnetohydrodynamic, and fluid flow conditions in the liquid and solid-liquid regions of a solidifying ingot during vacuum consumable arc remelting. The code is coupled and constrained with experimentally determined measurements of boundary conditions and melt parameters such as melt rate, melt current, and melt time.

The work reported in this paper is part of an ongoing effort and presents one preliminary step in the coupled experimental-numerical process. A 538 kg U-6w/oNb ingot was remelted to obtain regions of constant melting current of 2 through 6 kA in 1 kA increments. The melt was simulated numerically using inputs for the code that were obtained from this experiment. Results of this numerical simulation are compared to experimental results obtained from ingot radiography and chemical analysis. There is good

---

* This work was supported by the U. S. Department of Energy (DOE) under Contract No. DE-AC04-76-DP00789.
**A U. S. Department of Energy Facility.

qualitative agreement between computed and measured pool volumes and between computed fluid flow and macrosegregation tendency within the experimental range of melting currents.

In addition to discussion of experimental-numerical agreement, a detailed mathematical treatment of the thermal environment, energy budget considerations, electromagnetic conditions, thermophysical properties, equations of motion, and numerical solution procedures are included in the Appendix.

LIST OF ILLUSTRATIONS

		Page
Figure 1:	Schematic Illustration of Vacuum Consumable Arc Remelt Process	58
Figure 2:	Ingot Isometric Illustrating Radiographic and Chemical Sampling Procedures	59
Figure 3:	Image Enhanced Radiograph of Longitudinal Ingot Slice	60
Figure 4:	Melt Rate as a Function of Melting Current	61
Figure 5:	Ingot Growth Rate as a Function of Melting Current	62
Figure 6:	Energy Consumption per kg Melted as a Function of Melting Current	63
Figure 7:	Power Input and Power Loss to the Crucible	64
Figure 8:	Color Enhanced Radiograph Corrected for Nb Concentration	65
Figure 9:	Predicted and Observed Pool Volume as a Function of Melting Current	66
Figure 10:	Average Solute Band Period as a Function of Melting Current	67
Figure 11:	Nb Concentration as a Function of Melting Current for Surface, Midradius, and Center Locations in the Ingot	68
Figure 12:	(A) Photomacrograph of Solute Band Segregation at 3 kA (B) Nb Concentration vs. Distance for a Scan Along Line Shown in (A)	69
Figure 13:	(A) Photomacrograph of Solute Band Segregation at 4 kA (B) Nb Concentration vs. Distance for a Scan Along Line Shown in (A)	70
Figure 14:	(A) Photomacrograph of Solute Band Segregation at 5 kA (B) Nb Concentration vs. Distance for a Scan Along Line Shown in (A)	71

Figure 15: (A) Photomacrograph of Solute Band Segregation at 6 kA 72
(B) Nb Concentration vs. Distance for a Scan Along the Line Shown in (A)

Figure 16: Isotherm Plot for Ingot Section Melted at 6 kA 73

Figure 17: Isotherm Plot for Ingot Section Melted at 5.54 kA 74

Figure 18: Streamfunction Plot for Ingot Section Melted at 5.54 kA 75

Figure 19: Isotherm Plot for Ingot Section Melted at 5 kA 76

Figure 20: Streamfunction Plot for Ingot Section Melted at 5 kA 77

Figure 21: Approach to Steady State as Indicated by Plotting Dimensionless Enthalpy vs. Dimensionless Time for the 5kA Condition 78

Figure 22: Computed Energy Budget for the 5 kA Melting Condition 79

Figure 23: Approach to Steady State as Indicated by Plotting Dimensionless Time for the 4kA Condition 80

Figure 24: Isotherm Plot for Ingot Section Melted at 4 kA 81

Figure 25: Streamfunction Plot for Ingot Section Melted at 4 kA 82

Figure 26: Isotherm Plot for Ingot Section Melted at 3 kA 83

Figure 27: Streamfunction Plot for Ingot Section Melted at 3 kA 84

Figure 28: Isotherm Plot for Ingot Section Melted at 2 kA 85

Figure 29: Streamfunction Plot for Ingot Section Melted at 2 kA 86

Figure 30: Compilation of Computed Energy Budgets as a Function of Melting Current 87

Figure 31: Ingot Centerline Temperature as a Function of Distance from the Pool Surface for Current Levels 2,3,4,5, and 5.5 kA 88

Figure 32: Macrosegregation for U-6w/oNb Nominal Alloy under Conditions of Unidirectional Solidification 89

Figure A1: (A) Schematic Diagram of the Vacuum Comsumable Arc Remelt Process
(B) Cut Away of the Arc Zone 90

Figure A2: Possible Electrode-Thermal Interactions 91

Figure A3: Schematic of Temperature vs. Distance from the Molten Tip for an Electrode at Quasisteady Melt Conditions 92

Figure A4: Electrode Viewfactor from the Pool Surface 93

Figure A5: Schematic of Ingot Centerline Temperature as a Function of Distance from Pool Surface 94

Figure A6: Schematic of Contact Thermal Resistance at the Ingot-Crucible Wall as a Function of Temperature 94

Figure A7: Summary of Thermal Boundary Conditions 95

Figure A8: Current Streamlines for an Aspect of Ratio 1.0 97

Figure A9: Tangent Rule of Phase Equilibria as Shown by a Plot of Free Energy vs. Concentration 98

Figure A10: Calculated U-Nb Equilibrium Phase Diagram 100

Figure A11: Equilibrim Phase Diagram Including Non-equilibrium Solidification of a U-6.3w/oNb Alloy as Derived from the Scheil Equation 101

Figure A12: Enthalpy vs. Temperature 102

LIST OF TABLES

Page

Table I: Melt Parameters - U-6w/oNb Ingot 26

Table II: Solute Band Period Measurements as a Function of Location and Melting Current 27

Table III: Significant Difference Table for Bond Period Measurements as a Function of Location and Melting Current 28

Table IV: Energy Budget Computations 96

Table V: Thermophysical Properties of Uranium and Niobium 99

LIST OF ROMAN SYMBOLS

A,B	Components of binary alloy
A_e, A_I	Cross sectional area of electrode, ingot
A_o	Alfvén number = $(\kappa_o/R)/(B_o/\sqrt{\mu\rho_o})$
B	Dimensionless magnetic induction, azimuthal component
B_o	Reference value of B, = $\mu I_m/(2\pi R)$
C	Weight fraction concentration of solute
C_L, C_s	Weight fraction concentration of solute in liquid, solid phase
C_p	Specific heat; subscripts denote liquid or solid phase, superscripts (H_2O,A,B,U,Nb) denote substance.
C_k	Parameter in curve fit k(T) for thermal conductivity
f_s, f_L	Mass fraction solid, liquid; overscore denotes nonequilibrium cooling
g	Acceleration due to gravity, 9.81 m/s^2
g_s, g_L	Volume fraction solid, liquid
G	Gibbs' free energy; subscripts denote phase, superscripts denote substance
Gr	Grashof number = $g\alpha\Delta T_o R^3/\nu^2$
h	Dimensionless enthalpy; reference value is L/2
I	Radiographic radiation intensity transmitted through specimen
I_o	Radiographic radiation source intensity
I_m	Melt current in VAR furnace
$J_{electrode}$	Nominal current desnity of electrode face = I_m/A_e
J_o, J_1	Bessel functions of order zero, one
k	Thermal conductivity of alloy; subscripts denote phase
k_1	Parameter in viewfactor expressions, = $1 - r^2/R_e^2$

L	Latent heat of fusion of alloy
L_e	Length of electrode with noticeable radiation intensity
$\dot{m}$	Mass melt rate in VAR furnace
$\dot{m}_{H_2O}$	Mass flow rate of cooling water in crucible water jacket
M_{Nb}	Change in alloy absorption coefficient per unit weight percent change in Nb concentration
N	Number of grid points in radial direction; number of data points in sample
P_e	Thermal power deposited on electrode by arc
P_{ingot}	Thermal power deposited in ingot by inflow of molten metal from electrode
P_{loss}	Thermal power deposited on crucible by arc
Pr	Prandtl number, ν_o/κ_o
q	Heat flux at ingot surface
$\dot{Q}_c$	Thermal power conducted out through outflow boundary at bottom of computational grid
$\dot{Q}_{crucible}$	Thermal power removed from system by cooling water = $\dot{m}_{H_2O} C_p^{H_2O} \Delta T_{H_2O}$
$\dot{Q}_{eL}$	Thermal power radiated by electrode lateral surface
$\dot{Q}_{fo}$	Thermal power lost by advection through outflow boundary at bottom of computational grid
$\dot{Q}_{fs}$	Thermal power conducted in through top surface of pool
$\dot{Q}_R$	Net thermal power radiated by portion of pool directly under electrode
F_A, F_b	$\exp\left\{\frac{G_L^A - G_s^A}{RT}\right\}$; similarly for F_B

$\dot{Q}_{RL}$	Net thermal power radiated by portion of pool between electrode edge and wall
$\dot{Q}_w$	Thermal power conducted from ingot to crucible wall
r	Radial cylindrical coordinate
r_k	ratio of thermal conductivities of liquid/solid $= k_L/k_s$
r_ν	Ratio of viscosity at solidus temperature to viscosity at liquidus temperature $= \nu(T_s)/\nu(T_L)$
R, R_e	Radius of ingot, electrode
R_o	Minimum thermal resistance between ingot surface and cooling water
R_T	Thermal resistance between ingot surface and cooling water at temperature T
ΔS_f	Entropy change of fusion
ΔS_m	Entropy change of mixing
t	Thickness of radiographic specimen
t	Dimensionless time; reference value R^2/κ_o
T_a	Temperature of annular portion of pool surface between electrode edge and wall; equal to T_L in present computations
T_I	Immobilization temperature, below which interdendritic liquid flow can no longer carry significant heat
T_L	Liquidus temperature, equilibrium phase diagram
T_m	Maximum temperature in electrode; equal to $T_L + 12.2$ K in present computation
T_o, T_o^*	Reference temperature for dimensionless temperature scale, $= 1/2(T_L + T_s)$ or $1/2(T_L + T_s^*)$
T_p	Temperature of portion of pool surface directly under electrode, $= T_m$ in present computations
T_r	Room temperature, 300K
T_R	Temperature above which ingot makes partial contact with crucible wall

T_{RO}	Temperature above which ingot makes perfect contact with crucible wall
T_s, T_s^*	Solidus temperature of equilibrium, nonequilibrium phase diagram
$T_s(r)$	Function specifying surface temperature boundary condition on pool surface
T_U, T_{Nb}	Melting temperatures of pure U, Nb
T_w	Temperature of bulk cooling water
ΔT_{H_2O}	Temperature rise of cooling water, inlet to outlet
u	Axial component of dimensionless velocity; reference value κ_o/R
U_e, U_I	Linear melt rate of electrode, linear growth rate of ingot
U-6w/oNb	Six weight percent niobium alloy of uranium
v	Radial component of dimensionless velocity, reference value κ_o/R
v*	Viewfactor of electrode face, = $\Omega/2\pi$
$v_\perp$	Velocity component perpendicular to isotherm, positive along $-\nabla T$
w, w*	Atomic fraction of solute in solid, liquid
x	Axial coordinate
$Z_{m,n}$	Significant difference between means of data sets m and n

LIST OF GREEK SYMBOLS

α	Coefficient of thermal expansion (volumetric)
β_1	First zero of zero-order Bessel function; $J_o(\beta_1) = 0$
δ	Depth of penetration of thermal wave into electrode
δ_L	Depth of liquid film on the electrode face
ε	Hemispherical total emittance of U-6w/oNb surface
ζ	Dimensionless vorticity, $= \partial v/\partial x - \partial u/\partial r$
θ	Dimensionless temperature, $= (T - T_o)/[1/2(T_L - T_s)]$
κ_o	Thermal diffusivity at reference temperature
μ	Permeability of free space, $4\pi \times 10^{-7}$ n/A^2
μ_U, μ_{Nb}	Absorption coefficients of uranium, niobium for x-radiation
ν	Kinematic viscosity of liquid alloy, reference value
ρ_o	Reference value of alloy mass density
σ^*	Stefan-Boltzmann radiation constant, 5.67×10^{-8} W/m^2-K^4
$\bar{\tau}$	Average period for concentration band deposition in solidifying ingot
ψ	Stream function of liquid flow
ψ_1	Dimensionless value of streamfunction at ingot surface; also interpretable as Peclet number; $= U_I/(2\kappa_o/R)$
Ω	Solid angle subtended by electrode face
σ	Standard deviation of data set

TABLE OF CONTENTS

Page

Introduction 1

Experimental Procedures 3

Experimental Results

A. Melt Parameters 5

B. Ingot Analysis 6

Code Simulation

A. Numerical Model 8

B. Simulation Results 12

Discussion 16

Conclusions 22

Future Work 23

Acknowledgements 24

Appendix I - Data Tables 26

Appendix II - Mathematical Treatment for Evaluation of Absorption Coefficients to Obtain Nb Concentration Directly from Radiographs 29

Appendix III

Thermal Environment 32

Energy Budget Considerations 40

Electromagnetic Conditions 41

Thermophysical Properties 42

Equations of Motion 50

Numerical Solution Procedures 53

References 56

INTRODUCTION

Vacuum consumable arc remelting is a process used to control the solidification of segregation sensitive alloys. This is accomplished by manipulation of the system thermodynamics in a manner such that the advancing solidification region has an abundant supply of liquid metal while simultaneously minimizing local solidification time. Energy is added to the system by means of a vacuum arc and the internal distribution of this energy within the system influences melt rate, fluid flow within the molten pool, and the volume of the molten pool.

A schematic illustration of this melting process is shown in Figure 1. In general a direct current electrical potential is imposed across the electrode and ingot (the electrode is negative and the ingot is at ground) and a vacuum arc is established in an evacuated chamber. Metal is slowly melted from the electrode tip and deposited in a molten pool atop the ingot. Since the electrode is smaller in diameter than the ingot the electrode must be driven down to maintain a constant electrode gap. As a result, this process functions in a moving coordinate system. Since arc temperatures are high, direct measurements within the arc and molten pool are extremely difficult to obtain.

Because of these experimental constraints a mathematical modeling program has been underway at Sandia National Laboratories to simulate the thermodynamic, magnetohydrodynamic and fluid flow conditions ahead of and within the solid-liquid region of the solidifying ingot. This research effort involves both melting experiments (1,2) and computer modeling (3) with the goal of determining the influence of melt parameters on the homogeneity of the resulting ingot. The intent of this strategy is to constrain the computer code (ZAP) with experimentally determined boundary conditions and to use this code to design more productive experiments. Experimental verification of the simulation is accomplished by a number of indirect means including radiography, high speed photography, and chemical analysis.

The work contained in this progress report is part of that on-going effort and presents the first step in the coupled experimental-numerical process (see also (4)).

Specifically this report discusses the results of an experiment conducted at Union Carbide's Y-12 facility in which a standard U-6w/oNb production ingot was remelted such that four constant current regions were obtained. Experimentally determined values of melt rate as a function of melting current are used as inputs for the code. The results of the code calculations are compared to ingot post mortem radiographic and chemical evaluations.

This technique seems to be yielding qualitatively acceptable results; however, the present first step of the program represents an incomplete initial look at the internal conditions in the vacuum consumable arc remelt ingot. For easily-understood reasons, the numerical simulation is not yet quantitatively accurate. Further experimental measurements and refinements of the model will be required before a sharply focused picture of the internal conditions can be obtained.

Reporting begins with a section on experimental procedures and this section contains a description of the melting experiments and the techniques used for evaluation of these experiments. Next the experimental results are presented in two sub-sections: one related to melt parameters and the other to ingot evaluation. Following is a section on code simulation. The numerical model is developed with reference to extensive appendices and the model is then used to produce simulation results. Discussion of both the experimental and numerical results is presented in the next section. Lastly, the conclusions, plans for future work, and acknowledgements are presented.

Experimental Procedures

A. Melting

A standard Y-12, 0.156 m dia., 1.66m long U-6w/o Nb cast electrode was remelted at Y-12 into a 0.211m dia., 0.889m long, 538 kg ingot. Crucible water flow was maintained at $5.96 \times 10^{-3} m^3 s^{-1}$. Crucible water in/out temperatures, electrode position (ram travel), and nominal current and voltage were monitored every 120s. Electrode gap was determined at the end of each constant current interval by driving the electrode to a dead short and recording the amount of travel.

The arc was struck at 5kA and melting continued at this level for 198s. Melting current was then raised to 6kA and 0.267m of ingot was deposited to establish steady state thermal conditions. The melting time at 6 kA was about 2000s, (about four conductive diffusion times for the ingot) to permit attainment of certain quasisteady conditions. Melting continued at 6kA for the next 0.011m of ingot under quasisteady conditions and then the current was decreased in 1kA increments to obtain constant current regions of 0.138m, 0.146m, 0.164m and 0.064m at 5kA, 4kA, 3kA, and 2kA, respectively. Based on conductive diffusion times the 3kA case was quasisteady, the 4kA and 5kA cases were marginal, and 2kA was definitely unsteady. Each 1kA current reduction was acomplished in approximately 4s. A summary of the melt parameters appears in Table I. (Appendix I, P. 26)

B. Evaluation

Figure 2 illustrates the radiographic and chemical sampling procedures. A longitudinal plate 0.0015m thick was cut from the full length of the ingot along the centerline and two horizontal slices of the same thickness were cut from each constant current region. Five chemistry drillings representing surface (A), mid-radius (B), and center (C), were obtained from one half of the horizontal slices representing each region of constant current. Samples ($0.025m^2$) were also cut from each constant current region of the longitudinal slice (see Figure 2), examined metallographically and with an electron microprobe analyzer.

Each slice was radiographed with a 300kV, 10Ma W source using a pure U step wedge and a U-6w/oNb step wedge as standards for correction of thickness and concentration effects. (Step wedges are wedges with flat steps each having a thickness $2.54x10^{-6}$m different than an adjacent step. The total range of thickness of the steps brackets the thickness range of the radiographic slices.) Source to specimen distance was 1.82m and exposure time was 600s. The thickness of each slice was measured at the intersection of 0.013m grid lines. Radiographic negatives for each slice and step wedge were digitized with a microdensitometer and then these density data along with thickness measurements were analyzed using computerized image enhancement techniques. The use of the step wedges and absorption coefficient correction techniques made it possible to obtain Nb concentration directly from the enhanced radiographs. The mathematical development of this technique is shown in Appendix II. Images obtained by use of these enhancement techniques were used to obtain estimates for molten pool volume, solute band spacing at six locations across the ingot diameter, and general fluid flow trends.

Solute band spacings were measured at each current level along the six lines (±1, ±2, ±3) shown on the enhanced radiograph of Figure 3. Since the vertical growth rate of the ingot was known it was possible to compute the time required to deposit a solute band at each location and current level.

Experimental Results

A. Melt Parameters

Based upon the nominal values of melting current, voltage, and the amount of metal deposited for a given current interval, it was possible to compute the melt rate, ingot growth rate, and energy used per kg melted. Figure 4 is a plot illustrating the influence of melting current on the melt rate. It is clear from this figure that higher currents yield nearly proportionally higher melt rates although the influence of current becomes slightly less significant at higher current levels. Figure 5 presents ingot linear growth rate U_I, as a function of melt current. Since $U_I = \dot{m}/\rho A_I$ where $\dot{m}$ is the mass growth rate and ρ is the metal mass density and A_I the cross-sectional area of the ingot, Figure 5 resembles Figure 4.

A plot of energy consumption per kg melted vs melting current in Figure 6 shows that, in general, melting efficiency is not influenced by current over the experimental range of 2kA to 6kA.

The crucible heat flux was computed from the crucible water flow rate and in/out temperature measurements. The dependence of crucible power and total power input on melting current is illustrated in Figure 7. The heat transfer to the crucible increases as the current increases, and because energy is released more slowly than it is added, the power loss to the crucible exceeds the power input at currents less than 5kA. This is due to the finite heat conductivity of the ingot and high heat capacity of the metal.

A tabular summary of the above results along with appropriate melt parameters is shown in Table I of Appendix I.

B. Ingot Analysis

A montage of the image enhanced radiographs for the longitudinal sections is illustrated in Figure 3. A similar color enhanced montage calibrated for Nb composition is illustated in Figure 8. Observed pool volume was estimated by measuring the volume of revolution generated by a solute band. Likewise the volume bounded by the T_I isotherm and the upper surface of the pool in the computer simulations was computed, and both are plotted as a function of melting current in Figure 9.

As illustrated in Figure 3, six vertical grid lines are drawn on the enhanced radiograph with line pairs of the same number representing equal distances from the ingot centerline. The amount of time required to deposit a band is determined by measuring the distance between intersections of the bands with the grid lines and then dividing this value by the ingot growth rate U_I at that location. In this way, average band period $\overline{\tau}$ is obtained for each constant current region, and this value along with the standard deviation σ and sample size N are presented in Table II of the Appendix I for the entire matrix of measurements. A significance test,

$$Z_{m,n} = \frac{\overline{X}_m - \overline{X}_n}{\left(\frac{\sigma_m^2}{N_m} + \frac{\sigma_m^2}{N_n}\right)^{1/2}}$$

is used to evaluate significant differences between average band periods for all m where $-3 \leq m \leq +3$ and n where $-3 \leq n \leq +3$. When $Z \geq 1.96$ the hypothesis that two averages are significantly different is accepted with 95% confidence. The $Z_{m,n}$ values for this matrix are presented in Table II of Appendix I. Average band periods are plotted as a function of melting current (independent of location) in Figure 10 and the bounding lines in this plot represent the maximum deviation at each current level when the average value is allowed a ± 1 σ scatter.

Wet chemistries obtained from drillings of the horizontal slices shown in Figure 2 are plotted as a function of melting current in Figure 11. The data in Figure 11 illustrate that Nb concentration at the surface and mid radius locations are very similar for the higher currents (4,5, and 6kA). At 3kA there is significant Nb enrichment at the edge location. The ingot center line concentration is very strongly influenced by melting current over the entire current range.

Metallographic specimens obtained from the longitudinal ingot slice (see Figure 2) were polished and air etched. The resulting photomacrographs along with Nb concentration vs distance plots for a single electron microprobe analyser scan on each specimen are illustrated in Figures 12 through 15. The dark areas in the photomacrographs are depleted in Nb with peak to valley concentration spreads of approximately 3 w/oNb, 4w/oNb, and 4.25w/oNb for 6kA, 5kA, and 4kA current levels, respectively. Although the solute bands appear continuous in the radiograph (see Figure 3) it is clear from Figures 12 through 15 that at higher magnification, the bands are discontinuous.

Code Simulation

A. Numerical Model

As described in detail in the various sections of Appendix III, a numerical model of the ingot top including the molten pool was constructed. A time-accurate integration of the governing equations of a cylinder cut from the top of the ingot was performed.

The boundary conditions applied to the cut ("outflow" or bottom surface of the computational grid) of the ingot are chosen to be as compliant as possible numerically, and their physical effects are discussed in Appendix III.

The other boundary conditions consist of specifying axisymmetric motions and a shear-free pool surface, along with the thermal boundary conditions displayed in Figure A.7, Page 95. Briefly, one can say that the conditions on stream function, vorticity, and top surface (x = o) temperature are all accurate (or that the solution is insensitive to them) so that these are unlikely to be modified much in future studies. The same is not true of the crucible wall-ingot surface boundary conditions on temperature. This boundary condition attempts to parameterize the thermal resistance of a variable pressure contact. The Lorentz body force, (which has not yet been modified to model the actual motion of the vacuum arcs) is also uncertain. Likewise the specification of the liquid metal thermophysical properties will require more accurate measurements. As a result of these uncertainties, the simulation of a particular case can be carried out at present only by varying each of the uncertain parameters over its plausible range. The solutions presented below, then, represent the first point in such a parameter study, not, by any means, final results.

Besides the latter uncertain parameters and the former well-controlled ones, each simulation case requires as input from experiment a value for U_I, the linear ingot growth rate; for R and

R_e, the ingot and electrode radii, respectively; and for the total melting current, I_m. In the simulation of the Y-12 melt, the total time at each current level was also specified to match the actual melt, so that the solutions given below in fact represent five discrete times during a single simulation run, not five unrelated solutions. As a result, this computational coupling closely approximates the actual experimental conditions from the standpoint of melt history effects.

The computational grid used in the calculation is displayed on each plot of the results, in order to emphasize the limited resolution. Dependent variable values, given at these grid points, represent the average value of the variable over the 0.521 cm x 0.521 cm rectangles centered on the grid points (actually, centered on the cross-sections of rings in the axisymmetric geometry). Surface and axis grid points correspond to half and quarter cells.

The thermal field is presented as a set of isotherm plots (See Figures 16, 17, 19, 24, 26, and 28). On each plot, four isotherms: T_s^*(1440K), T_o(1523K), T_I(1551K), and T_L(1606K) are specially flagged to characterize the mushy zone. As described in Appendix III, these are, respectively, T_s^*, the effective solidus temperature determined by a linear fit to the enthalpy-temperature curve resulting from the Scheil relationships (5); T_o is halfway between solidus and liquidus temperatures and serves as the datum for dimensionless temperature; T_I, is the immobilization temperature at which liquid and solid are prescribed to move together as a rigid body; and T_L, the liquidus temperature from the equilibrium phase diagram for the U-Nb system. The value of T_I is determined by arbitrarily prescribing immobilization at 0.38 mass fraction solid (0.55 volume fraction solid), and then interpolating the Scheil $f_s(T)$ relationship to determine the corresponding temperature.

To depict the motions of the melt pool, the streamfunction $\psi(x,r)$ is plotted in each case. Given an instantaneous velocity field, a set of streamlines may be obtained from it by constructing contours tangent to the velocity vectors. The streamfunction, which is constant on these contours, has the useful mathematical properties noted in Appendix III, and also the following:

(i) No particle ever crosses a streamline

(ii) The total volume of fluid passing through a surface per unit time is simply the change in the streamfunction between the surface boundaries. Equivalently, if uniformly spaced streamlines are plotted, equal volume flow rates occur between them, so that flow velocity magnitude is inversely proportional to streamline separation

(iii) In a steady (time-independent) flow, a streamline is a particle path. In the axisymmetric motions of the melt pool, one should speak of "streamsurfaces" rather than "streamlines" since a closed-loop streamline on the plots actually is the cross section of a toroid about the ingot axis. Further, those cells which extend to the axis resemble a bowl in three dimensions, as indicated in the inset to Figure 20.

Generally the streamfunction plots contain both counterclockwise rotating cells due to domination of the Lorentz forces ("magnetic cells", green) and clockwise rotating cells due to domination of the buoyancy forces ("thermal cells", red). While a sufficiently weak current could lead to a solution with only thermal cells, the converse situation--entirely counterclockwise magnetic cell circulation-is not physically plausible. This is because such a flow, by countering heat transfer, must enhance thermal gradients at its boundary. The enhanced gradients in turn produce greater buoyancy forces and must ultimately produce a thermal cell. Since viscosity cannot stabilize a horizontal temperature gradient, on any length scale, it follows that even very large currents cannot produce a pure magnetic cell; therefore, some thermal cell, however thin, must always accompany it.

Each streamfunction plot consists of two parts; first, a set of uniformly spaced streamlines with a spacing $\Delta\psi$ (which varies from 2.0 to 9.0 as noted in the figure captions), and second, a pair of blue streamlines which indicate the path followed by particles entering the pool top at radii of 2cm and 9 cm. In addition, vectors are plotted to indicate the direction and magnitude of the largest surface and interior velocities. In general, the magnitudes of these increase as $\Delta\psi$ increases, because, as stated earlier, the total volume flowrate between streamlines is $\Delta\psi$ itself.

B. Simulation Results.

Based on the experimental values of U_I, R_e, R, and I_m listed in Table I, plus the thermophysical properties listed in Appendix III, a code simulation of the Y-12 melt was run. During this simulation tables of the dependent variable values at the gridpoints were printed at various output times along with printer plots of streamfunction and isotherms. At the end of each constant-current period Versatec electrostatic plotter output was prepared. This produced not only higher-resolution plotting but also allowed a detailed analysis of the T(x,r) and ψ(x,r) surfaces. These higher quality plots are presented below, but part of the discussion comes from the auxiliary output.

Since the Y-12 ingot was melted from a quasisteady state at 6kA current, the first phase of the simulation attempted to produce such a state numerically. This attempt failed because the magnetic cells proved so dominant that the pool depth exceeded the 14.1 cm length of the computational grid. (See Figure 16). This difficulty probably arises because not all the 6kA melt current actually penetrates the pool, and Lorentz forces in the actual pool are correspondingly weaker than in the present model. Since the magnetic cells' opposition to heat transfer is the cause of the unrealistically deep computed pool, improvement of the current path model should remove this problem.

Since the improved current model is not complete, a nominal current of $I_m = 5.54$ kA, with a melt rate interpolated from the 5kA and 6kA measured rates, was used as a rough equivalent to the actual 6kA starting current level. This produced a less distorted solution but which was still noticeably deformed near the outflow boundary. As can be seen by the presence of the hot plume of liquid descending along the axis in the isotherm plot, (Figure 17) this solution consists of a dominant magnetic cell over most of the pool with only a relatively thin thermal cell on the edge of the mushy zone (see Figure 18) countering this dominance. Further, the auxiliary output indicates that this solution is quasisteady, showing only weak fluctuations of the streamfunction. To the four-digit accuracy of the output tables, the enthalpy solution is steady.

When the current is reduced to 5 kA for the appropriate time, the resulting isotherms (Figure 19) and streamlines (Figure 20) still show that the outflow boundary condition is distorting the interior solution, but less significantly.

A prime question raised above was whether or not the 477 s duration of the 5 kA current was sufficient to achieve a quasisteady condition. By plotting the evolution of the enthalpy at points most distant from any boundary (Figure 21) one can see clearly that, although some change in the temperature of the solid was still occurring at the end of this time, the liquidus and solidus had achieved steady positions. Thus the pool shape can be regarded as steady over about half the 5kA melt period.

At this current level, it is instructive to examine the overall energy budget, computed as described in Appendix III, and displayed in Figure 22. From the measured melt rate, $\dot{m}$ = 0.188 kg/s (Table I), it follows that the melting of the electrode requires 59 kW. Because very little cooling is possible during transfer of metal to the pool, this energy is supplied directly to the ingot. The code simulation indicates that material inflow carries with it another 9 kW, which must come from the arc energy, resulting in a total inflow power of 68 kW to the pool. The code also indicates 7 kW are received by conduction at the pool surface; again, this must come from the arc. Since the code conserves energy, this received energy total is lost by outflow conduction and material transfer plus conductive/radiative loss at the crucible wall. These considerations leave 60 kW of the 135 kW electrical energy input unaccounted for; presumably, this is lost directly to the crucible wall by the arc. Since no direct measurement has yet been made to support this partition of the energy, the power loss has a question mark attached to indicate uncertainty.

For the 4 kA run, it is apparent from the time sequence printer plots of streamfunction that the pool flow has not become steady. This is quite apparent in Figure 23, where the sensitive enthalpies are plotted as functions of time. The scale is compressed by a factor of two from that of Figure 21, so the fluctuations in the near-liquidus enthalpy here are about ten times as large as at 5 kA. However, the histories of the solid enthalpies indicate that the solidified ingot is at a steady state, so the fluctuations in the pool must be regarded as an actual feature of the solution. This must imply that the different pool circulation patterns which appear must be "thermally equivalent" in the sense that their heat transfer to the solid is the same. Thus, although the isotherms of the solid in Figure 24 represent the solution at all subsequent times, neither the pool isotherm pattern nor the streamfunction (Figure 25) is steady.

The same kind of behavior is displayed even more clearly in the 3kA case, which had the longest duration of all current levels. On the streamfunction printer plots, a thermal cell is typically created at the high thermal gradient point under the edge of the electrode. This thermal cell then migrates toward the axis and is assimilated by the magnetic cells. A similar pattern of birth, migration, and annihilation occurs for magnetic cells being created at radii just beyond the strong thermal gradient. Nevertheless, the isotherms in the solid (Figure 26) are quite steady, and the pool is sufficiently shallow at this current that the outflow boundary condition produces no discernable distortion. Streamlines for 3kA are shown in Figure 27.

After the current is reduced to 2 kA, the pool settles down and is essentially a thermal circulation, although weak cells which may have either sign occur around the axis. This is equivalent to saying that the cancellation between buoyancy and Lorentz forces is almost complete near the ingot axis, so that flow is almost zero. The overall dominance by the thermal cell also has the effect of making the pool extremely shallow; see Figures 28 and 29.

The effect of varying the currents (and hence melt rates) can be seen indirectly in Figures 30 and 31, which display the elements of the energy budget and the axis temperature profiles, respectively, as functions of melt current. Computed pool volume as a function of melt current has already been presented in Figure 9, along with the experimentally determined values.

Discussion

It is clear from the almost constant energy consumption per kg melted as a function of melting current (Figure 6) that energy efficiency will not dictate selection of a melting current. However, the chemical analysis results and solute band spacing results lead to the conclusion that higher currents favor better ingot homogeneity. It is speculated that the center line segregation pattern illustated in the enhanced radiograph at the higher current levels (Figure 3) is a channel segregate caused by channel flow instabilities (6). This type of segregate results when hot fluid flows into a cooler partially solidified region and creates an unstable situation wherein a channel will melt back (grow) at the expense of the surrounding solidified material. The large thermal flows in Figures 18 and 20 (5.5 and 5kA) could result in the necessary flows to supply hot material to this region and thus disrupt the solute banding.

It should be pointed out that all of the streamfunction plots are very crude first estimates to the actual flows. The current streamlines (see Figure A.8) used in the model are first approximations and will change as the model is refined. The new model will incorporate more current flow to the ingot-crucible meniscus area of the pool and will probably result in less magnetic influence. Thus, the flows will be weaker and the buoyancy and Lorentz forces will be more nearly balanced. The sensitivity of this balance is demonstrated in the difference between the 6kA and 5.5kA isotherm plots (see Figures 16 and 17). A 0.5kA increase in current changes the flow to complete magnetic dominance resulting in a very large pool. The radiographic evidence clearly shows that this does not happen, suggesting that a significant fraction of the DC electrode current does not pass through the pool, but is grounded by electrode-to-crucible wall arcs. Such arcs are seen in high speed photography results (1,4).

In addition, the current path for this model is assumed to be steady state. Under actual conditions the current flow is made up of rapidly-moving arcs, interrupted by drop shorts (4). During the lifetime of a short all of the current is directed to a localized area and, depending on the drop short frequency, these interruptions could have a significant effect on the fluid flow. Thus, with a revised current model, the solutions could differ considerably from the model used in these calculations.

For all cases calculated here surface and cell fluid velocities decrease as the current is decreased. However, these velocities must increase again at even lower currents as the Lorentz force ceases to oppose the buoyancy force. Another general observation is that a significant amount of material injected on the pool surface follows a tortuous path that passes through the pool-crucible meniscus area. This implies that boundary conditions selected for this region have a large influence on the entire ingot.

Good agreement between calculated and measured pool volume, except at 6kA (see Figure 9), is an indication that the isotherm plots are reasonable estimates of actual conditions. The estimated volumes are generally larger than the measured values and this difference could result from an inadequate current streamline model (magnetic flows are too strong) or improper selection of the liquid immobilization isotherm. Immobilization of the system to fast flows at a volume fraction solid of 0.55 is based on a considered guess. There is much controversy among solidification investigators concerning the definition as well as the value of the immobilization temperature and a more accurate estimate awaits definitive experiments.

When considering the observed macrosegregation, it is interesting to note that the ingot tops for currents of 5kA and less are almost all partially solidified. Thus, a significant amount of fast fluid flow (at temperatures between T_L and T_I) occurs in partially solidified regions. This implies a large interaction between the pool flows and low fraction solid regions. It also implies that channel segregation should be common.

The isotherm plots show that large regions of low permeability (large fraction solid) exist. It is fortunate that the solidification shrinkage for this alloy system is low (2.5%), so that only small amounts of liquid are required to feed shrinkage in this low permeability region. Thus, shrinkage driven flows are weak resulting in corresponding weak induced macrosegregation in these large mushy regions.

Mehrabian (7) has calculated the propensity for macrosegregation in a unidirectionally solidified U-6w/oNb ingot. The results are shown in Figure 32. It can be seen that as fluid flow velocities perpendicular to the isotherms ($V_\perp$) increase (at a constant growth rate, U_I) macrosegregation becomes more severe. In addition, flows from cold to hot regions result in a depletion of Nb and flows from hot to cold regions result in increased Nb contents. Thus, very weak flows ($U_I < 0.2$) from cold to hot could yield 5w/oNb in a unidirectionally solidified ingot. Although it is impossible to apply the results from the unidirectionally solidified case to the VAR process because the VAR ingot allows motion along isotherms as well as across them, the above qualitative statements still describe the local instantaneous development of macro-segregation and are thus useful guides. For example, the flow in the 5 kA and 5.5 kA cases (see Figures 20 and 18) carries all particles around the tip of the thermal cell as they cross the liquidus isotherm. Their subsequent motion as they solidify is from the wall (cold) toward the axis (hot). Their cross-isotherm velocity U_I is small, and, except for flows near the axis, positive. Thus, one expects Nb-rich alloy near the wall and progressively more Nb-poor material as the axis is approached. Were the currents increased even beyond the strength examined here, the flow through the mushy zone would predominately follow the magnetic cell, from axis toward wall. One would then expect Nb-rich centerlines and U-rich (possibly channel segregated) surfaces on the resulting ingot.

The amount of time required to deposit a solute band at each cross section line decreases slightly in the current range from 4kA to 6kA (see Figure 10). In addition, the bands appear to be axisymmetric within this current range as indicated by the low scatter associated with the data points.

At 3kA the bands are not axisymmetric as indicated by the wide scatter bands and there is a much larger spread between band periods at locations close to the ingot surface (locations ± 3) and locations close to the axis (locations ± 1). In general the time required to deposit a solute band increases as the ingot centerline is approached at a particular current level and the data in Figure 10 seems to indicate that bands start to become unstable at currents less than 4kA. That the time required to deposit a solute band increases as the ingot center line is approached also implies that the number of bands decreases as the axis is approached. This is confirmed on the radiograph (see Figure 3) where it is clear that two bands can merge into one band as the axis is approached.

Flemings (8) has studied solute banding in unidirectional solidified Al-Cu ingots and he concluded that solute bands can be caused by acceleration or deceleration of the liquidus isotherm. His model differs from the earlier theoretical model of Tiller et al. (9) in that the kinetics-induced concentration wave is absent but interdendritic shrinkage-fed flows are considered. We conjecture that the source of such accelerations is the change in diffusivity with solute concentration, in the latter stages of solidification (i.e., at small fraction liquid, in the zone where shrinkage must produce a "planar" flow perpendicular to isotherms). This picture is supported by the observed microstructure of the bands in Figures 12 through 15.

CONCLUSIONS

From the first part of this continuing investigation, it is possible to draw a number of conclusions of practical importance.

1. The U-6w/oNb experimental ingot remelted at Y-12 was under thermal control as demonstrated by parameter continuity over the range of melting currents.
2. Energy consumption per kg melted is constant over the range of melting currents from 3 kA to 6kA.
3. Negative centerline macrosegregation occurs and is sensitive to melting current and decreases as current is increased from 3 kA to 6 kA.
4. The time required to deposit a solute band is not sensitive to melting current in the range from 4 to 6 kA as determined by significant difference tests.
5. Solute bands are not continuous but are interrupted by what appears to be dendritic structure.
6. The Nb concentration range across a solute band decreases from 4.3 w/o to 3.0 w/o as the melting current is increased from 4 to 6 kA, respectively.
7. Fluid flow within the molten pool is not sensitive to location of material inflow on the top surface of the ingot.
8. Heat transfer analysis (Appendix III) and limited experimental observations for steels are in agreement for a ~ 200 K upper bound on superheat for metal transferred from the electrode.

9. At higher currents (≥ 5 kA) fluid circulation is dominated by a magnetic cell and at low currents (≤ 2 kA) fluid circulation is dominated by a thermal cell.

10. At intermediate current levels the flow is time dependent as a result of the unstable standoff between the Lorentz and buoyancy forces.

11. In general the volume of partially solidified material is greater than the volume of liquid ahead of the advancing dendrites.

12. There is qualitative agreement between observed pool volumes and computed pool volumes.

13. Radiography coupled with image enhancement shows great potential as a diagnostic tool to provide global information about segregation and fluid flow.

FUTURE WORK

A number of questions need to be answered before a sharply focused picture can be drawn of the vacuum consumable arc remelt process by the combined computational and experimental program.

1. Determine the important U-alloy thermophysical properties by a computational parameter study and arrange to obtain experimental values for these properties.

2. Experimentally determine the heat flow boundary conditions at the crucible wall.

3. Determine the arc radiation flux to the crucible wall with the retractable hearth furnace.

4. Determine fluid velocities on the pool surface by using high speed photography with the retractable hearth furnace.
5. Develop a computational model for current distributions within the ingot that is consistent with the high speed movie observations of the arc.
6. Conduct tracer experiments with U and Nb isotopes to evaluate the immobilization isotherm.
7. Computationally couple the present fluid flow model with the differential equations for macrosegregation as developed by Flemings and Mehrabian.

ACKNOWLEDGEMENTS

The broad scope of this investigation has resulted in a great deal of interaction with people of many technical disciplines.

The authors are grateful for the help received from personnel of the Nondestructive Testing, 1551, and the Photometric and Optical Development Division, 1556. Rogue Feliciano and Fay Tamashiro were particularly helpful in generating the radiographic negatives and digitizing them, respectively. Hilary Jones (8334) expended a considerable effort enhancing the digitized radiographs with a Stanford Technology Image Processor.

The efforts of Y-12 personnel are particularly appreciated. Dave Beck coordinated the melting experiments and all of the ingot cutting and chemistry sampling. John Koger and Nick Jessen

arranged for the Y-12 financial support of these activities.

Robert Merhrabian (U. S. Bureau of Standards) provided valuable technical inputs concerning fluid flow and macrosegregation. Barry Marder (2623) contributed technical input concerning the current streamlines, and Gordon McClure (2353) provided inputs concerning the physics of vacuum arcs.

Personnel of the Electron Optics and X-Ray Analysis Division 5822 provided the microanalysis and metallography.

The authors are grateful to R. W. Fisher, J. Maroone A. Netz, and N. Zamora (all 5836) for coordinating various projects concerned with this investigation.

APPENDIX I - DATA TABLES

Table I. Melt Parameters - U-6w/oNb Ingot

Variable	6kA	5kA	4kA	3kA	2kA	Units
time start	10:09:51	10:15:15	10:22:42	10:32:18	10:50:00	hrs,min,s
time stop	10:15:15	10:22:42	10:32:18	10:50:00	10:59:00	hrs,min,s
Δt	324	447	576	1062	540	s
ram start	89.4	97.02	106.7	116.8	128.3	cm
ram finish	97.02	106.7	116.8	128.3	130.8	cm
ingot start	26.7	37.7	51.5	66.1	82.5	cm
ingot stop	37.7	51.5	66.1	82.5	88.9	cm
Δ ingot	11.0	13.8	14.6	16.4	6.4	cm
Δ volume	3839	4832	5089	5710	2243.2	cm^3
Δ mass	66.57	83.79	88.25	99.01	38.89	kg
melt rate	0.206	0.188	0.153	0.0932	0.072	kg/s
voltage	28	27	24.5	23.5	22	volts
energy used	5.48×10^7	6.03×10^{-7}	5.64×10^7	7.49×10^7	2.38×10^7	joules
energy/kg	8.24×10^5	7.20×10^5	6.41×10^5	7.56×10^5	6.12×10^5	joules/kg
ΔT_{H_2O}	6.0	5.0	3.9	2.8	2.2	°C
$j_{electrode}$	1.4	26.2	20.9	15.7	10.5	A/cm^2
Ingot Growth Rate	0.0340	0.0310	0.0253	0.0154	0.0120	cm/sec
Power	1.68×10^5	1.35×10^5	9.8×10^4	7.05×10^4	4.4×10^4	watts
$\dot{Q}$ crucible	1.49×10^5	1.25×10^5	1.02×10^5	7.44×10^4	5.54×10^4	watts

Notes;

Electrode Dia.	0.156	m
Ingot Dia.	0.208	m
Electrode Wt.	538	kg
Cooling water flow rate	5.96×10^{-3}	m^3/s

Table II. Solute Band Period Measurements as a Function of Location and Melting Current

	Melting Current				
Variable	6kA	5kA	4kA	3kA	Units
Line − 3 $\bar{\tau}$	13.8	15.6	19.5	34.3	s
Line − 3 σ	3.24	3.55	3.95	8.44	s
Line − 3 N	20	18	17	17	
Line − 2 $\bar{\tau}$	14.5	18.4	19.8	51.6	s
Line − 2 σ	4.12	3.55	3.16	11.69	s
Line − 2 N	21	18	15	12	
Line − 1 $\bar{\tau}$	20.3	21.1	33.6	70.8	s
Line − 1 σ	6.47	5.16	6.32	16.88	s
Line − 1 N	17	14	11	8	
Line + 1 $\bar{\tau}$	22.5	18.5	32.1	83.1	s
Line + 1 σ	6.47	5.81	4.74	11.04	s
Line + 1 N	13	17	10	7	
Line + 2 $\bar{\tau}$	13.2	15.0	22.5	70.9	s
Line + 2 σ	2.35	2.26	6.72	24.03	s
Line + 2 N	24	24	18	8	
Line + 3 $\bar{\tau}$	13.2	13.8	17.8	49.2	s
Line + 3 σ	2.65	4.84	4.35	14.3	s
Line + 3 N	20	28	23	12	
U_I	0.034	0.031	0.0253	0.0154	cm/s

Where τ = band period, σ = standard deviation of band period, and N = the number of band period measurements

Lines ±3 near ingot surface, Line ±2 near ingot mid-radius, Lines ±1 near ingot axis.

Table III. Significant Difference Table for Band Period Measurements As a Function of Location and Melting Current

	Melting Current			
Variable	6kA	5kA	4kA	3kA
$Z_{-3,3}$	1.37	1.45	1.58	2.07
$Z_{-2,2}$	1.45	1.52	1.48	2.30
$Z_{-1,1}$	1.69	1.70	2.03	3.04
$Z_{-3,-2}$	1.37	1.45	1.58	2.11
$Z_{-2,-1}$	1.42	1.51	1.47	2.46
$Z_{3,2}$	1.30	1.42	1.55	2.25
$Z_{2,1}$	1.23	1.26	1.79	3.11

Notes: A significant difference exists at 95% confidence if $|Z| \geq 1.96$.
Z subscripts refer to sampling location in the ingot.
Location 3 is near the ingot surface, Location 2 is near the ingot mid-radius, Location 1 is near the ingot axis. (See Figure 3)

APPENDIX II

Mathematical Treatment for Evaluation of Absorption Coefficients to Obtain Nb Concentration Directly from Radiographs

Using the x-ray intensity equation

$$I = I_o e^{-\mu t},$$

where:
I = radiation intensity transmitted through specimen
I_o = source radiation intensity
μ = absorption coefficient of material being evaluated
t = thickness of specimen through which radiation has passed

it is possible, using step wedges, to evaluate the absorption coefficient for both pure uranium and the U-6w/oNb alloy. For two different steps (identified by subscripts 1 and 2, respectively) on the uranium step wedge.

$$I_1 = I_o e^{-(\mu_U t_1)} ; \qquad (II.1)$$

and

$$I_2 = I_o e^{-(\mu_U t_2)} . \qquad (II.2)$$

must hold. Dividing (II.1) by (II.2) gives

$$\frac{I_1}{I_2} = \exp\left\{-\mu_U(t_1 - t_2)\right\} ; \qquad (II.3)$$

solving for μ_U gives

$$-\mu_U = \frac{\ln(I_1/I_2)}{t_1 - t_2} .$$

Likewise for the U-6w/oNb alloy:

$$I_1 = I_o e^{-(\mu_{6Nb} t_1)} \tag{II.5}$$

and

$$I_2 = I_o e^{-(\mu_{6Nb} t_2)} \tag{II.6}$$

so that

$$-\mu_{6Nb} = \frac{\ln(I_1/I_2)}{t_1 - t_2} \tag{II.7}$$

Assuming that the absorption coefficient changes linearly with changing Nb concentration, it is possible to obtain Nb concentration as a function of intensity at constant specimen thickness. Thus, define:

$$-M_{Nb} = \frac{\mu_U - \mu_{6Nb}}{6} \tag{II.8}$$

where M_{Nb} is the absorption coefficient per 1% Nb. Then, at an arbitrary weight percent of Nb, denoted by C, the transmitted intensity I_c is given by

$$I_c = I_o \exp\left\{-(M_{Nb} C + \mu_U) t_c\right\} \tag{II.9}$$

if the specimen thickness was t_c. For the same thickness of pure U

$$I_U = I_o e^{-(\mu_U t_c)} \tag{II.10}$$

so that dividing by (II.9) and solving for C gives

$$C = \frac{-\ln(I_c/I_U)}{M_{Nb} t_c} \tag{II.11}$$

If t_c is not the same as the thickness of a step of the step wedge, the concentration can still be calculated. Consider a point (x,y) on the specimen, with measured thickness t_{xy} and measured intensity I_{xy}; then:

$$I_{xy} = I_o \exp\left\{- (M_{Nb} C_{xy} + \mu_U) t_{xy}\right\} \tag{II.12}$$

must hold. As before, pure uranium of thickness t_U will have

$$I_U = I_o e^{-(\mu_U t_U)} \tag{II.13}$$

so that dividing (II.11) by (II.12) allows one to solve for C_{xy}:

$$C_{xy} = \frac{-\ln(I_{xy}/I_U) + \mu_U(t_U - t_{xy})}{M_{Nb} t_{xy}} \tag{II.14}$$

Appendix III

Thermal Environment. The typical situation during VAR melting is shown in Figure A.1. Clearly, simulation of the entire furnace would be a very large task, and would result in a model of so many uncertain parameters that conclusions drawn from the simulation would always be suspect. Accordingly, attention here is focused on the most active region, consisting of the hot end of the electrode, the electrode gap, and the top portion of the ingot. Despite the large number of interactions among these components (Figure A.2), an even more restricted view can be taken because of the simplicity of the thermal budget of the electrode.

Start by considering the electrode as a one-dimensional cylinder (Figure A.3); i.e., suppose the temperature depends only on distance, x, from the hot end. After a long time has elapsed from startup, a quasisteady temperature T(x) will be set up in the electrode; this satisfies:

$$U_e \frac{\partial T}{\partial x} = \kappa \frac{\partial^2 T}{\partial x^2}$$

where U_e is the electrode feed rate (cm/s), κ is the thermal diffusivity of the solid (cm^2/s). The input temperature T_r is assumed to be room temperature (300K) if the electrode is long enough, and the maximum temperature on the hot end, T_m, can be estimated by the following simple argument. First, T_m must exceed the liquidus temperature of the electrode, T_L (1605.5K for U-6w/oNb), since the metal transfer in VAR is observed to be due to droplet transmission from electrode to pool (1,2,4). When the VAR process is shut down in mid-melt, the film of liquid solidifies on the electrode face with a refined grain structure, so the depth of the liquid layer can be measured by observing the depth, δ_L, of the recrystallized zone. This is typically a couple of millimeters; thus, the superheat, T_m-T_L, cannot exceed that needed to conduct the energy flux required to maintain quasisteady melting of the electrode, P_e, namely:

$$P_e = \dot{m}(L + C_p\ (T_m - T_r)) = k_L\ (T_m - T_L)\pi R_e^2/\delta_L$$

where L = latent heat (j/g), C_p is specific heat (j/g-K), k_L is liquid conductivity (W/cm-K), R_e is electrode radius (cm) and $\dot{m}$ is the mass melt rate (g/s). From this, the superheat is given by:

$$T_m - T_L = (h_L/C_p)\ (k_L \pi R_e^2/\dot{m}\delta_L C_p - 1)^{-1} = 1635\text{K}/(\frac{1406\text{g/s}}{\dot{m}} - 1)$$

which gives $88\text{K} < T_m-T_L < 280\text{K}$ for the parameters of the Y-12 melt. In short, the superheat is rather narrowly bounded within a range of a couple of hundred degrees, from the single observation of recrystallized layer thickness. This conclusion is supported, and, in fact, the range narrowed to the lower end, by observations of steel melts in the retractable hearth VAR furnace at Sandia, in which high speed photography(4) was used to observe both a cherry red color of electrode surface, and to observe dendritic-form "islands" in the liquid film; both suggest just barely molten conditions. Further support comes from the argument that the liquid film is Rayleigh-Taylor unstable, with its heavy liquid suspended above the vacuum by surface tension alone. Thus, droplets will detach as soon as liquid is available, again suggesting low superheats because the liquid cannot remain on the electrode long enough to gain much temperature. In the model, then, electrode surface superheat, $T_m - T_L$, is assumed with considerable confidence to lie in the 100K-200K range. The calculations reported above used a superheat of 122K for all current levels.

Finally, with the superheat specified, the whole quasi-steady temperature solution T(x) is given by:

$$T(x) = T_r + (T_m - T_r) e^{-U_e x/\kappa}$$

which has a length scale (e-folding distance), δ, of $\kappa/U_e \simeq$ 3 to 8 cm for the Y-12 melt rates. Ignoring the radial temperature dependence, this solution can be used to compute an upper bound to the radiative losses through a length L_e of the electrode surface, denoted by $\dot{Q}_{eL}$ in Figure A.2:

$$\dot{Q}_{eL} = 2\pi\varepsilon\sigma^* \int_0^{L_e} T^4 R_e dx$$

where ε is the hemispheric total emittance of U-6Nb, estimated (10) at 0.3 for a clean surface and at 0.75 for an oxidized one; σ^* is the constant in the Stefan-Boltzmann radiation law, $5.67 \times 10^{-12} W/cm^2\text{-}K^4$. When T is given by the above quasisteady solution, the result is:

$$\dot{Q}_{eL} = \frac{\kappa T_m^4}{U_e} \left(\frac{U_e L_e}{\kappa} - \frac{25}{12}\right) r^4 + r^3 + \frac{1}{2} r^2 + \frac{1}{3} r + \frac{1}{4} \quad \simeq 0.7 \text{ to } 2 \text{ kW}$$

for the Y-12 parameters with $r = T_r/T_m = 0.176$. Compared to the typical scale of P_e, which is 20-70kW for superheats below 200K, this radiated power is negligible. Thus, the electrode acts like a one-dimensional cylinder, and the above arguments justify use of T(x) as an excellent approximation to its quasisteady temperature.

With the electrode temperature known, the top of the ingot, including the melt pool, can be considered separately. In this closer view (Figure A.2), there are many interactions between the elements; however, step-by-step analysis allows estimation of these.

Start by considering the remaining radiative fluxes, $\dot{Q}_R$ and $\dot{Q}_{RL}$. When the electrode gap is very short, as is assumed here, the net radiative exchange, $\dot{Q}_R$, can only become significant when the pool and electrode are at quite different temperatures. This can be verified by computing the solid angle Ω subtended by a circular disc of radius R_e. When viewed from a point r off its axis and h out of its plane, this is:

$$\Omega = \begin{cases} \displaystyle\int_0^{\pi} \left(1 - \frac{h/Re}{q^{1/2}(\theta)}\right) \frac{q(\theta)+k_1-h^2/R_e^2}{q^{1/2}(\theta)-h^2/R_e^2}\, d\theta & \text{for } r \le R_e \\ \displaystyle\int_0^{\theta^*} \frac{h}{R_e}\left[\frac{1}{q^{1/2}} - \frac{1}{\left\{q+2\frac{r}{R_e}\sin\phi\sin(\phi+\theta)\right\}^{1/2}}\right] \frac{p(\theta)\,d\theta}{p(\theta)-k_1}, & r \ge R_e \end{cases}$$

where $p(\theta) = 2(1-r\cos\theta/R_e)$, $k_1 = 1 - r^2/R_e$ and $q(\theta) = 2(1-r\cos\theta/R_e)-1+(r^2+h^2)/R_e$. The angles are given by $\theta^* = \cos^{-1}(R_e/r)$ and $\cos^2\phi = (\cos\theta-r/R_e)^2/(p(\theta)-k_1)$. The indicated quadrature was carried out numerically, and the results given as "viewfactor", i.e., the fraction of the hemispherical solid angle subtended by the disc, $v^* = \Omega/2\pi$, producing the curves shown in Figure A.4. From the figure, it is apparent that short electrode gap, h, results in very tight radiative coupling between the electrode surface and the pool surface directly below it, while the annulus between R_e and the wall of the crucible is only very weakly coupled. Since the ratio h/R_e varied between 0.24 and 0.36 in the Y-12 experiment, it can be concluded that the pool surface sees essentially only electrode in its "sky" for $r < R_e$, and sees mostly cool crucible wall for $r > R_e$; as a result, the temperature will be a function of the same form as the viewfactor, nearly discontinuous under the edge of the electrode, at $r = R_e$. Supposing, then, that

$$T_s(r) = \begin{cases} T_p & r < R_e \\ T_a & r > R_e \end{cases}$$

gives the surface temperature distribution, one must have

$$\dot{Q}_{RL} = \pi R_e^2 \varepsilon\sigma^*(T_p^4 - T_m^4) = \pi R_e^2 \varepsilon\sigma^* T_m^4(T_p^4/T_m^4 - 1) = 2.77\text{kW}(T_p^4/T_m^4 - 1)$$

which indicates that $T_p/T_m = 2^{1/4}$ before even 2kW net radiative flux can pass between pool and electrode, i.e., the pool temperature would need to be more than 350K higher than the electrode. Similarly the annulus flux is bounded above by

$$\dot{Q}_{RL} \leq \pi R_e^2 \varepsilon\sigma^* T_p^4 (R^2/R_e^2 - 1)\ (T_a^4/T_p^4)$$

which indicates fractional kW radiation, since $R/R_e = 4/3$, and $T_a/T_p \approx 0.8$ because the temperature of the annulus cannot exceed the melt temperature of the crucible wall (T_{Cu} = 1360K) by much, and T_p cannot differ from T_m (1606K) by much. Thus, it is concluded that the surface temperature of the melt pool is the discontinuous function $T_s(r)$, with $T_p = T_m$ and $T_a = T_L$, and that the radiative fluxes are all negligible in the global energy budget. Having determined a pool surface temperature distribution, one can begin to consider separating the ingot from the rest of the furnace for analysis. To do this requires parameterization of the ingot-crucible wall heat exchange, and, if very large computational meshes are to be avoided, requires an estimate of conditions on some internal surface of the ingot as well. Both can be done because of the fact that the solidifying ingot must shrink on cooling, so that it breaks contact with the crucible wall at some not-very-large distance below the pool surface, as was indicated in Figure A.1. This means that the ingot transfers heat to the wall by radiation over most of its lateral surface, and, because radiation is so weak below about 1000K, most of a long ingot behaves like an insulated cylinder, i.e., a one-dimensional cylinder. In the case of the ingot, this cylinder is being built up by addition of hot material to its end; at quasisteady growth conditions, this steady addition must eventually dominate over the ability of the ingot to diffuse the heat (addition occurs proportional to time, t; diffusion is proportional to $t^{1/2}$) and the ingot must have a uniform axial temperature distribution, $T(x) = \text{const} = T_1$, say. This can be confirmed formally by seeking a solution to the quasisteady problem:

$$U_I \frac{\partial T}{\partial x} = \kappa \frac{\partial^2 T}{\partial x^2}$$

The only solution to this is given by:

$$T(x) = \frac{\kappa}{U_I} \left(\frac{\partial T}{\partial x}\right)_{x=0} e^{U_I x/\kappa} + T_1$$

and this requires $(\partial T/\partial x)_{x=o}=0$ if $T(x)$ is to be bounded; i.e., only $T = \text{const}$ can be a bounded solution to the quasisteady growing-cylinder problem. One thus expects an axial temperature distribution of the general form sketched in Figure A.5 when melting conditions are held constant enough to produce quasisteady melting.

Since most the the length of the ingot will be at nearly constant temperature, the portion of interest--the top section containing the pool--can indeed be isolated for analysis, and either an insulated boundary condition given on the cut section ($\partial T/\partial x = 0$ at $x = L_1$, say) or an even less demanding "outflow" boundary condition could be chosen ($\partial^2 T/\partial x^2 = 0$ at $x = L_1$). The latter was chosen here in order to allow use of the smallest possible computational mesh by constraining the temperature field as little as feasible on the outflow boundary.

These arguments leave only one boundary condition to be specified, namely, the thermal conditions in the small zone near the top of the ingot in which there is at least partial contact between ingot and crucible wall. This interaction zone can only be parameterizd crudely for the time being; firm, detailed models of the interaction will have to await the gathering of further experimental data. The initial model incorporates only the gross features of the contact, which consist of

(i) at initial solidification, i.e., at temperatures above some value T_{RO}, the ingot makes full contact with the crucible wall, and thermal resistance between the ingot surface and the cooling water (denoted by R_o) must equal the thermal resistance of the half inch (1.27 cm) of copper plus the resistance of the boiling-transfer boundary layer in the water.

(ii) at temperatures sufficiently below solidification, thermal contraction of the ingot will have broken contact with the crucible wall entirely, so that the conductive thermal resistance between ingot and wall is infinite.

(iii) Finally, between these two extremes, partial contact will result in some intermediate thermal resistance level.

All this is present in the following model (see Figure A.6):

$$R_T = \begin{cases} R_O & T > T_{RO} \\ R_O \dfrac{T_{RO} - T_R}{T - T_R} & T_R < T < T_R \\ \infty & T < T_R \end{cases}$$

and heat flux between ingot and wall is then

$$q = (T - T_w)/R_T$$

where T_{RO} = 1405K, T_R = 1205K, and the cooling water is at T_w = 300K; R_o = 1.0W/cm^2-K. T_{RO} was chosen as the temperature at which the last liquid solidified in a nonequilibrium solidification process (=T_U), and T_R was chosen 200K lower because of the extremely low, anisotropic coefficient of thermal expansion of U (11).

A comment on the actual working of this latter boundary condition is in order. Although the form of the boundary condition provides for conduction up to full contact intensity, the fluxes actually seen in computation never approach this level. In effect, the above expressions apply a boundary temperature close to T_R at all points where the boundary condition is operating, because any flux which the ingot can conduct may be carried quite readily by the wall at high resistance, so the wall temperature need only depart slightly from T_R. Thus, most of the numerical solutions display a nearly constant wall temperature at gridpoints below the surface, where the above condition holds.

The thermal boundary conditions actually applied to the ingot top are summarized in Figure A.7.

Energy Budget Considerations.

Recalling Figure A.2, in which the various significant energy fluxes were displayed, consider now the results of having solved the thermal problem for the ingot top. Such a solution will yield a value for the ingot wall loss power $\dot{Q}_W$, for the outflow advection $\dot{Q}_{fo}$, and outflow conduction $\dot{Q}_c$, as well as inflow powers P_{ingot} and $\dot{Q}_{fs}$. Since the radiative fluxes have already been shown negligible, and $P_{electrode}$ explicitly calculated, there remains only one unknown quantity, P_{loss}. Until direct measurements are made of P_{loss}, this means that the simulation cannot yet be constrained by global energy conservation. Like the wall boundary condition problem of determining R_T, this problem will remain until appropriate measurements are made on the crucible inside wall as well as on the water jacket side. These measurements are planned for the near future.

For the time being, then, the energy budgets displayed must be regarded as provisional since the data required for a consistency check is lacking. For easy reference, the scheme of calculation of these provisional energy budgets is displayed in Table IV.

Electromagnetic Conditions.

The analysis of the current and Lorentz forces which were used in the calculations reported herein is that described in Ref. (2). That is, use is made of a quasisteady current distribution corresponding to current input on the ingot surface given by $j(x=o,r) = I_m J_1(\beta_1 r)$, where I_m is the total melting current (A), j is current density (A/cm^2), J_1 is the Bessel function of order one (see, e.g., Ref. (12)) and r is the distance from the axis of the ingot. The value β_1 is chosen to make $J_o(\beta_1 R) = 0$; i.e., potential is maximum on the axis, and falls to zero at the wall. With grounded (zero potential) lateral surfaces and bottom on a cylinder with one radius length, the resulting current streamlines are those given as Figure 3 in Bertram (2), reproduced here as Figure A.8.

Since the above current distribution was derived, Zanner (4) has obtained new data on the actual distribution of input current density by high-speed photography of the arc region, using stainless steel and superalloy melts in the unique Sandia retractable-hearth VAR facility. This data reveals that very fast-moving, very concentrated plasma columns carry the current in a typical vacuum arc, so that one may expect that the actual current distribution can be obtained only by a careful consideration of the time-dependent Maxwell equations. Results from this study are only now becoming available, and will be described elsewhere (Marder and Bertram, to appear).

Thermophysical Properties

Reliable measurements of the thermophysical properties of liquid uranium or liquid niobium are exceedingly difficult to carry out, and this has resulted in quite large variations in the published properties. For the U-Nb binary system, the situation is correspondingly worse. Therefore, considerable effort has been invested in constructing a constitutive model of the alloy in such a way that it at least possesses consistency.

The first necessity in solidification studies, is, of course, a well-defined equilibrium phase diagram. Since there is considerable difference between the phase diagrams given in Hansen (13), and Elliott, First Supplement (14), and since the melting temperature of pure Nb in both differs from that given by e.g., Wilson (15) or Barin, Knacke, and Kubashchewski (16), it was concluded that even a theoretically constructed phase diagram would be more reliable so long as it was consistent with recent data (R. Jackson, private communication). Accordingly the following argument was used.

All available data agrees that the U-Nb system posseses unlimited solid solubility in the gamma phase which forms on initial solidification. The miscibility gap of the solid solution below 1000°C is ignored here. This suggests that the system forms a near-regular mixture and thus raises the hope that the phase diagram can be derived relatively easily from free energy considerations. In particular, the procedures described in Ref. (17) with slight modifications, are applied.

Consider, then, two components A and B which have melting points T^A, T^B; latent heats L^A, L^B; and specific heats C^A_{ps}, C^B_{ps} in the solid phase and C^A_{pL}, C^N_{pL} in the liquid phase. At a temperature T, let a liquid mixture with mole fraction w* of B (atomic %/100), and a solid mixture with mole fraction w of B be in equilibrium. For convenience, define a Gibbs free energy $G_L(w^*)$ for the liquid using pure liquid A at T^A as the reference value, and a free energy for the solid $G_s(w)$ using pure solid B at T^B as the reference value. Then, if the entropy change on fusion, ΔS_f, is independent of temperature for both components, the free energies can be written:

$$G^A_L = C^A_{p_L} (T - T^A - T \ln T/T^A)$$

Liquid

$$G_L^B = C_{p_s}^B(T - T_B^B - T \ln T/T^B) + L^B(T) - T\, S_f^B$$

$$= C_{p_L}^B(T - T^B - T \ln T/T^B) + (1 - T/T^B)L^B$$

$$G_L = (1 - w^*)G_L^A + w^*G_L^B - T\Delta S_m \text{ for a regular mixture}$$

Solid

$$G_s^A = C_{p_s}^A(T - T^A - T \ln T/T^A) - (1 - T/T^A)L^A$$

$$G_s^B = C_{p_s}^B(T - T^B - T \ln T/T^B)$$

$$G_s = (1 - w)G_s^A + wG_s^B - T\Delta S_m \text{ for a regular mixture}$$

with $\Delta S_m = -R[w \ln w + (1-w)\ln(1-w)]$ being the entropy of mixing and R being the universal gas constant, 1.98647 cal/gm-mole-K. Equilibrium between phases (isothermal) then requires $\partial G_L/\partial w^* = \partial G_s/\partial w$ (equal chemical potentials in the two phases). Graphically, this is the familiar "Tangent Rule" of phase equilibrium (see, e.g., Darken and Gurry, p. 286 and pp. 333-335), depicted in Figure A.9.

Analytically, this rule takes the form:

$$\left.\frac{\partial G_s}{\partial w}\right)_{x=x} = \left.\frac{\partial G_L}{\partial w^*}\right)_{w=w}$$

which may be manipulated into:

$$\ln \frac{w}{1 - w} = \frac{G_s^A - G_L^A + G_L^B - G_s^B}{RT} + \ln \frac{w^*}{1 - w^*}$$

so that introducing

$$F_A = \exp\left(\frac{G_L^A - G_s^A}{RT}\right); \qquad F_B = \exp\left(\frac{G_s^B - G_L^B}{RT}\right)$$

yields the simple relation

$$\frac{w}{1 - w} = \frac{1}{F_A F_B} \frac{w^*}{1 - w^*}$$

The Tangent Rule also requires

$$\frac{\partial G_L}{\partial w^*} \cdot (w - w^*) = G_S(w) - G_L(w^*)$$

which, after much manipulation, reduces to

$$\frac{1 - w}{1 - w^*} = F_A$$

Combined with the earlier expression, this implies

$$\frac{w^*}{w} = F_B$$

as well. Solving finally for the unknown concentrations w and w* gives:

$$w = \frac{1 - F_A}{1 - F_A F_B} \text{ and } w^* = \frac{1 - F_A}{1 - F_A F_B} F_B$$

After some adjustment of the values found in the literature for U and Nb, (Stephens, (18); Gathers, et.al. (19), Barin, et.al. (16)) the values in Table V were chosen in order to give the broken line phase diagram shown in Figure A.10.

It should be mentioned explicitly that, while the uranium latent heat is quite close to that measured by Stephens (18) the value assumed here for niobium is 33% lower than the usual published figure (Barin et. al. (16); Wilson, (15) 1965, p. 540); however, use of the nominal L^{Nb} leads to a solidus almost coincident with the liquidus of Figure A.10 and a liquidus generally about 150K above that shown here. It is concluded that the lower figure for L^{Nb} should be used because the higher value produces a predicted phase diagram inconsistent with all current published phase diagrams.

The criterion of acceptability for the phase diagram was that it at least not contradict what little data was available to the authors on the liquidus and solidus temperatures of the U-Nb alloys. This data is indicated, in Figure A.11 below, where the detail of the U-rich end of the phase diagram is shown.

Once the phase diagram is established, an enthalpy function can be written down for the alloy if zero heat of mixing is again assumed. This leads to the expression:

$$h^e(T) = (1 - C_L)\left[h_s^U(T) + f_L L^U(T)\right] + C_L\left[h_s^{Nb}(T) + f_L L^{Nb}(T)\right] + (C_s - C_L)(1 - f_L)(h_s^{Nb} - h_s^U)$$

where the "e" superscript indicates "equilibrium", C_L is the weight fraction Nb in the liquid phase, f_L is the mass fraction liquid, from the equilibrium phase diagram, and the "s" subscript denotes the same quantities for the solid. This expression produces the solid-line graph of h vs. T in Figure A.12.

Because the above expression applies at best to equilibrium states of the alloy, it cannot be expected to accurately give the actual h(T) function in the solidifying ingot, in which nonequilibrium cooling occurs. Nevertheless, it is essential to the feasibility of macrosegregation analyses that some single-valued h(T) be specified. That is, if the heat transfer analysis is to be decoupled from the microscale details of the solidification, h(T) must be specified directly. The alternative, specification of $h(T, C_L(T), \overline{C}_s)$ where $\overline{C}_s$ is the average composition of the solid and therefore is a function of the history of the solidification process at that point, would require simultaneous solution for flow, thermal, and composition fields. This would be a considerably more demanding computational task than solving the decoupled thermal and composition (macrosegregation) problems, and the decoupled thermal problem is already approaching the capacity of the CDC7600 at Sandia. Furthermore, such detailed equations with coupled thermal and solute diffusion would almost certainly be singular since even simpler models display the Mullins-Sekerka instability (20,21).

On the other hand, it is clear that the solution obtained from the decoupled problems cannot be fully consistent precisely because it "misplaces" the latent heat release by ignoring the history contained in $\overline{C}_s$. A rough idea of the magnitude of this misplaced heat can be obtained by considering the one case of nonequilibrium solidification for which convenient analytical solutions are available: the microstructure (coring) described by Scheil equation (5). By assuming that the solidifying liquid is in equilibrium; i.e., that $C_L(T)$ is the value from the equilibrium phase diagram, while the solute in the solid does not diffuse, Scheil obtained:

$$\bar{f}_L = (C_L/C_O)^{\frac{1}{k_e-1}}$$

as the weight fraction liquid at the temperature T corresponding to C_L. Here $C_o = k_e C_L$ on the equilibrium phase diagram (const k_e), and C_o is the overall composition. The average composition of the solid is then:

$$\bar{C}_s = \int_0^1 C_s dg_s = k_e \int_0^1 C_L dg_L$$

The solidification path, $\bar{C}_s$ vs T, is plotted on Figure A.11 to indicate the degree of departure from equilibrium.

Once the fraction liquid and solid composition are determined, the enthalpy can be computed as before, with f_L and C^S replaced by $\bar{f}_L$ and $\bar{C}_s$. The result (Figure A.12) clearly shows a significant difference from the equilibrium h(T).

As noted in the main body of this report, the actual conditions (degree of segregation) can be quite different in the VAR ingot because interdendritic flow can bring liquid of nearly any composition between 0 and C_o into contact with the already formed solid. The corresponding local enthalpy can depart even further from the equilibrium value than does the "Scheil enthalpy". Thus, even though full consistency is not achieved, use of something approaching the Schiel enthalpy should be a better approximation than the existing practice of using the equilibrium enthalpy. The Scheil equations, extended to include shrinkage effects by Flemings and Nereo (22), were also applied, but 2.5% solidification shrinkage produced no significant fluid flow effect. Accordingly, a straight line is fit by eye to the Scheil curve, as shown in Figure A.12, and the following equation results:

$$h(T) = \begin{cases} C_p(T-T^U) & \\ C_p(T-T^U) + \dfrac{L}{T_L - T_s^*}(T-T_s^*) & T_s<T<T_L \\ C_p(T-T^U) + L & T \geq T_L = 1605.5\text{K} \end{cases}$$

where $C_p = 0.1742$ j/g-K and $L = 57.4$ j/g.

The remaining thermophysical properties are modeled essentially as described by Bertram (2). In particular, dimensionless temperature is given by:

$$\theta = (T - T_o^*)/\Delta T_o^*;\ T_o^* = 1/2\ (T_s^* + T_L)\ \text{and}$$
$$\Delta T_o^* = 1/2\ (T_L - T_s^*);$$

and thermal conductivity by:

$$k = \frac{k_s}{2}\left[r_k + 1 - \frac{2}{\pi}(r_k - 1)\tan^{-1}C_k\theta\right]$$

where $k_s = 0.3$ w/cm-K, $r_k = 0.85$,

and $C_k = \tan(0.99\,\frac{\pi}{2})$. Thermal diffusivity is again obtained from k(T) and h(T) as

$$\kappa = k/(\rho_o|\nabla h|/|\nabla T|)$$

a practice of growing popularity (23). The kinematic viscosity function ν(T) has been modified from that adopted for steel because the fundamental algorithm has been changed for the U-6Nb calculations (<u>See Equations of Motion below</u>):

$$\nu = \begin{cases} \nu_o & 1 \leqslant \theta \\ \nu_o \quad e^{(1-\theta)\ell n r_v} & 0 \leqslant \theta \leqslant 1 \\ r_v \nu_o & \theta < 0 \end{cases}$$

where $\nu_o = \mu/\rho = 5.2$ cp/17.34 g/cm^3 = 3×10^{-3}cm^2/s and $r_v = 500$ were adopted, based only on the observation that the molten metal appears "watery" at low superheats.

<u>Equations of Motion</u>. The same arguments that were used for stainless steel alloys (2) apply here to U-Nb alloys, and allow the same reduction of the Navier-Stokes equations and Maxwell equations to the system of three coupled partial differential equations for vorticity, ζ; streamfunction, ψ; and enthalpy h. Made dimensionless using R^2/κ_o as time unit, R as length unit, $\Delta T_o{}^*$ as temperature unit, and L/2 as energy unit, these equations are:

$$\frac{\partial\zeta}{\partial\tau} + \frac{\partial(u\zeta)}{\partial x} + \frac{\partial(v\zeta)}{\partial r} = \Pr\left\{\frac{\partial^2(\nu\zeta)}{\partial x^2} + \frac{\partial}{\partial r}\left(\frac{\partial(r\nu\zeta)}{r\partial r}\right) + S\right\} + \Pr^2 Gr\,\frac{\partial\theta}{\partial r} - \frac{1}{rA_o^2}\frac{\partial B^2}{\partial x}$$

$$\text{with } S = 2\left(\frac{\partial v}{\partial r} - \frac{\partial u}{\partial x}\right)\frac{\partial^2\nu}{\partial r\partial x} + 2\left(\frac{\partial u}{\partial r}\frac{\partial^2\nu}{\partial x^2} = \frac{\partial v}{\partial x}\frac{\partial^2\nu}{\partial r^2}\right).$$

$$\frac{\partial h}{\partial t} + \frac{\partial(uh)}{\partial x} + \frac{\partial(rvh)}{r\partial r} = \frac{\partial}{\partial x}\left(\kappa\,\frac{\partial h}{\partial x}\right) + \frac{1}{r}\frac{\partial}{\partial r}\left(\kappa r\,\frac{\partial h}{\partial r}\right) + \frac{j^2}{\sigma}$$

$$\frac{\partial^2\psi}{\partial x^2} + r\frac{\partial}{\partial r}\left(\frac{\partial\psi}{r\partial r}\right) = -r\zeta$$

Here, the dimensionless magnetic flux was scaled by $B_o = \mu I_m/2\pi R$; Prandtl number is $P_r = \nu_o/\kappa_o$; the square of the Alfven number is $A_o^2 = (\kappa_o/R)^2\mu_o\rho_o/B_o^2$; and (u,v) are the axial (x) and radial (r) velocity components respectively, related to stream function by: $u = \frac{\partial\psi}{r\partial r}$, $v = -\frac{\partial\psi}{r\partial x}$ and to vorticity by $\zeta = \frac{\partial v}{\partial x} - \frac{\partial u}{\partial r}$. Besides reducing the number of dependent variables, introducing the steam function also provides exact conservation of mass since

$$\nabla\cdot\underset{\sim}{u} = \frac{\partial u}{\partial x} + \frac{\partial(rv)}{r\partial r} = \frac{\partial^2\psi}{r\partial x\partial r} + \frac{1}{r}\frac{\partial}{\partial r}\left[-\frac{\partial\psi}{\partial x}\right] \equiv 0$$

The original solution strategy, a time accurate explicit integration of these equations, is carried out, with the solution subject to the thermal boundary conditions summarized in Figure A.7. In addition, the vorticity boundary conditions

$\zeta(x,o,t) = 0$ (axisymmetry) $\zeta(o,r,t) = 0$ (shear-free surface)

are prescribed. For the streamfunction

$\psi(x,o,t) = 0$ $\psi(o,r,t) = \psi_1 r^2$ (uniform inflow)

are given, and then solid surfaces are required to have $\zeta = \partial v_{tan}/\partial n$ and $\psi = \psi_1 r^2$. A solid surface is a gridpoint at which $T = T_I$, the "immobiliztion temperature" discussed earlier.

Two of these conditions are departures from previous practice and therefore require some comment. First, the specification of uniform inflow at the pool surface is made only for convenience in following "tracer particles" such as the blue streamlines in Figures 18, 20, 25, 27, and 29; this is an available option because the typical velocities in the pool are 10^2-10^3 times larger than U_I, the linear growth rate. Thus, the pool dynamics are independent of the details of the inflow velocity distribution so long as it is of order U_I in scale, and the surface streamfunction can be chosen at will.

The second new condition is the requirement that the flow become rigid-body motion at the immobilization temperature. Despite the additional programming complexity compared to the "viscous solid" model used earlier, this condition is preferable because of the order-of-magnitude improvement in computer run times it offers.

Just as the mushy zone was treated in a "thermally averaged" sense by adoption of the Scheil enthalpy function, this practice of applying an increasing viscosity to the liquid provides an "average" motion of solid and liquid there. Only after full solidification has occurred can one specify that the motion is truly rigid-body, but the interdendritic flow must become a negligible contributor to the heat transfer at some higher temperature, at which the fraction liquid is so small and the permeability of the dendrites so low that low velocity and small mass combine to reduce heat transfer to insignificance. This is the temperature which is estimated by T_I here.

Viewed from the other side, the liquid motions are more and more effectively retarded by the forming solid until the point is reached such that the drag is great enough that relative motion between solid and liquid is not sufficient to carry significant heat. Thus, during the initial solidification the liquid is treated as more and more viscous until immobilization occurs.

At present, the immobilization temperature is chosen on the basis of mass fraction solid, using $\overline{f}_s = 0.38$. From the above arguments, it is clear that this still represents fairly open dendrites, even though the corresponding T_I, 1551 K, is quite deep into the mushy zone compared to the usual immobilization temperature = liquidus temperature.

Numerical Solution Procedures. With the problem formulated as described above, solution for the thermal and fluid dynamic environments in the ingot proceeds numerically in a quite straightforward, even primitive, manner. Specifically, the enthalpy equation is solved on the entire computational grid as a parabolic equation; the resulting temperature field is scanned and rigid body motion prescribed in the immobilized portion of the ingot. Finally, the vorticity equation is solved in the remaining portion, and the elliptic problem for the streamfunction is inverted in the same portion, in the standard explicit approach (see, e.g., Roache, 24).

Recognizing that high spatial resolution cannot be achieved (because the explicit time step limit for stability is inversely propotional to $M^2 + N^2$ if there are M mesh points in the axial direction and N mesh points in the radial; further, the number of mesh points is proportional to NM, so that the computational effort to reach a fixed time is proportional to $MN(M^2 + N^2)$, that is, quartic in the resolution), the finite difference form of the equations of motion is chosen to be as crude-mesh tolerant as possible. Specifically, conservative forms of the equations of motion are chosen, and "kinematically consistent" velocities (Parmentier and Torrance, 25) are obtained from a simplified version of the original rules. Finally, in order to correctly treat the high-speed "core flow" of the magnetic or buoyancy dominated circulation cells in the melt pool, which have essentially hyperbolic-type equations of motion, upwind differencing is used on the advection terms of enthalpy and vorticity equations.

A natural thing to attempt for improved computational run times would be an implicit time integration in order to avoid the stability time step restriction. This was examined for these problems, using the Lees three-time-level scheme described in Lees (26) with the Harwell Sparse Matrix Package MA28, a very efficient set of nested dissection routines. The loss of accuracy of the scheme proved to be too severe; convergence to the final solution values took up to 200 iterations due to the slow damping of the characteristic "wiggles" of the typical implicit method (27).

A second approach to efficiency would be use of a semi-direct method (or any other non-timelike iteration to the steady state). Indeed, experimentation has shown this approach to be extremely fast when it succeeds, but it has a tendency to converge to the wrong nonlinear solution for these problems. The final exclusion of these methods comes for physical reasons, however: the explicit integrations indicate that the buoyancy and Lorentz force can so completely cancel each other that the resulting weak flow is intermittent even under quasisteady boundary conditions. Thus, in the end, the explicit integration proves to be the most desirable.

Other integration schemes having been eliminated, the explicit calculations must be optimized. One way of minimizing lost production time is to obtain new solutions by using some previous solution on the same grid as the initial condition; i.e., by simple continuation. An extension of this notion is also used for startup on a new grid, by specifying zero body force until somewhere between 0.1 and 0.3 dimensionless times (unit of time is R^2/κ_O, about 1550 sec for the 10.42 cm radius U-6.3w/oNb ingot), so that the pool shape is a reasonable approximation due to heat conduction alone. Also, to avoid completely irrelevant solutions which melt through the bottom of the computational mesh, the metal on the outflow boundary is always immobilized. This latter practice is quite apparent in the solutions for currents over 4kA in the above report--all such solutions have isotherms in the solid of nonphysical shape (that is, with relative maxima in T(r) occurring off-axis) due to the immobilization of the outflow and the requirements that $\partial^2 h/\partial x^2 = 0$ on outflow.

REFERENCES

1. F. J. Zanner, Sandia Laboratories Technical Report, SAND77-1410, November 1977.

2. L. A. Bertram: Proc. 1st Int. Conf. Math. Model., X.J.R. Avula, ed., Vol. III, 1977, p. 1173.

3. F. J. Zanner: Met. Trans. B, 1979, Vol. 10B, p. 133.

4. F. J. Zanner: Proc. Sixth Int. Vacuum Metallurgy Conf. on Special Melting, San Diego, CA., April, 1979, p. 417.

5. E. Scheil: Z. Metalk, 1942, Vol. 34, p. 70.

6. R. Mehrabian, M. Keane, and M. C. Flemings: Met. Trans, 1970, Vol. 1, p. 1209.

7. R. Mehrabian, private communication.

8. M. C. Flemings, R. Mehrabian, and G. E. Nereo: Trans. TMS-AIME, 1968, Vol. 242, p. 41.

9. W. A. Tiller, K. A. Jackson, J. W. Rutter, and B. Chalmers: Acta Met., 1953, Vol. 1, p. 428.

10. J. F. Lagedost, K. E. Wilkes, J. W. Droege, E. A. Eldridge, and D. E. Niesz: Battelle Report No. 1783, 1973, Battelle Columbus Laboratories, Columbus, OH.

11. J. J. Burke, D. A. Colling, A. E. Gorum, and J. Greenspan, eds: Physical Metallurgy of Uranium Alloys, 1974, Metals and Ceramics Information Center, Columbus, OH.

12. M. Abramowitz and I. Stegun: Handbook of Mathematical Functions, 1964, Dover, NY.

13. M. Anderson; Constitution of Binary Alloys, 1958, McGraw-Hill, NY.

14. R. P. Elliott: Constitution of Binary Alloys, First Supplement, 1965, McGraw-Hill, NY

15. J. R. Wilson: Met. Revs., 1965, Vol. 10, No. 40.

16. O. Barin, O. Knacke, and O. Kubashchewski: Thermomechanical Properties of Inorganic Substances, 1977, Springer-Verlag, NY.

17. L. S. Darken and R. W. Gurry: Physical Chemistry of Metals, 1953, McGraw-Hill, NY.

18. H. P. Stephens: High Temp. Sci., 1974, Vol. 6, p. 156.

19. G. R. Gathers, J. W. Shaner, D. A. Young: Phys. Rev. Lett. 1974, Vol. 33, No. 2, p. 70.

20. W. W. Mullins and R. F. Sekerka: J. Appl. Phys. 1964, Vol. 35, No. 2, p. 444.

21. J. S. Langer and L. A. Turski: Acta Met., 1977, Vol. 25, p. 1113.

22. M. C. Flemings and G. E. Nereo: Trans. TMS-AIME, 1967, Vol. 239, p. 1449.

23. E. C. Lemmon in Num Meth. in Therm. Probs., R. W. Lewis and K. Moregan, eds; 1979, Swansea, Wales.

24. P. J. Roache: Computational Fluid Dynamics, 1972, Hermosa, Albuquerque.

25. E. M. Parmentier and K. E. Torrance. J. Comp. Phys., 1975, Vol. 19, No. 4, p. 404.

26. L. Lees, Maths. Comp., 1966, Vol. 20, p. 516.

27. L. A. Bertram, Sandia Laboratories Technical Report, SAND78-0306, June, 1978.

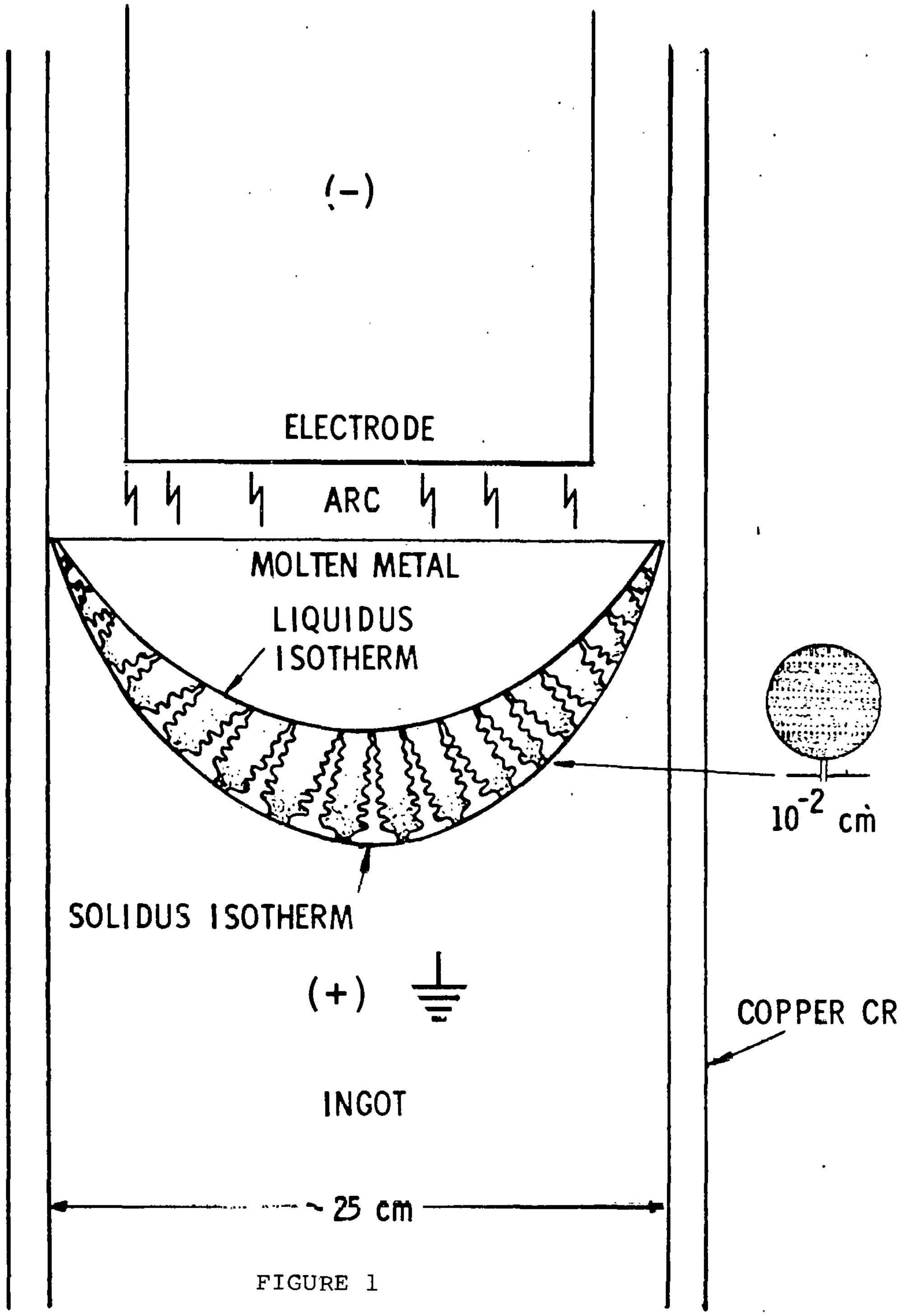

FIGURE 1

SCHEMATIC ILLUSTRATION OF THE VACUUM CONSUMABLE ARC REMELT PROCESS. SOLIDIFICATION SHOWN WITH COLUMAR GRAINS. INSERT AT RIGHT IS A SMALL SECTION OF THE LIQUID-SOLID ZONE AS IT WOULD APPEAR AT ABOUT 100X.

ANALYSIS SCHEMATIC OF VACUUM CONSUMABLE ARC REMELTED

U-6 $^{W}/o$ Nb INGOT

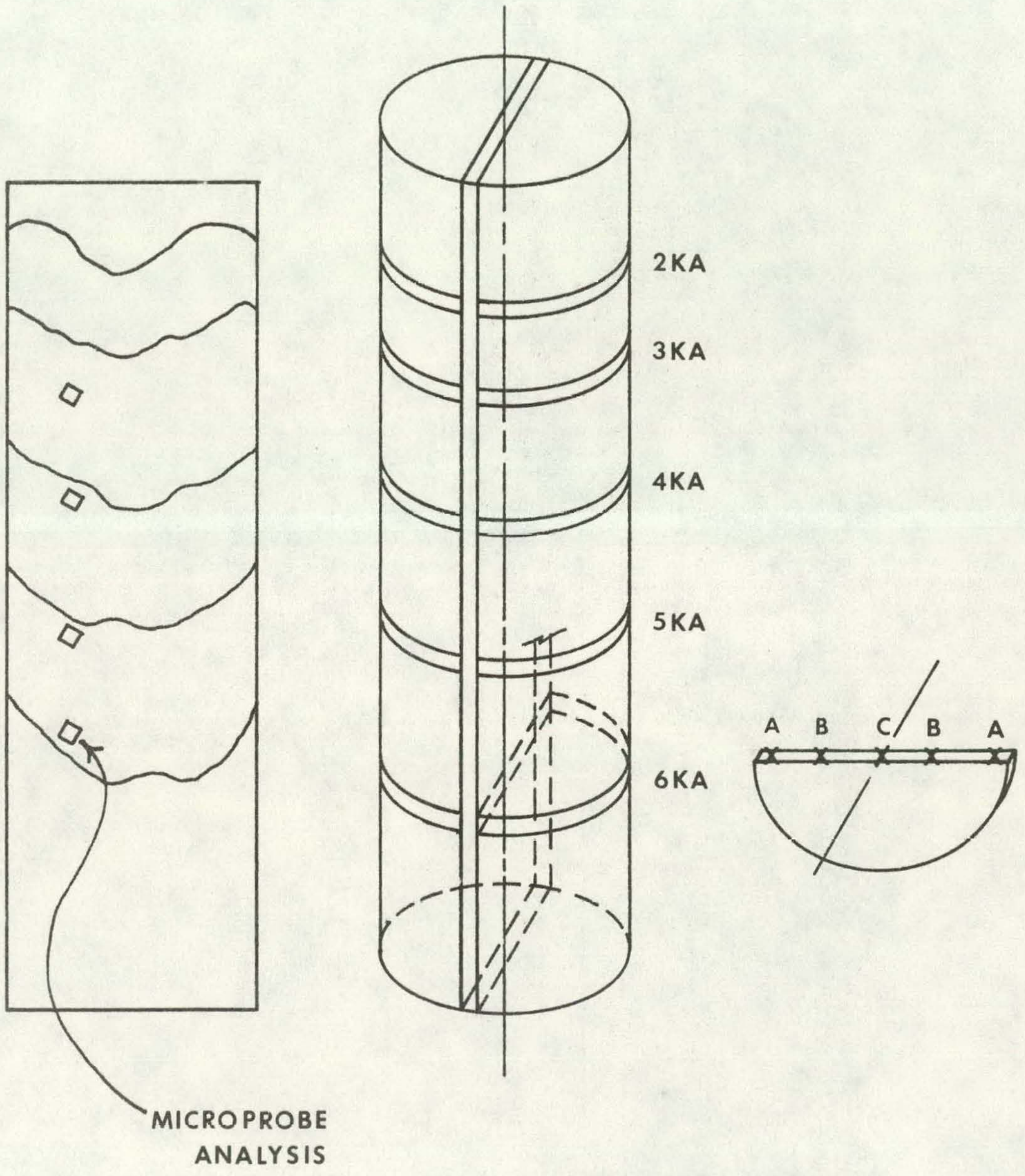

INGOT DIA. - 208 mm
ELECTRODE DIA. - 152 mm

FIGURE 2

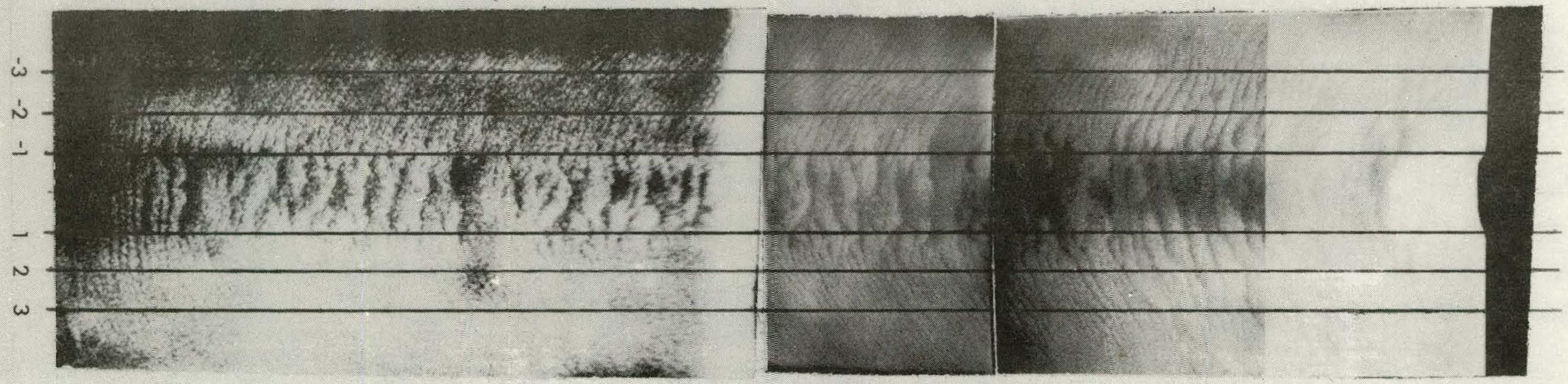

FIGURE 3: Image Enhanced Radiograph of Longitudinal Ingot Slice

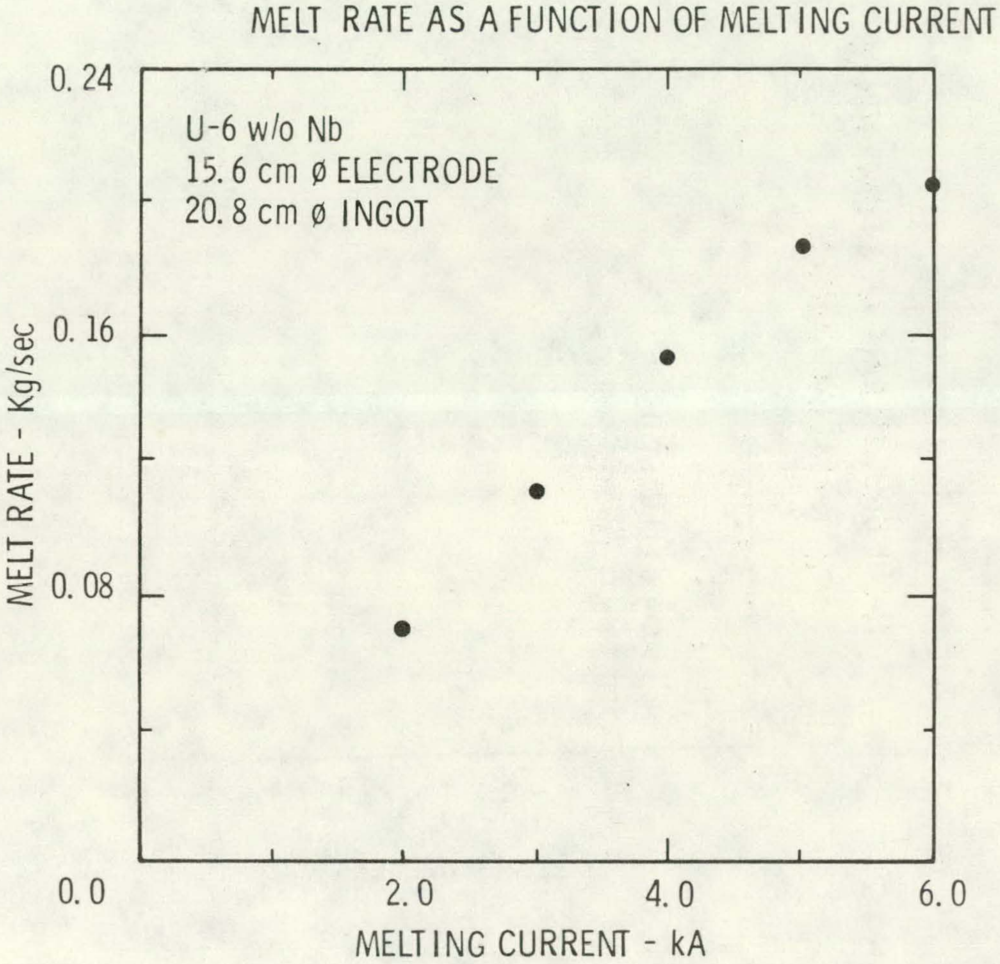
MELT RATE AS A FUNCTION OF MELTING CURRENT
0.24
0.16
0.08
0.0
U-6 w/o Nb
15.6 cm ø ELECTRODE
20.8 cm ø INGOT
MELT RATE - Kg/sec
2.0
4.0
6.0
MELTING CURRENT - kA

FIGURE 4

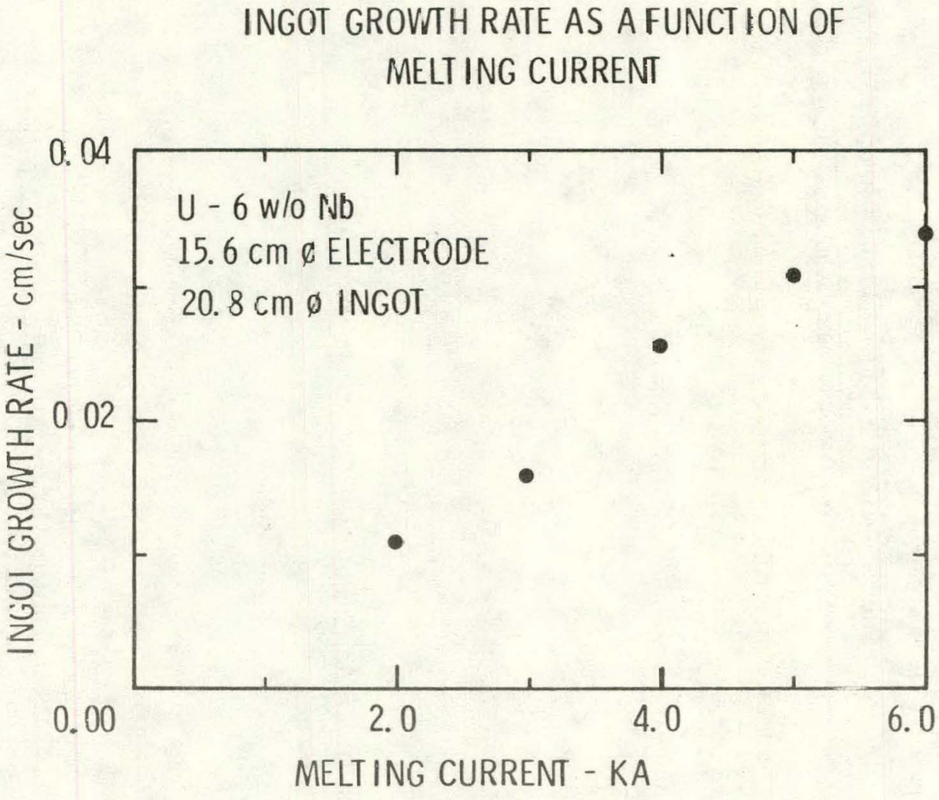
INGOT GROWTH RATE AS A FUNCTION OF MELTING CURRENT
U - 6 w/o Nb
15.6 cm ø ELECTRODE
20.8 cm ø INGOT
INGOT GROWTH RATE - cm/sec
0.04
0.02
0.00
2.0
4.0
6.0
MELTING CURRENT - KA

FIGURE 5

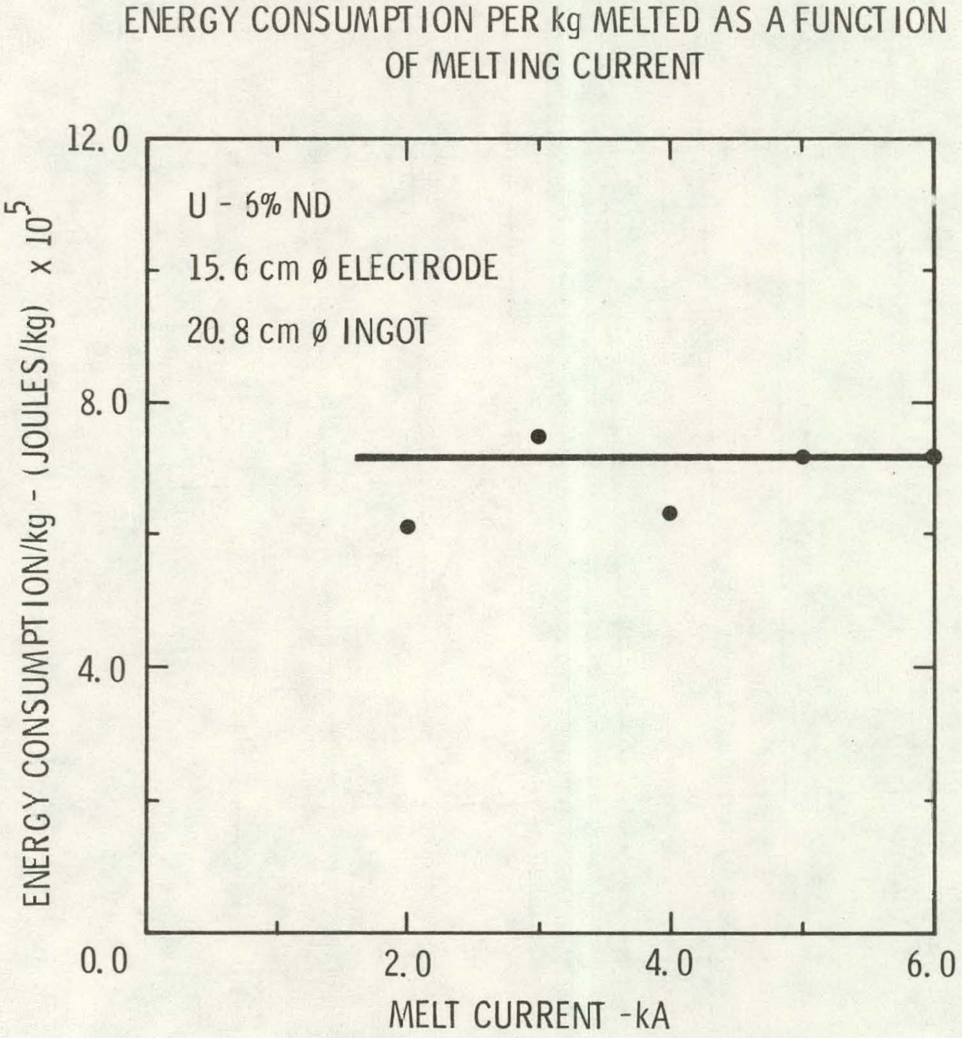
ENERGY CONSUMPTION PER kg MELTED AS A FUNCTION OF MELTING CURRENT
U - 6% ND
15.6 cm ø ELECTRODE
20.8 cm ø INGOT
ENERGY CONSUMPTION/kg - (JOULES/kg) x 10^5
12.0
8.0
4.0
0.0
2.0
4.0
6.0
MELT CURRENT -kA

FIGURE 6

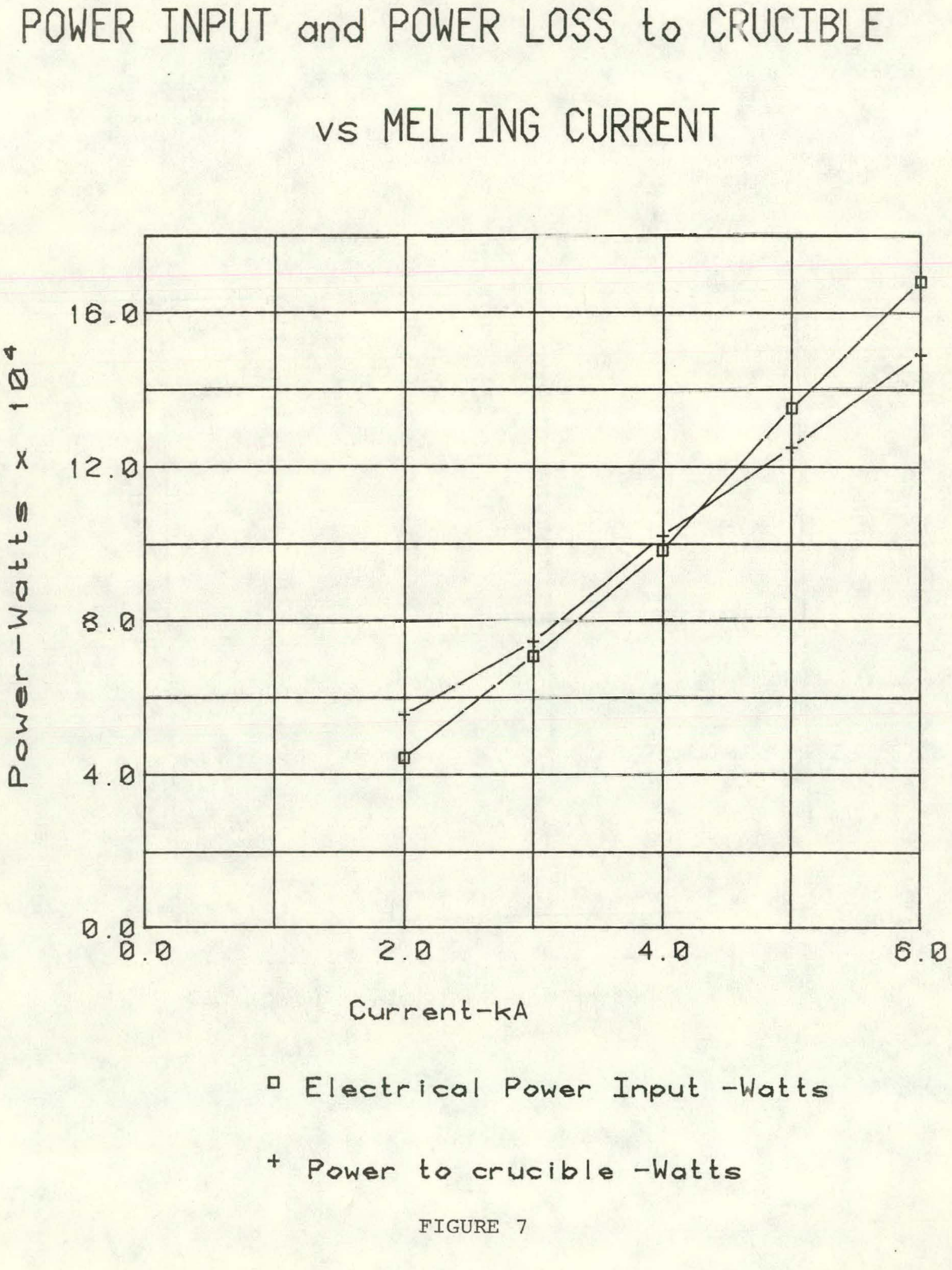
POWER INPUT and POWER LOSS to CRUCIBLE vs MELTING CURRENT

FIGURE 7

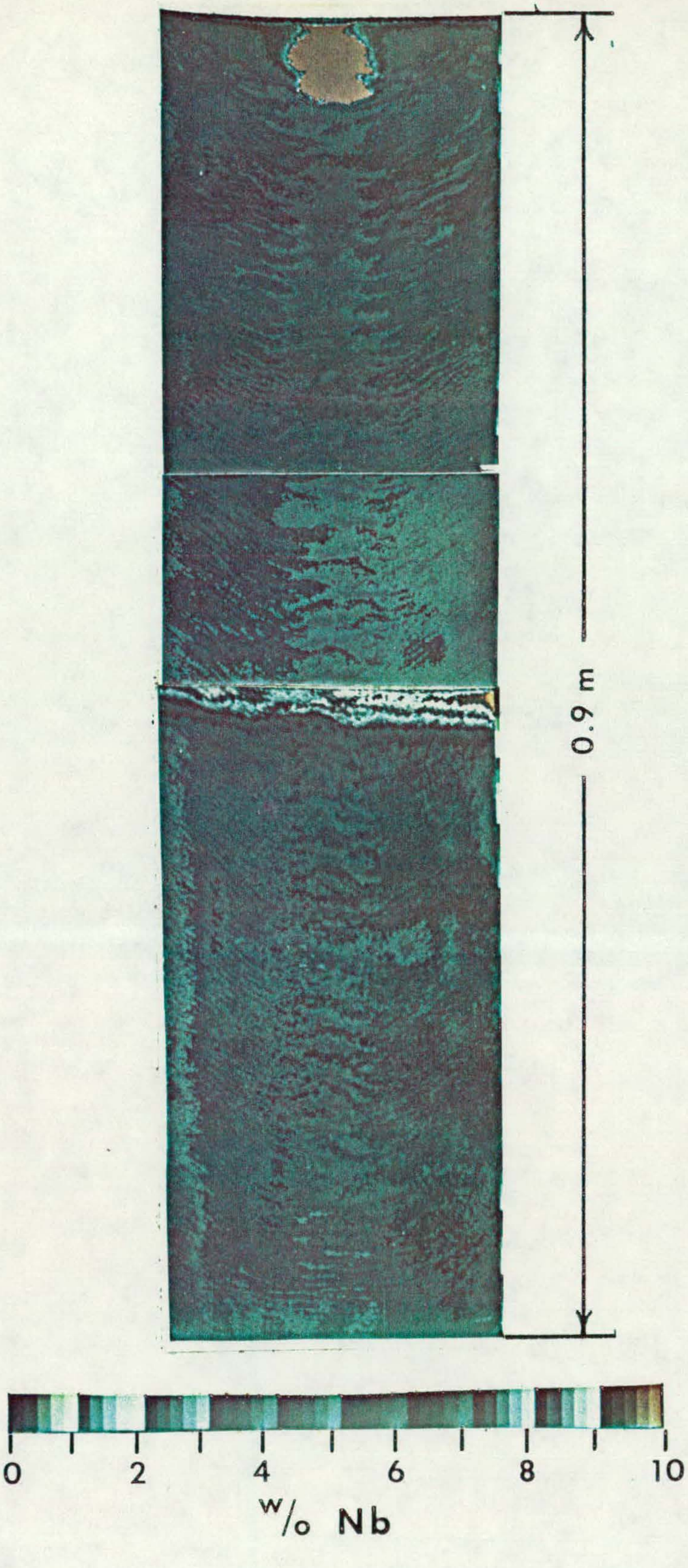

FIG. 8 - Color Enhanced Radiograph Corrected for Nb Concentration

Notes - Pink area on the top is due to shrink pipe and the pink area in the mid-section is due to a sudden change in specimen thickness

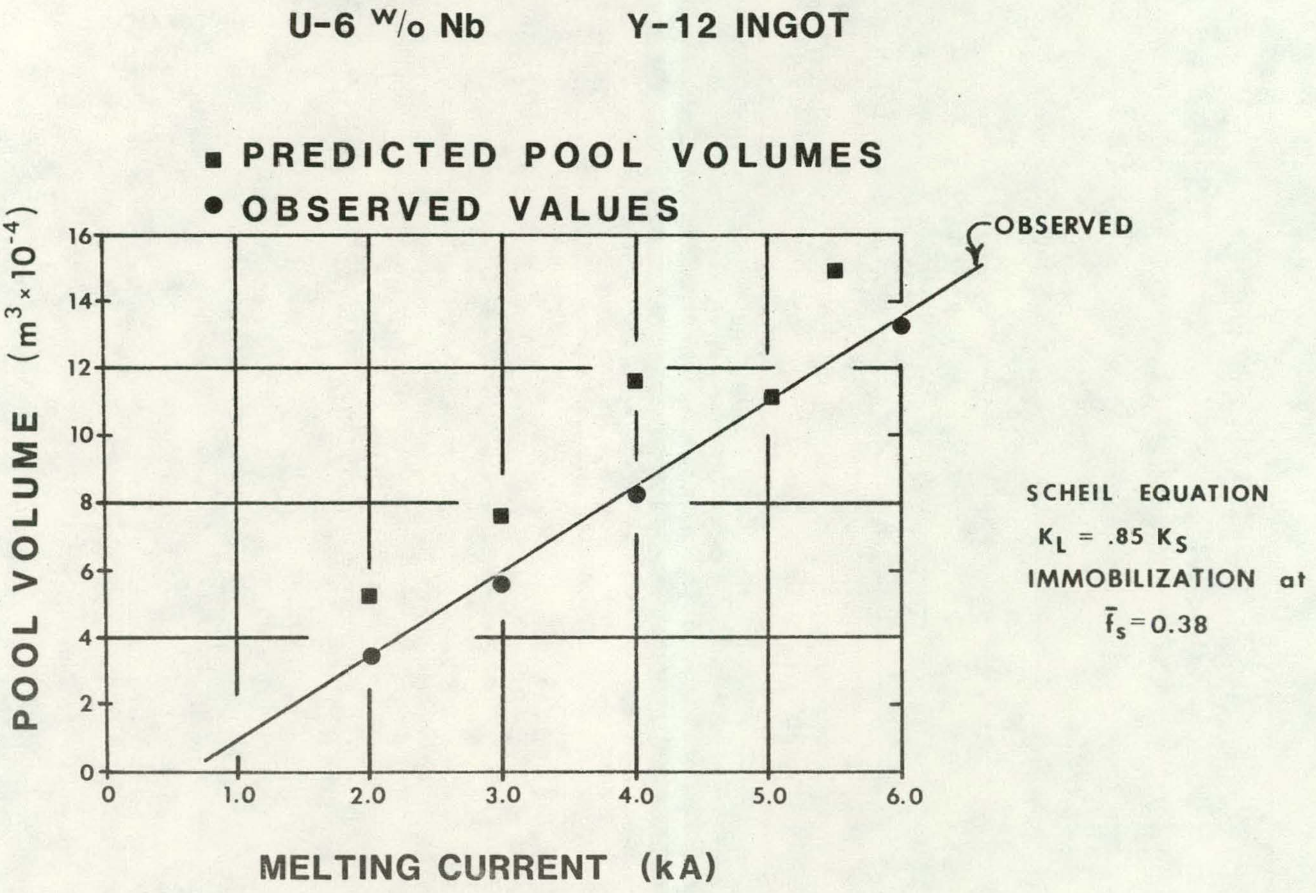

FIGURE 9: Predicted and Observed Pool Volume as a Function of Melting Current

AVERAGE SOLUTE BAND PERIOD AS A FUNCTION OF MELTING CURRENT FOR VACUUM CONSUMABLE ARC REMELTED U-6w/oNb

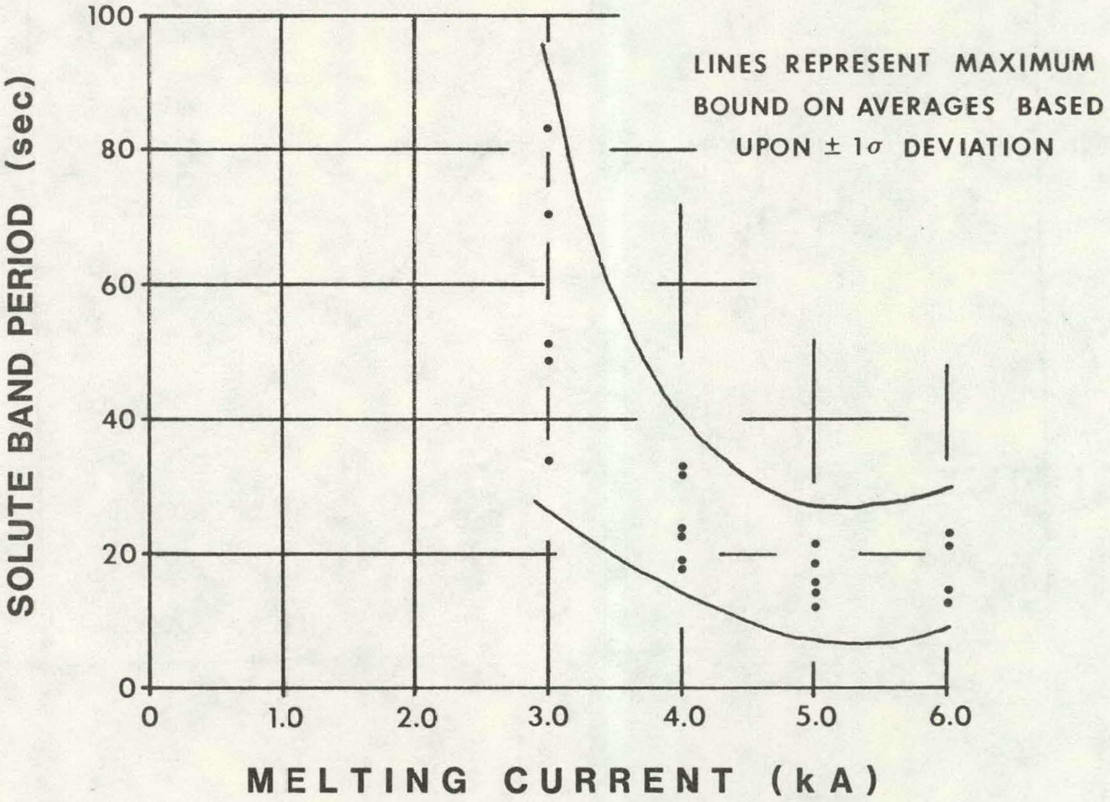

FIGURE 10

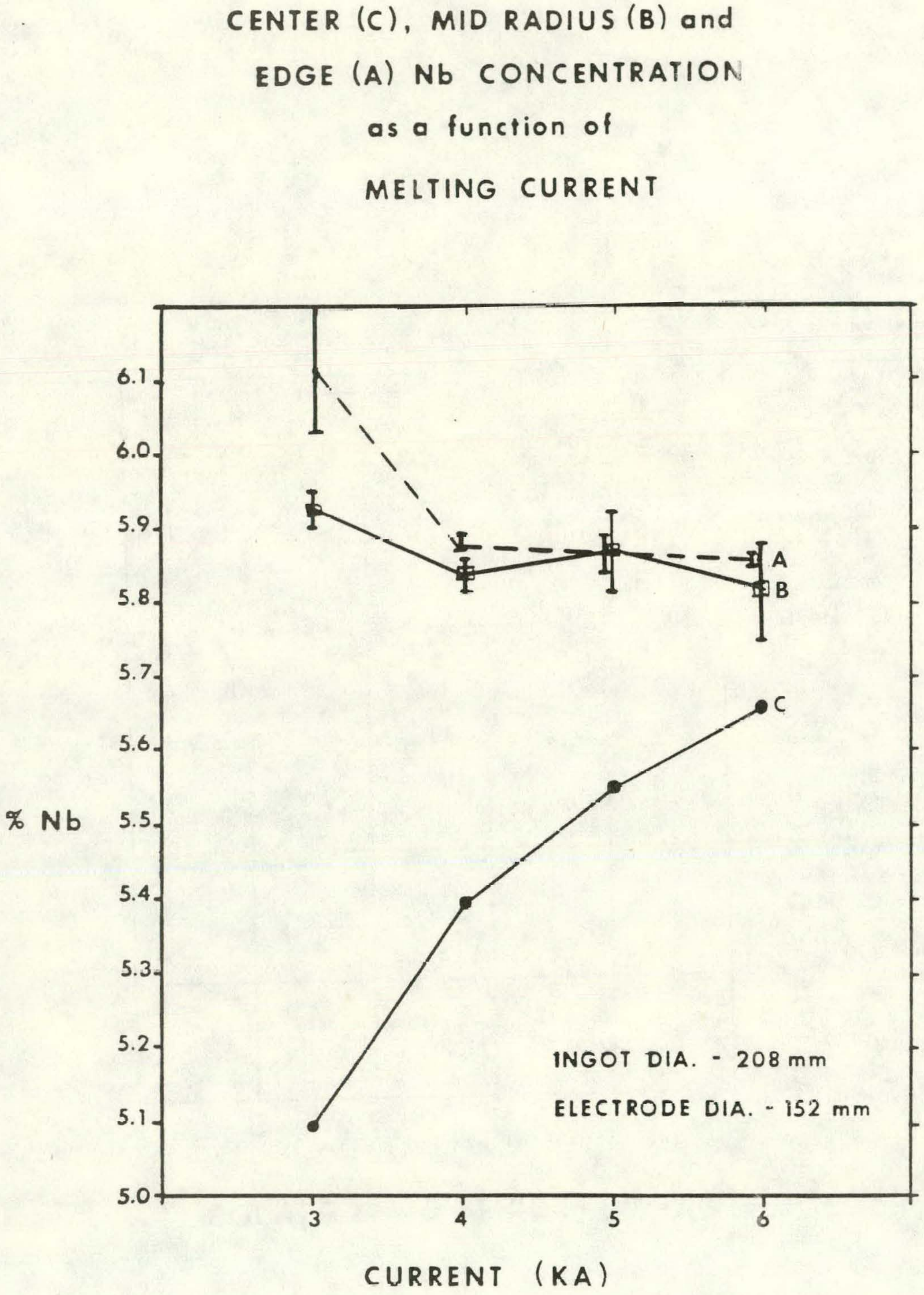

Figure 11: Nb Concentration as a Function of Melting Current for Surface, Mid-radius, and Center Locations in the Ingot.

(A)

(B)

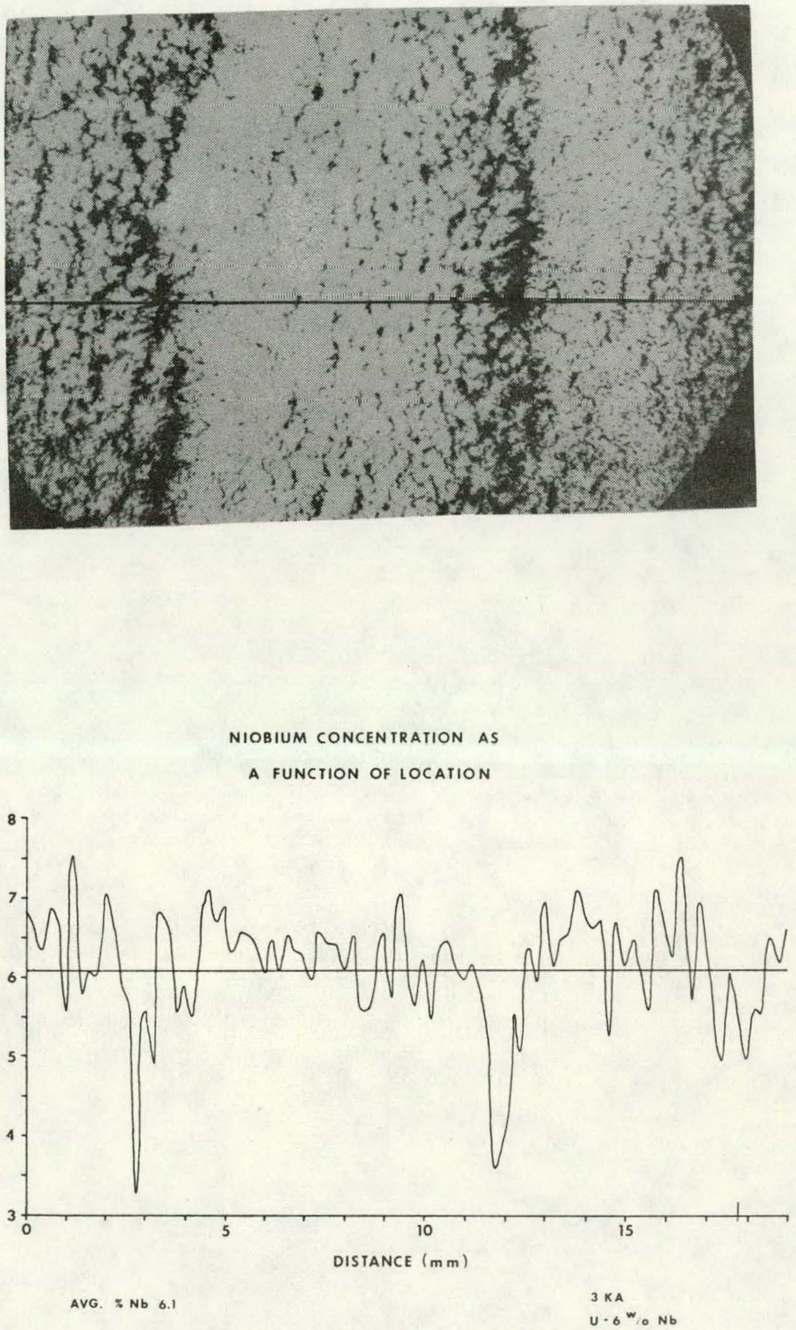

Figure 12: (A) Photomacrograph of Solute Band Segregation at 3 kA.

(B) Nb Concentration vs. Distance for a Scan Along Line Shown in (A)

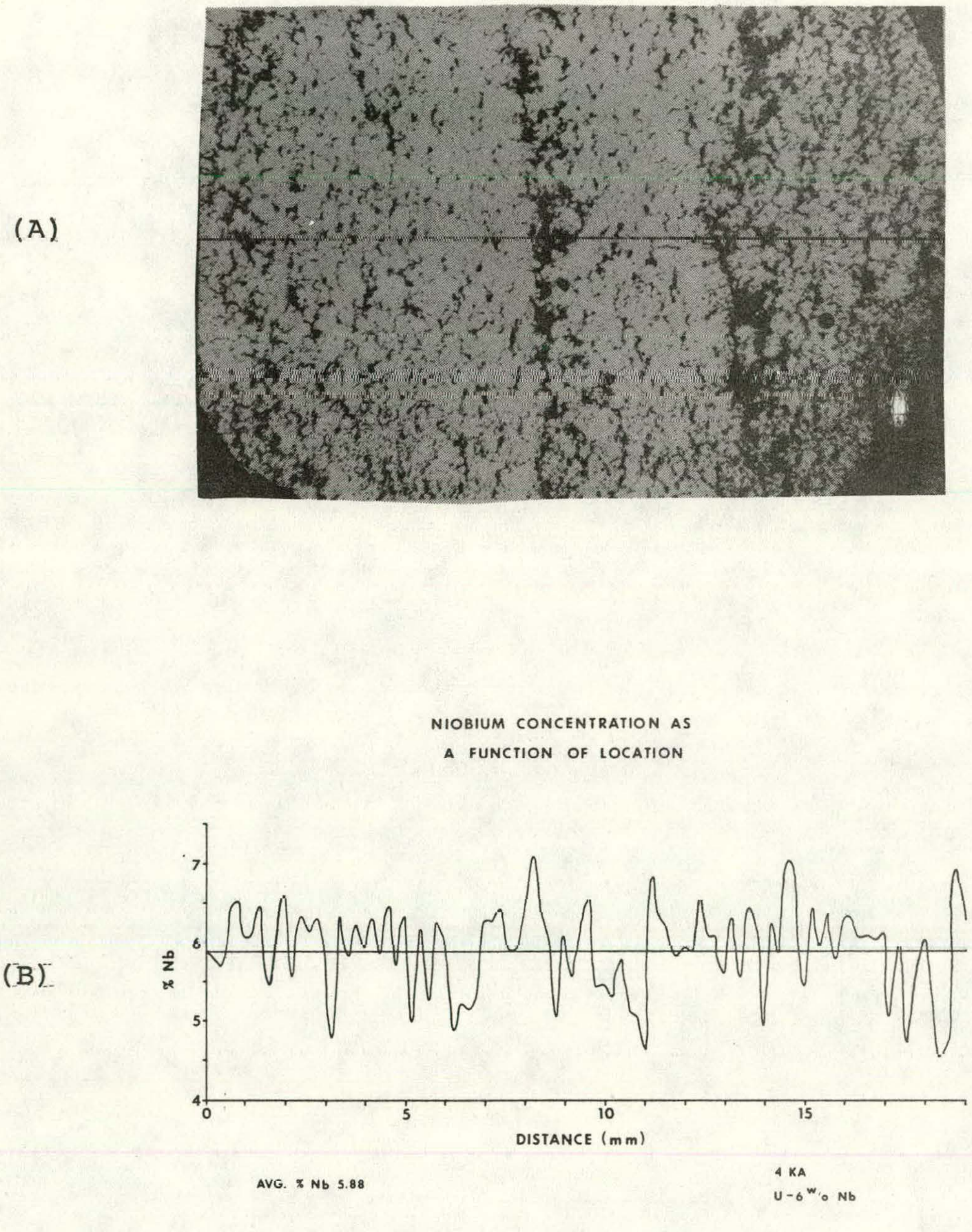

Figure 13: (A) Photomacrograph of Solute Band Segregation at 4 kA

(B) Nb Concentration vs. Distance for a Scan Along Line Shown in (A)

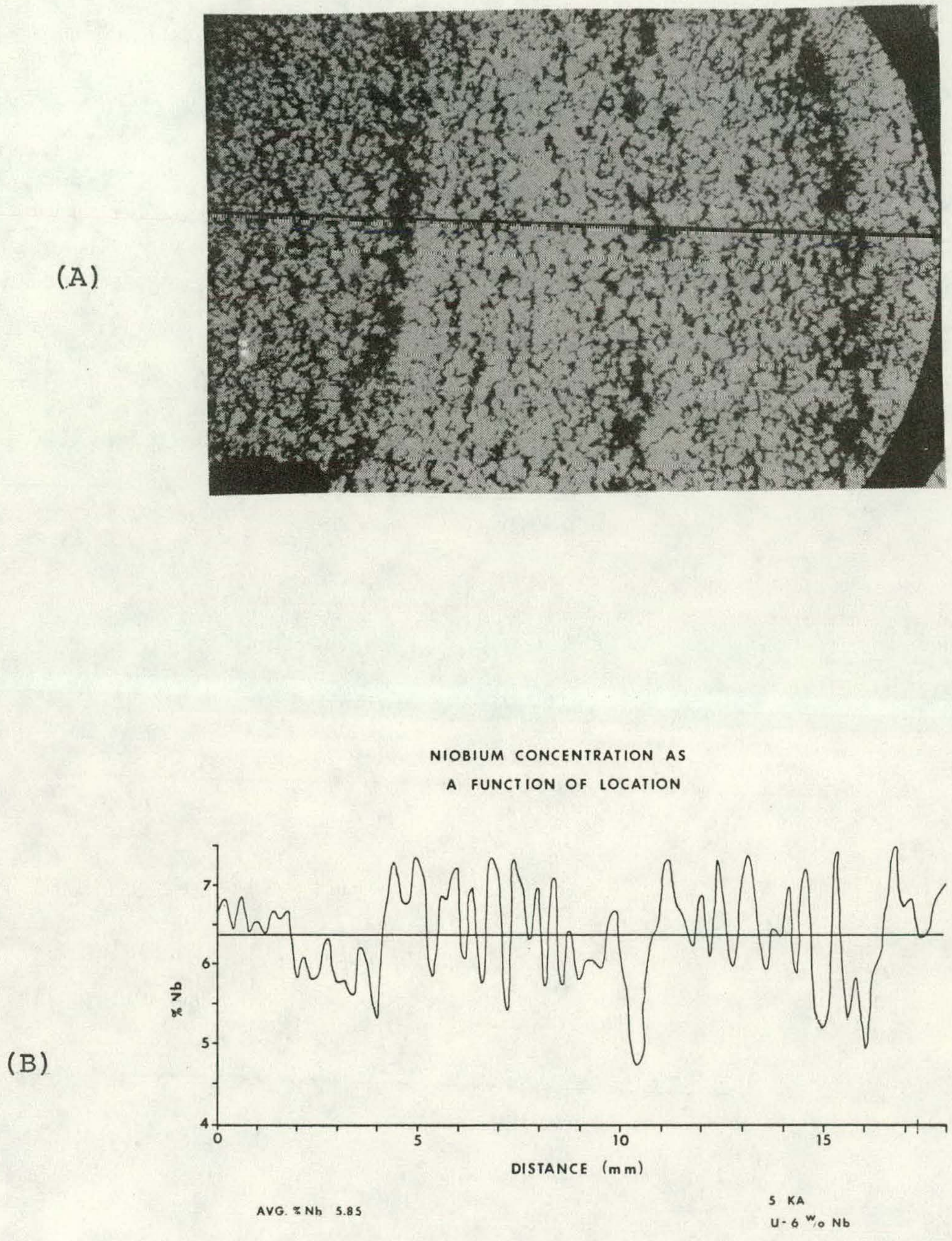

Figure 14: (A) Photomacrograph of Solute Band Segregation at 5 kA

(B) Nb Concentration vs. Distance for a Scan Along Line Shown in (A)

(A)

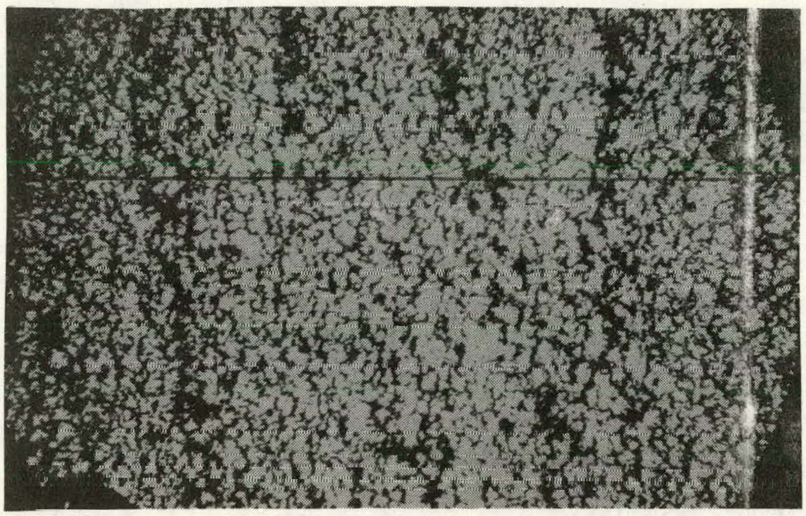

(A)

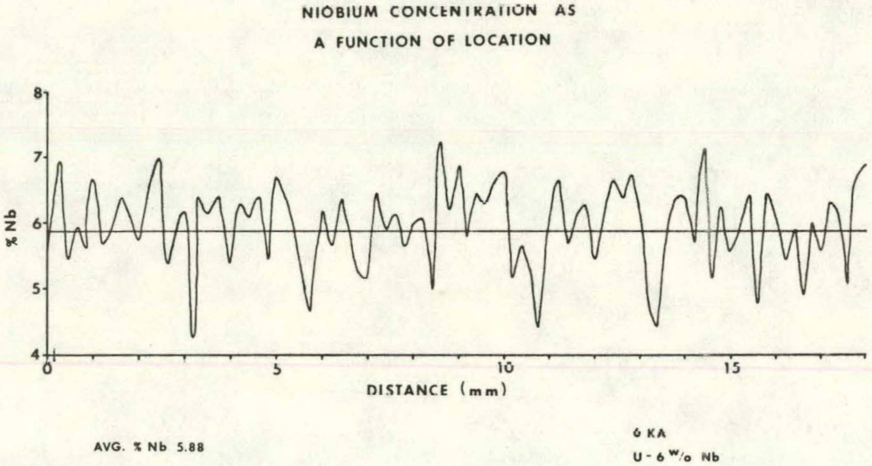

Figure 15: (A) Photomacrograph of Solute Band Segregation at 6kA

(B) Nb Concentration vs. Distance for a Scan Along the Line Shown in (A)

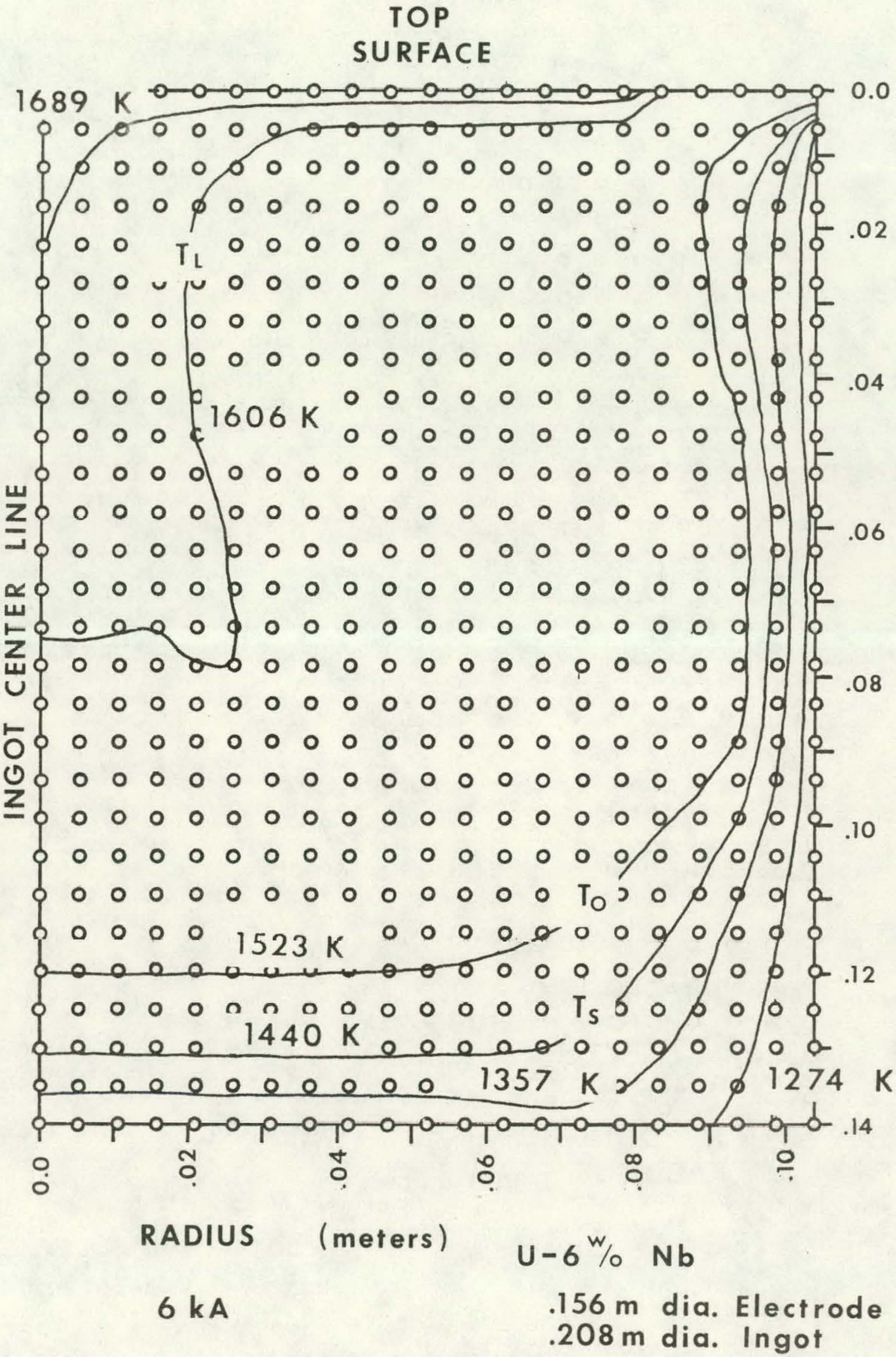

Figure 16: Isotherm Plot for Ingot Section Melted at 6 kA

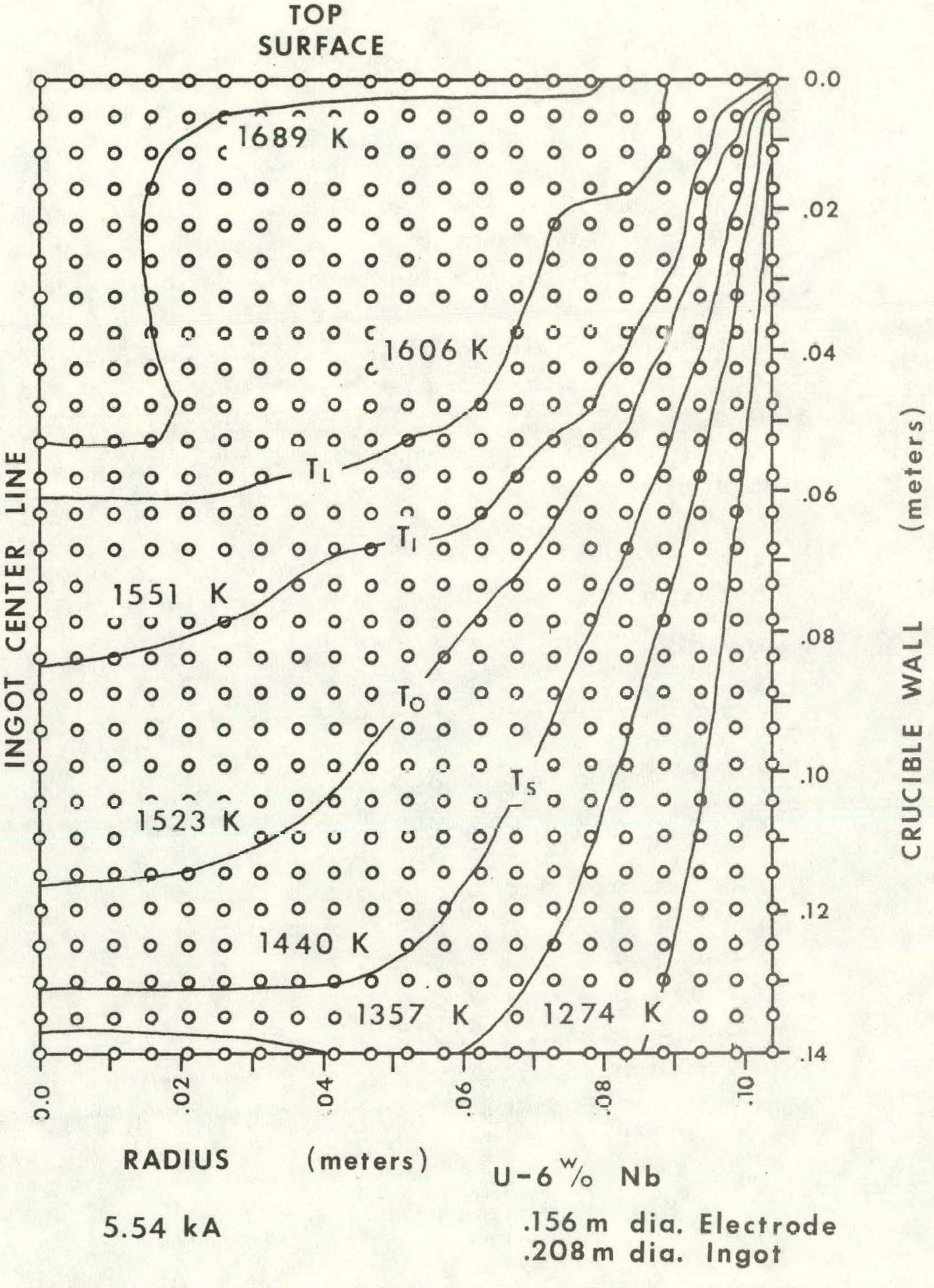

Figure 17: Isotherm Plot for Ingot Section Melted at 5.54 kA

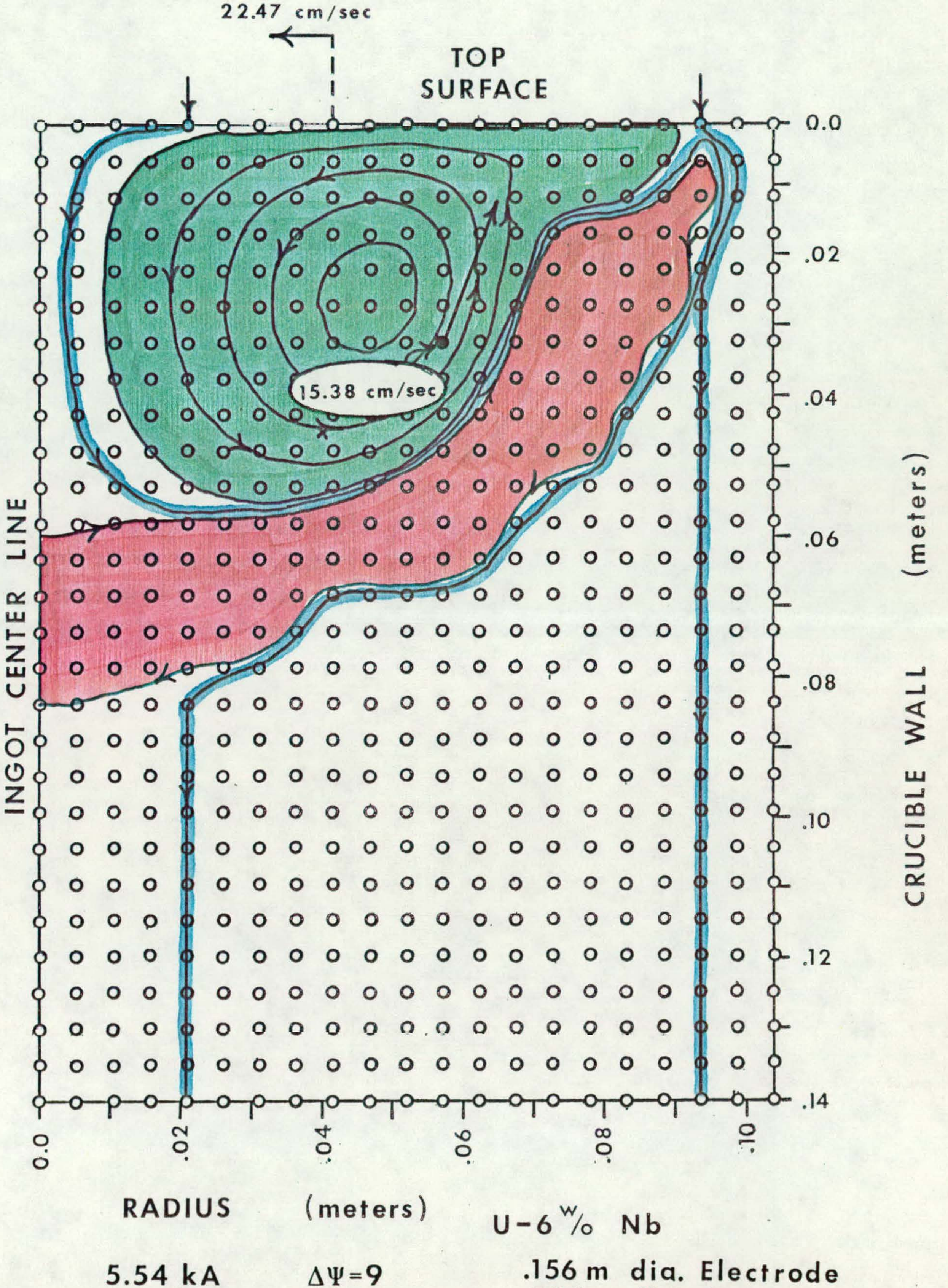

Figure 18: Streamfunction Plot for Ingot Section Melted at 5.54 kA

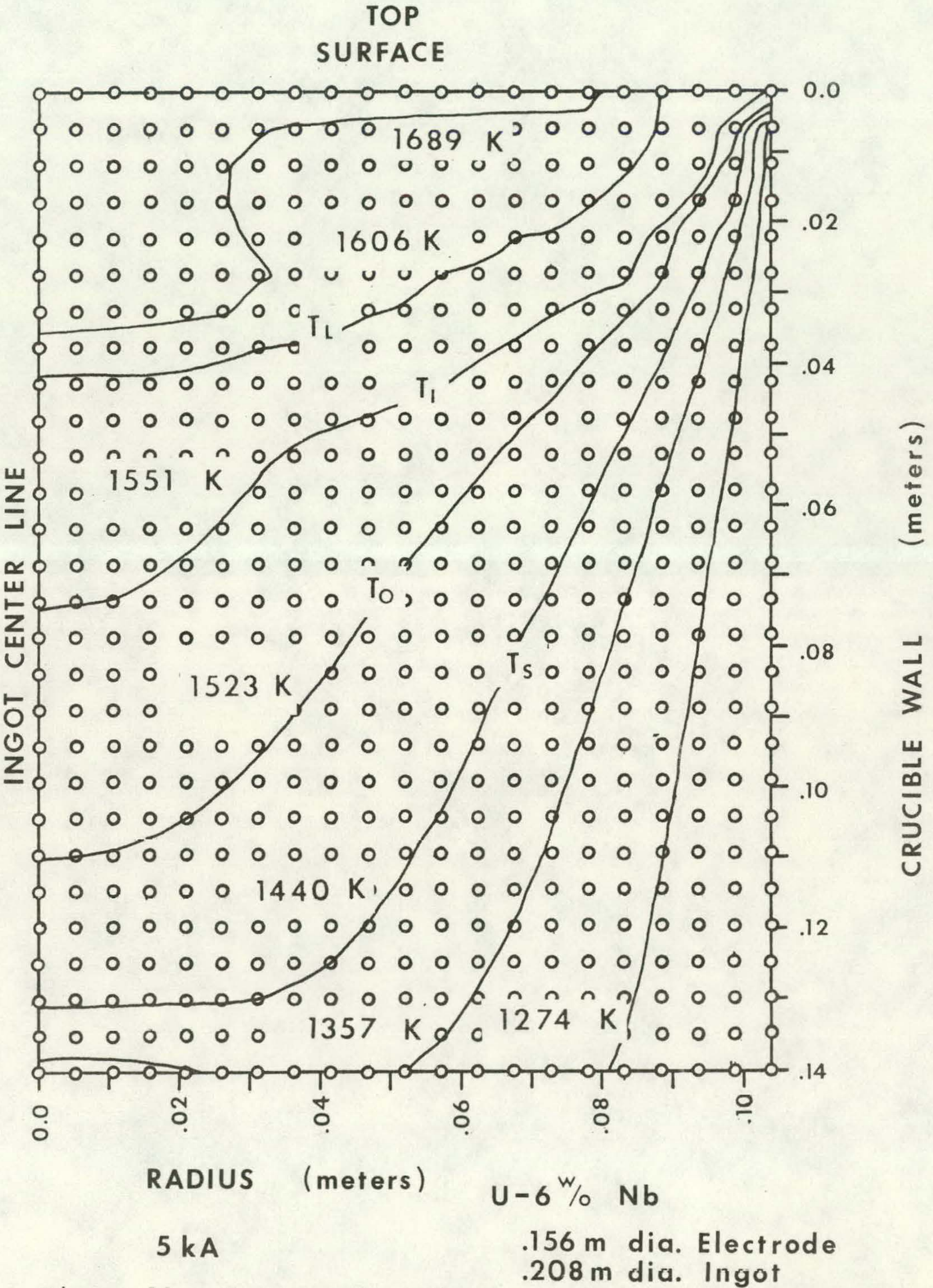

Figure 19: Isotherm Plot for Ingot Section
Melted at 5 kA

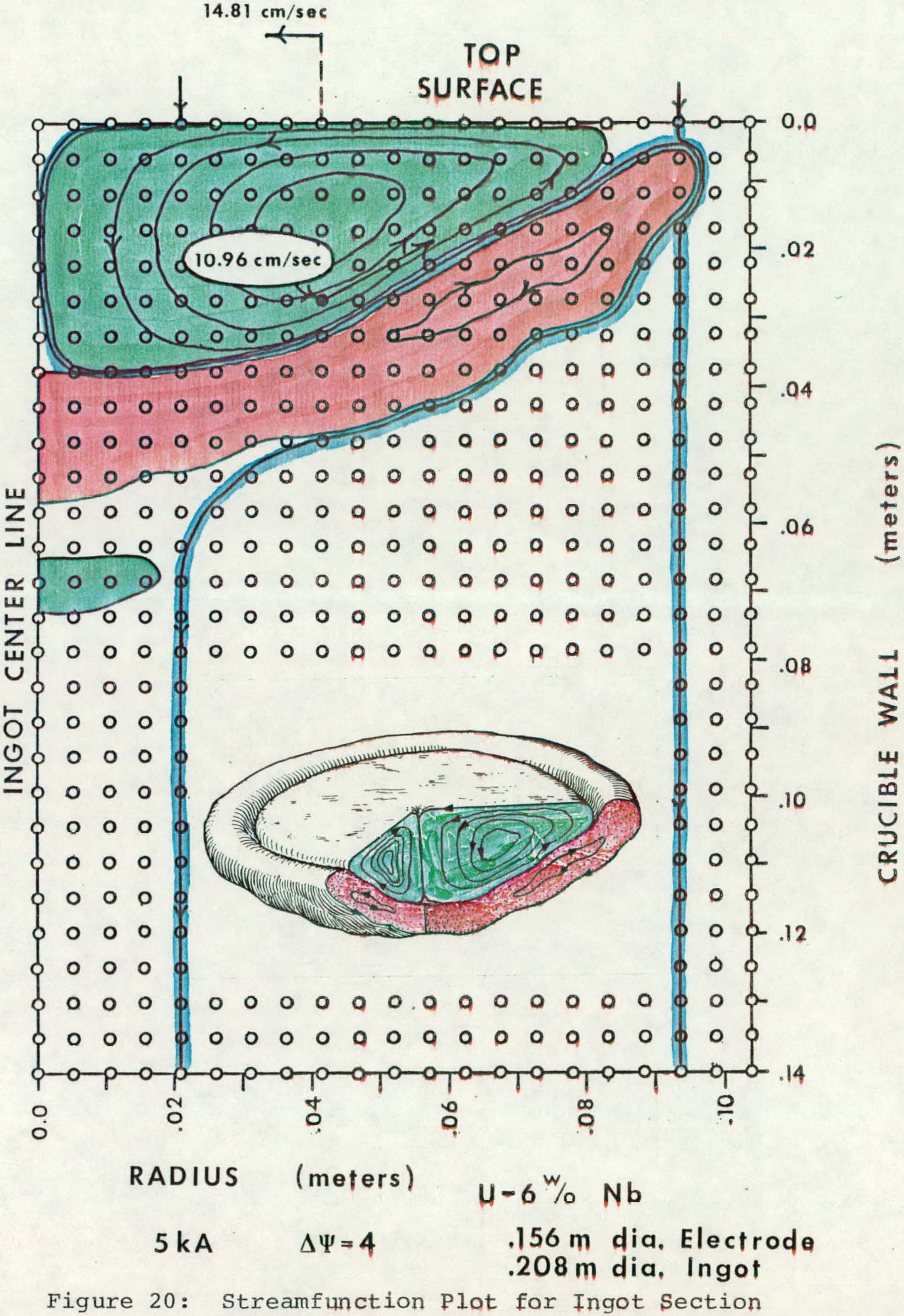

Figure 20: Streamfunction Plot for Ingot Section Melted at 5 kA

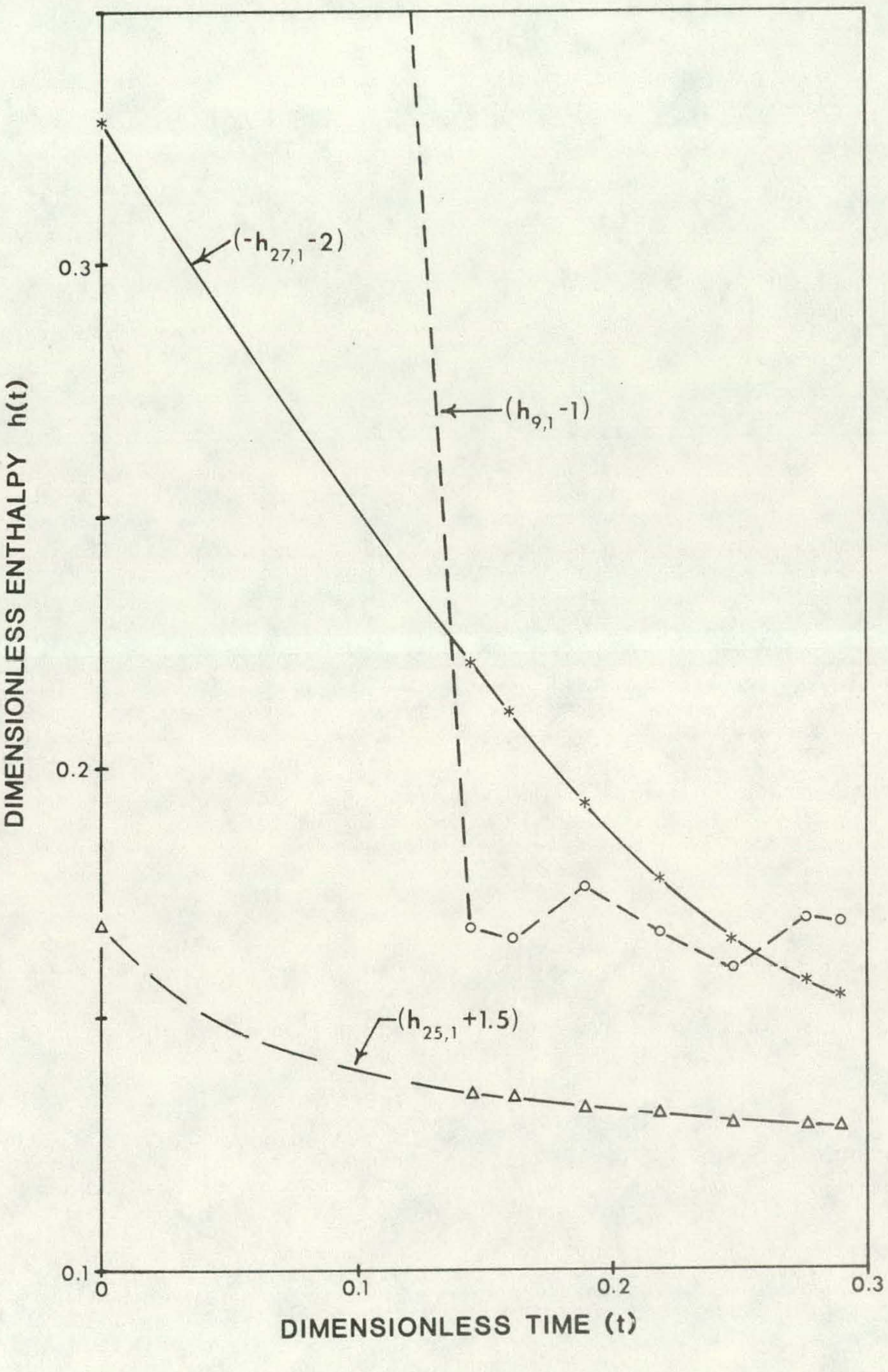

Figure 21: Approach to Steady State as Indicated by Plotting Dimensionless Enthalpy vs. Dimensionless Time for the 5 kA Condition

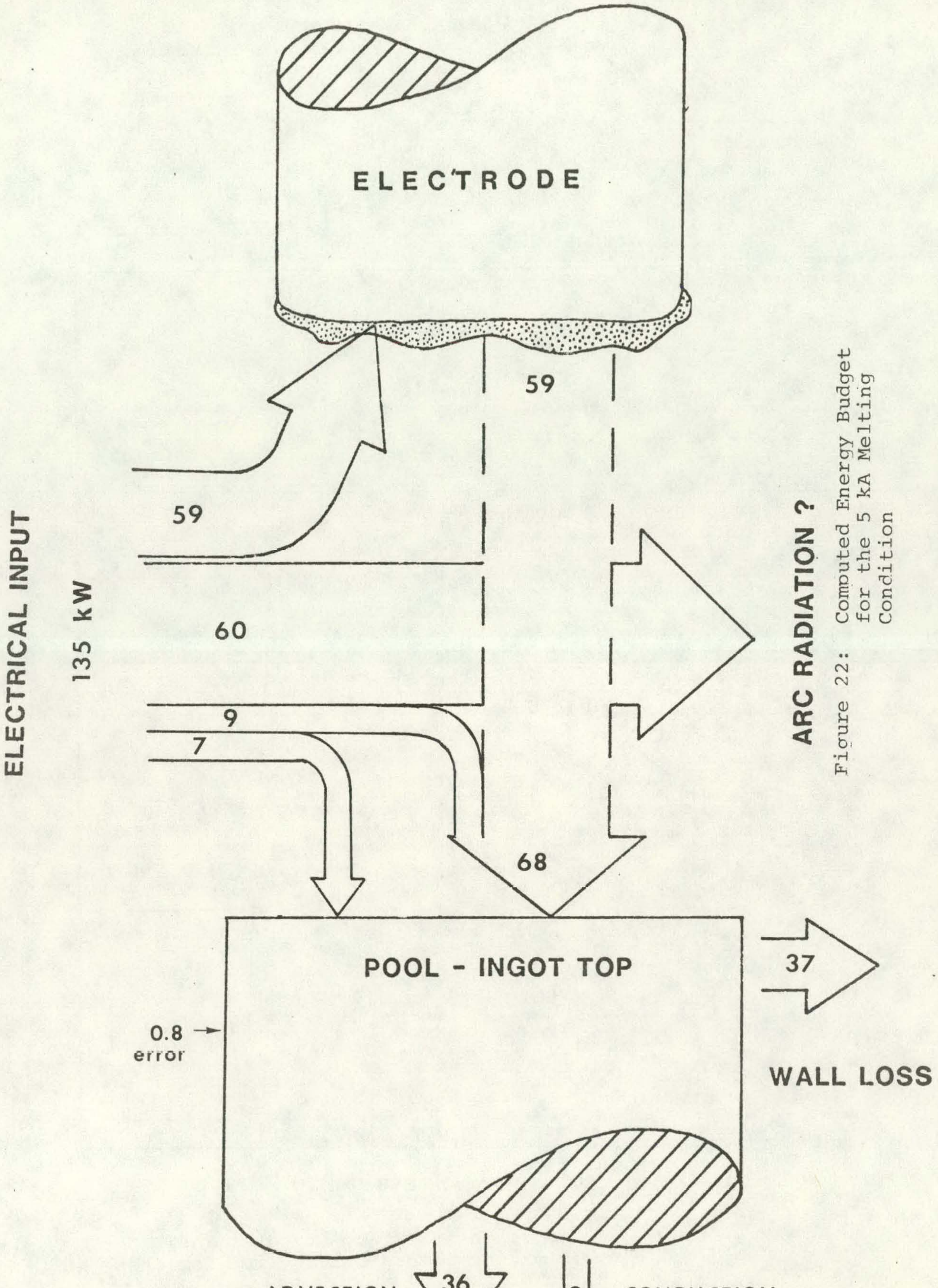

Figure 22: Computed Energy Budget for the 5 kA Melting Condition

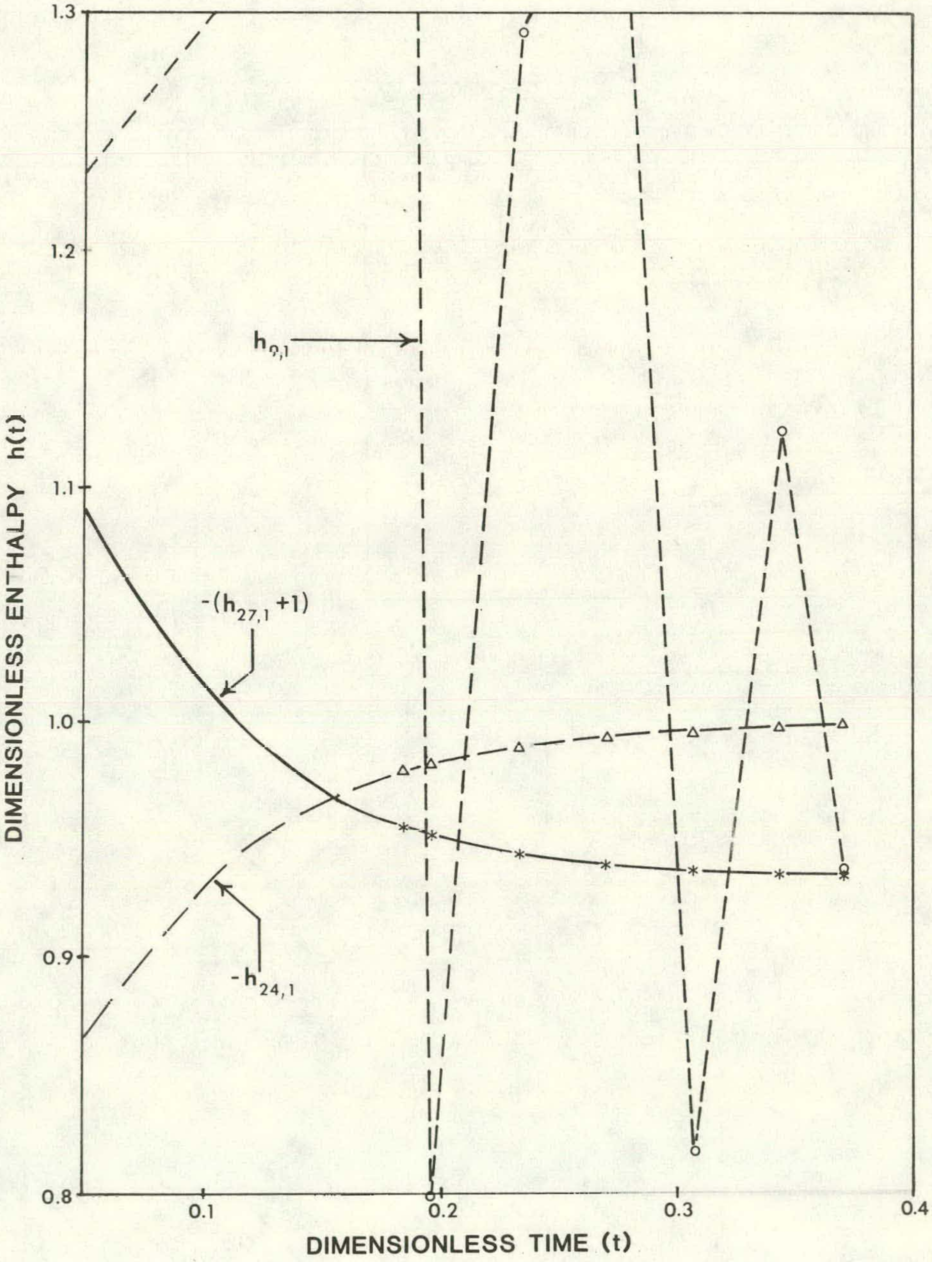

Figure 23: Approach to Steady State as Indicated by Plotting Dimensionless Time for the 4 kA Condition

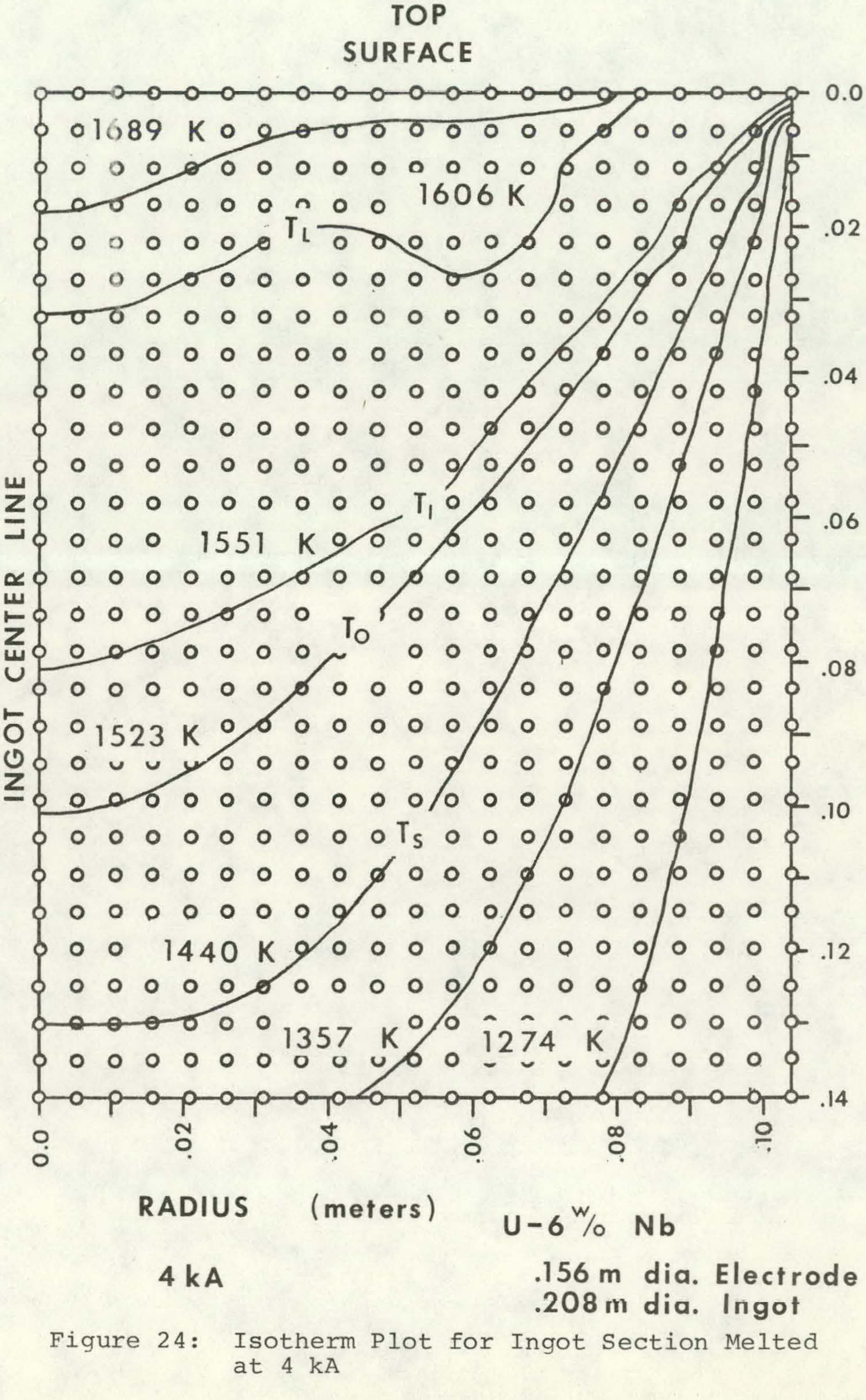

Figure 24: Isotherm Plot for Ingot Section Melted at 4 kA

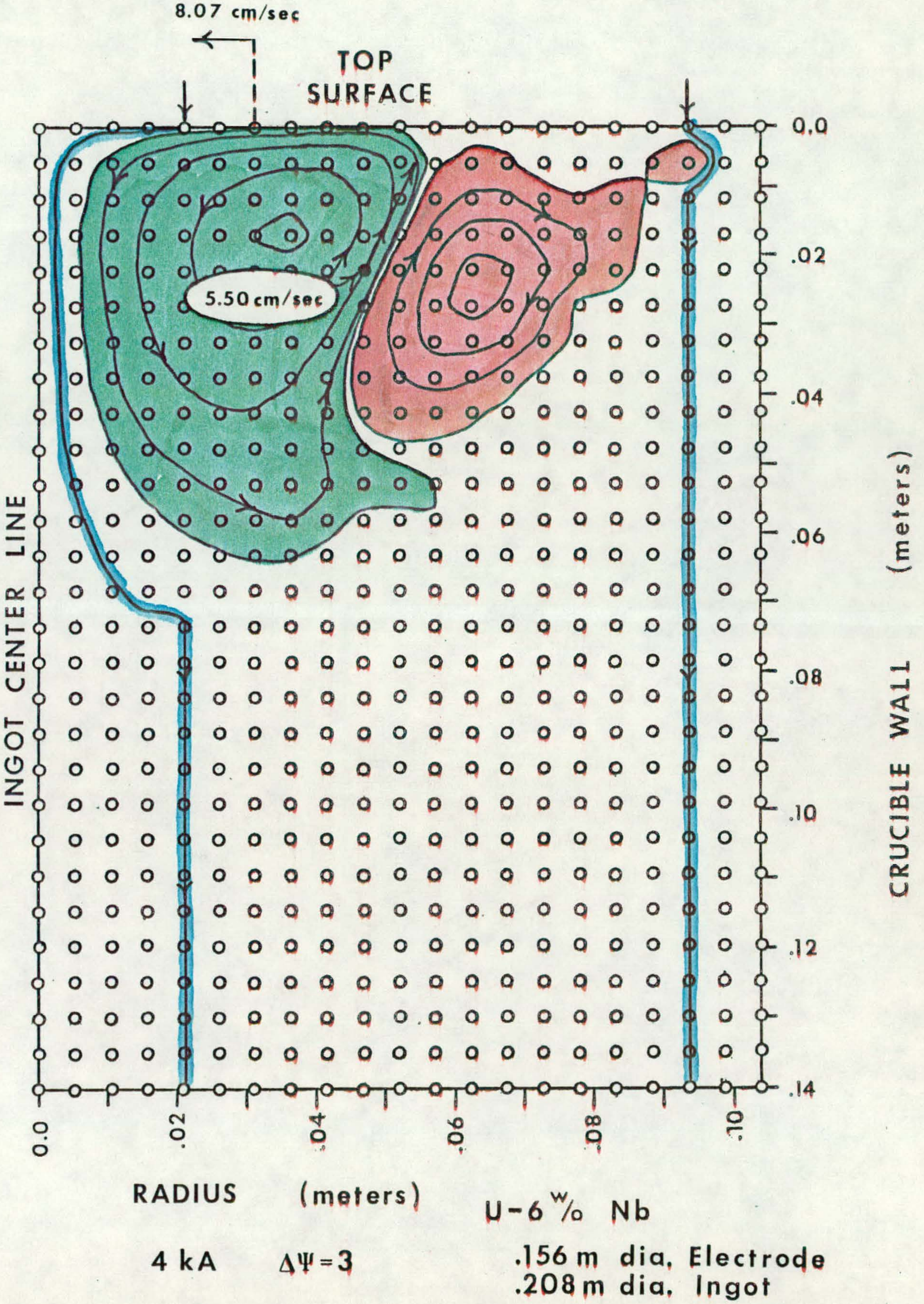

Figure 25: Streamfunction Plot for Ingot Section Melted at 4 kA

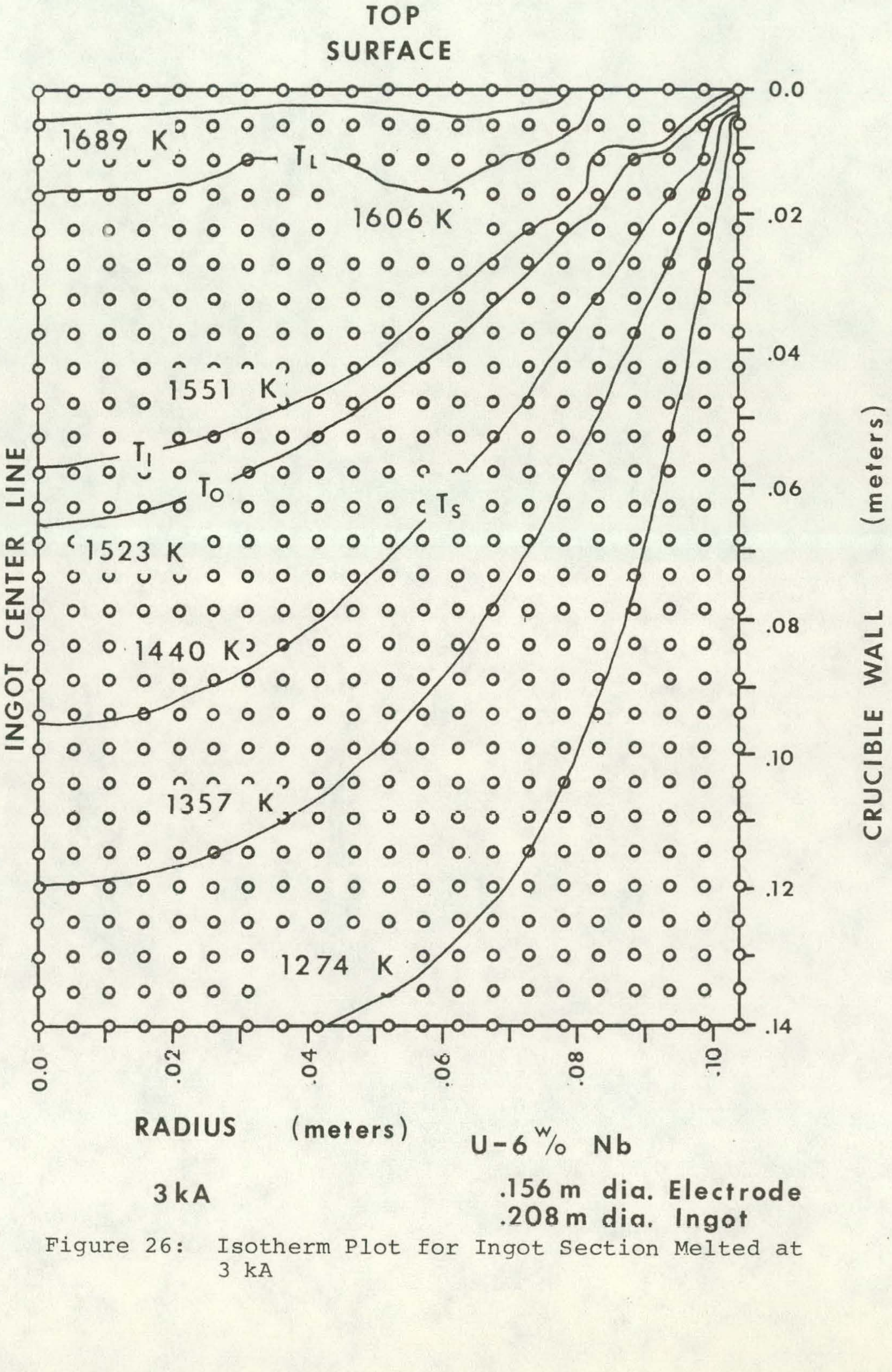

Figure 26: Isotherm Plot for Ingot Section Melted at 3 kA

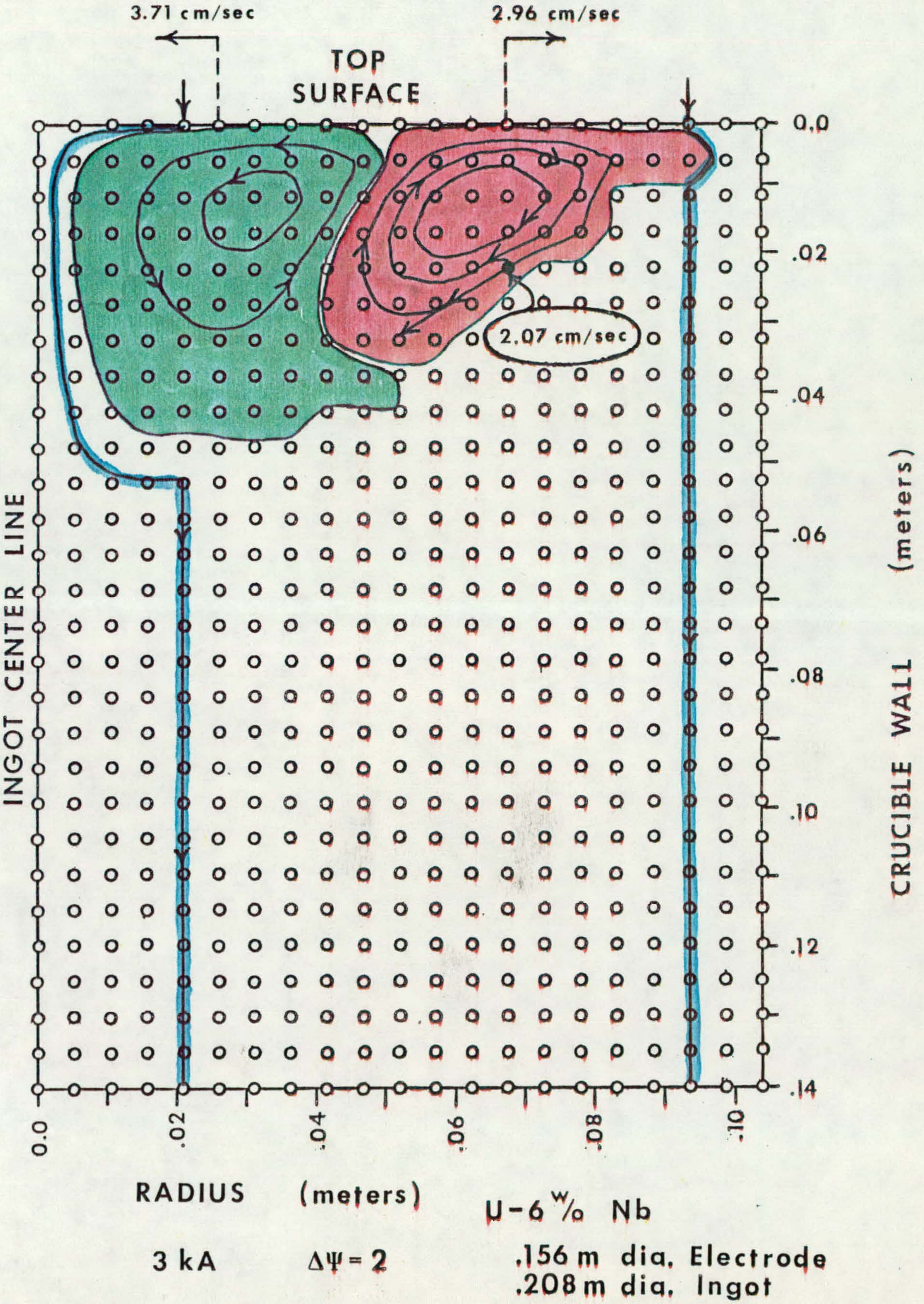

Figure 27: Streamfunction Plot for Ingot Section Melted at 2 kA

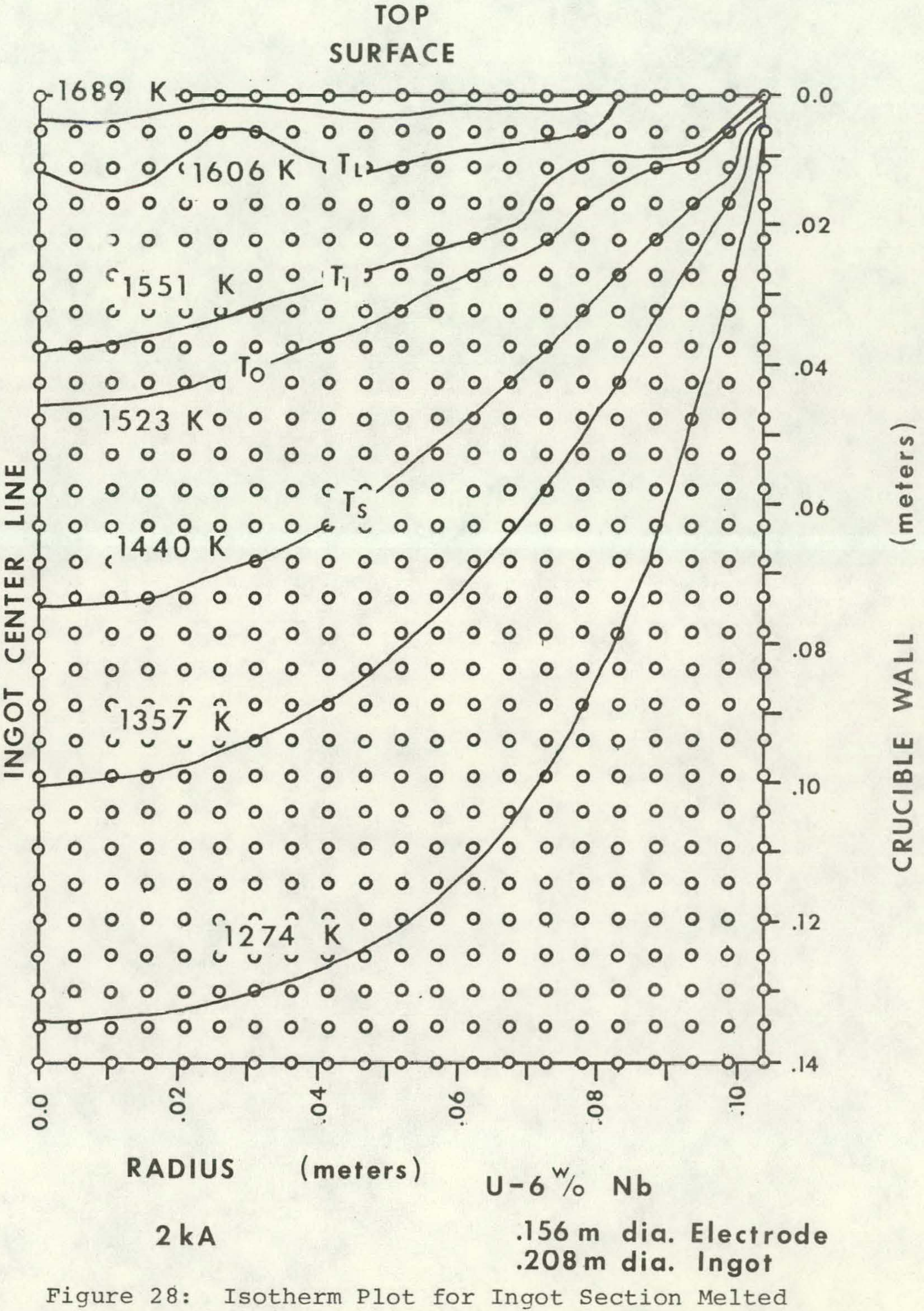

Figure 28: Isotherm Plot for Ingot Section Melted at 2 kA

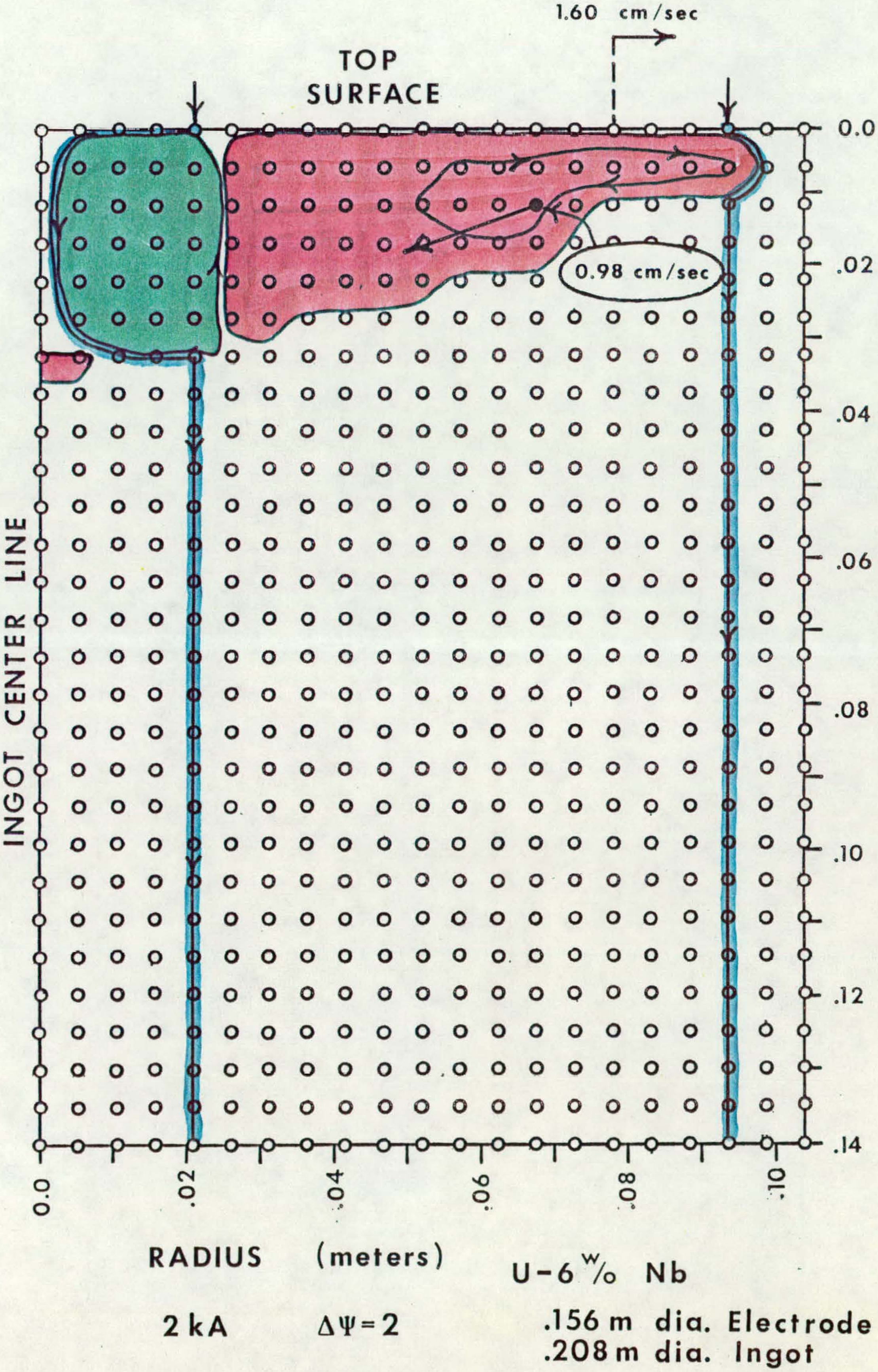

Figure 29: Streamfunction Plot for Ingot Section Melted at 2 kA

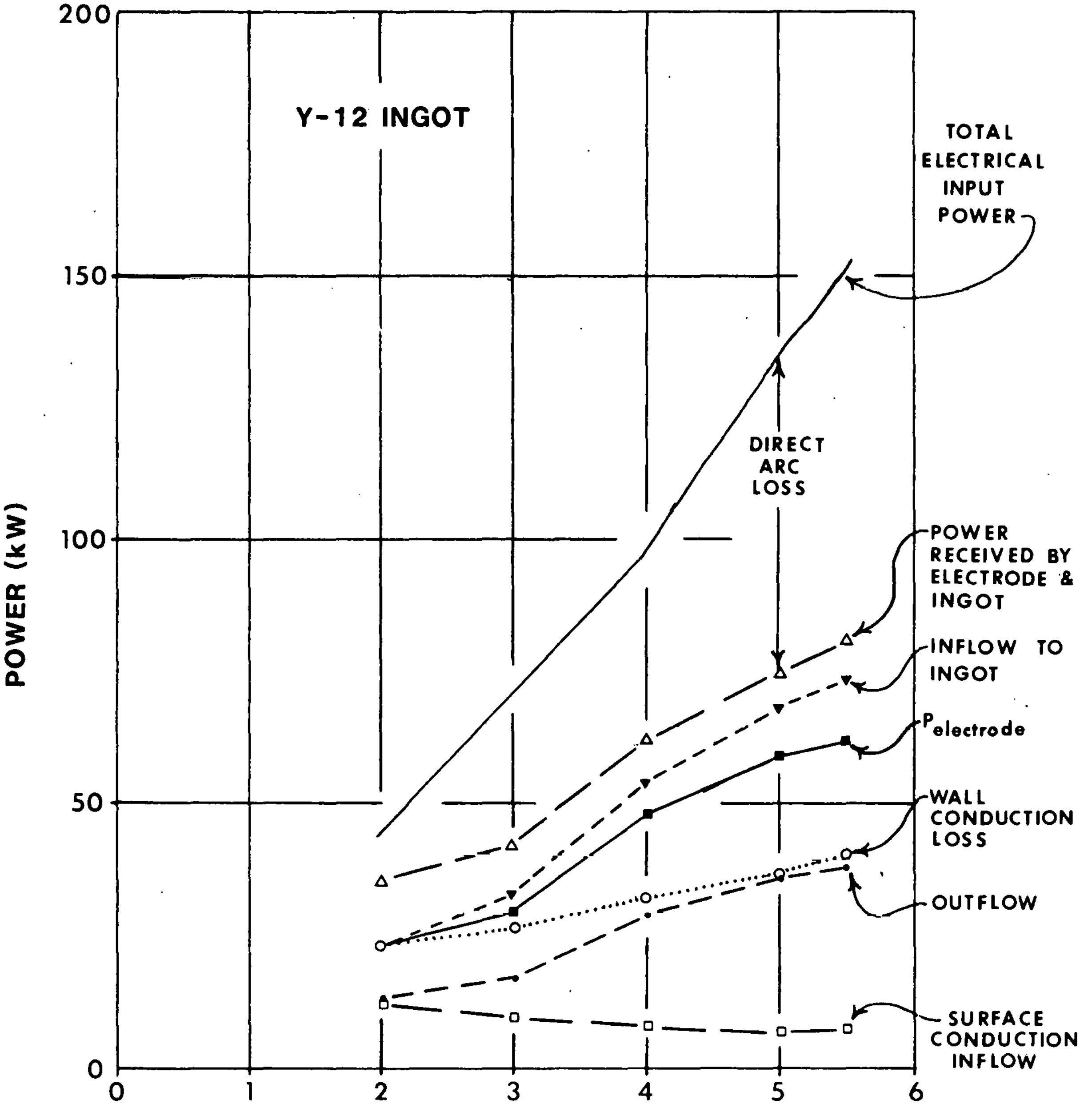

Figure 30: Compilation of Computed Energy Budgets As a Function of Melting Current

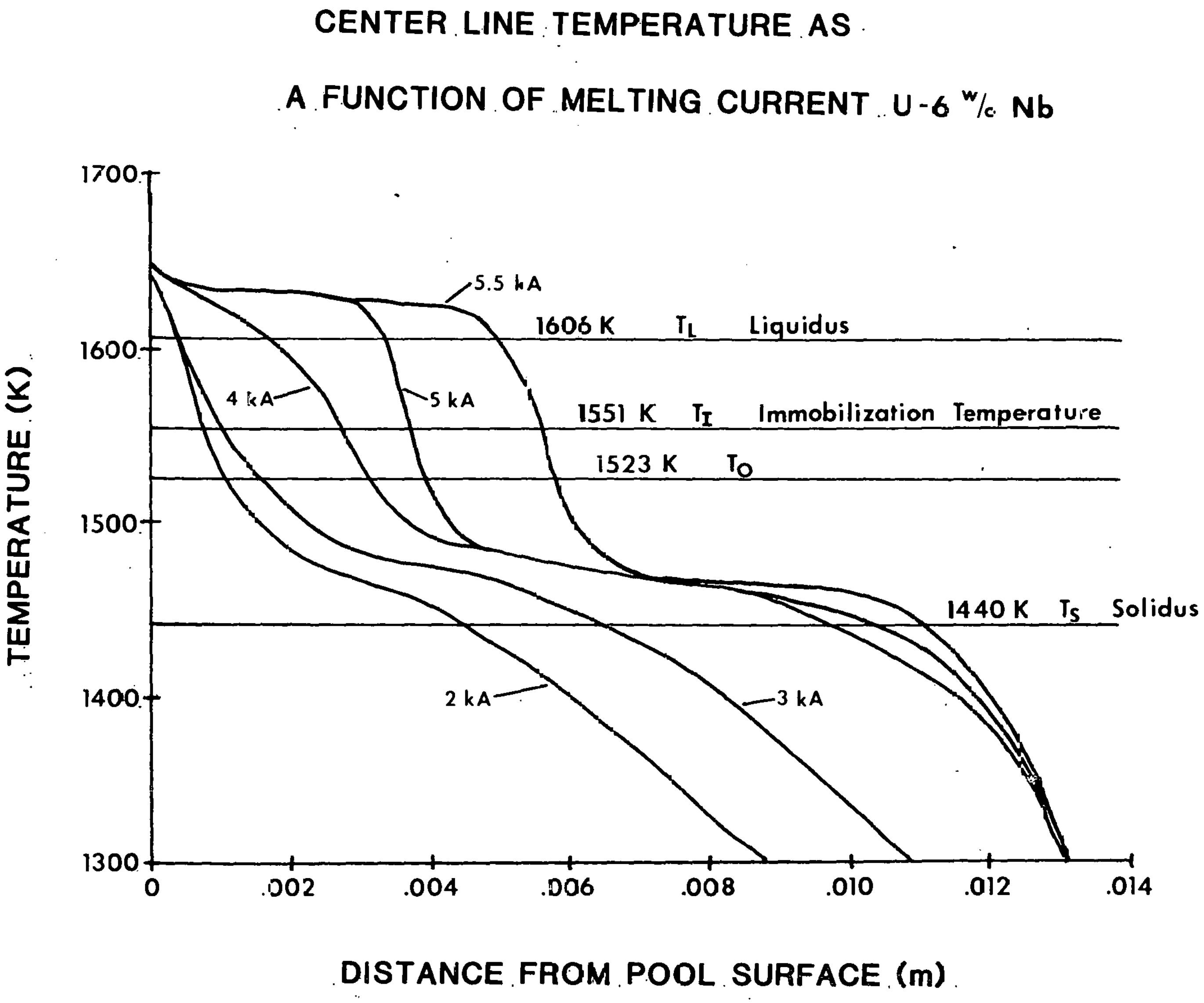

Figure 31: Ingot Centerline Temperature as a Function of Distance from the Pool Surface for Current Levels 2, 3, 4, 5 and 5.5 kA

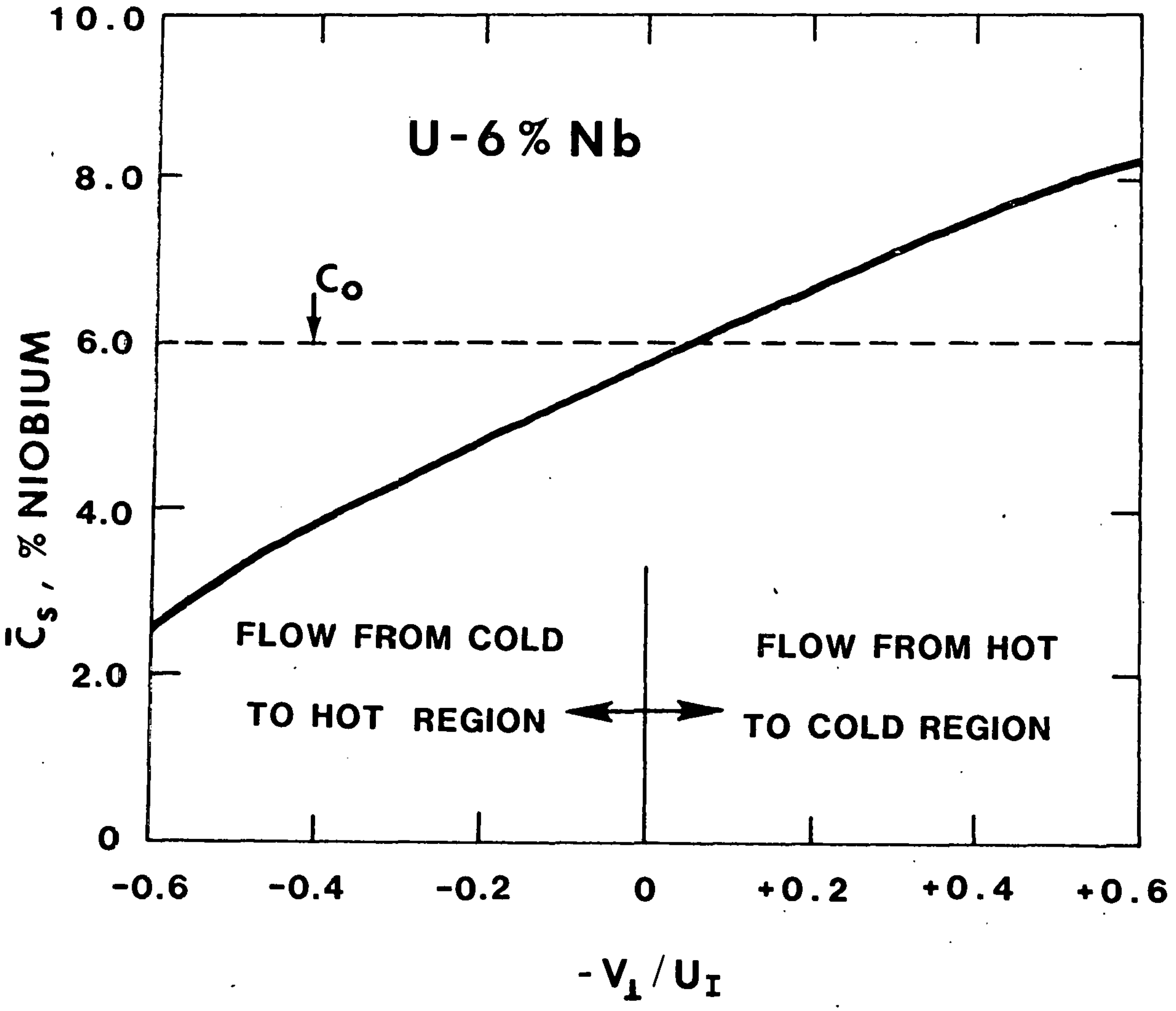

MACROSEGREGATION

Figure 32: Macrosegregation for U-6w/o Nb Nominal Alloy Under Conditions of Unidirectional Solidification

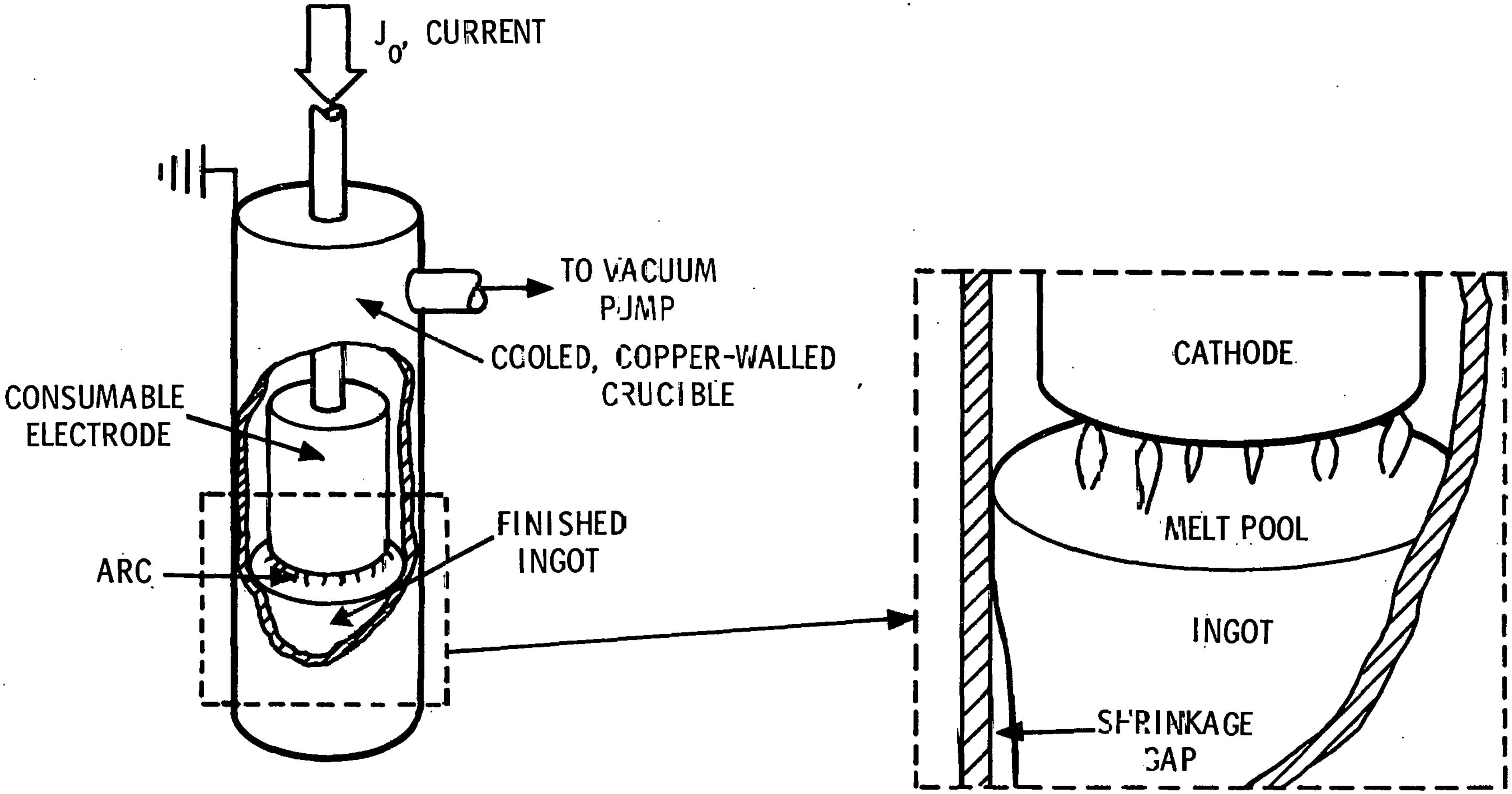

Figure A1: (A) Schematic Diagram of the Vacuum Consumable Arc Remelt Process

(B) Cut Away of the Arc Zone

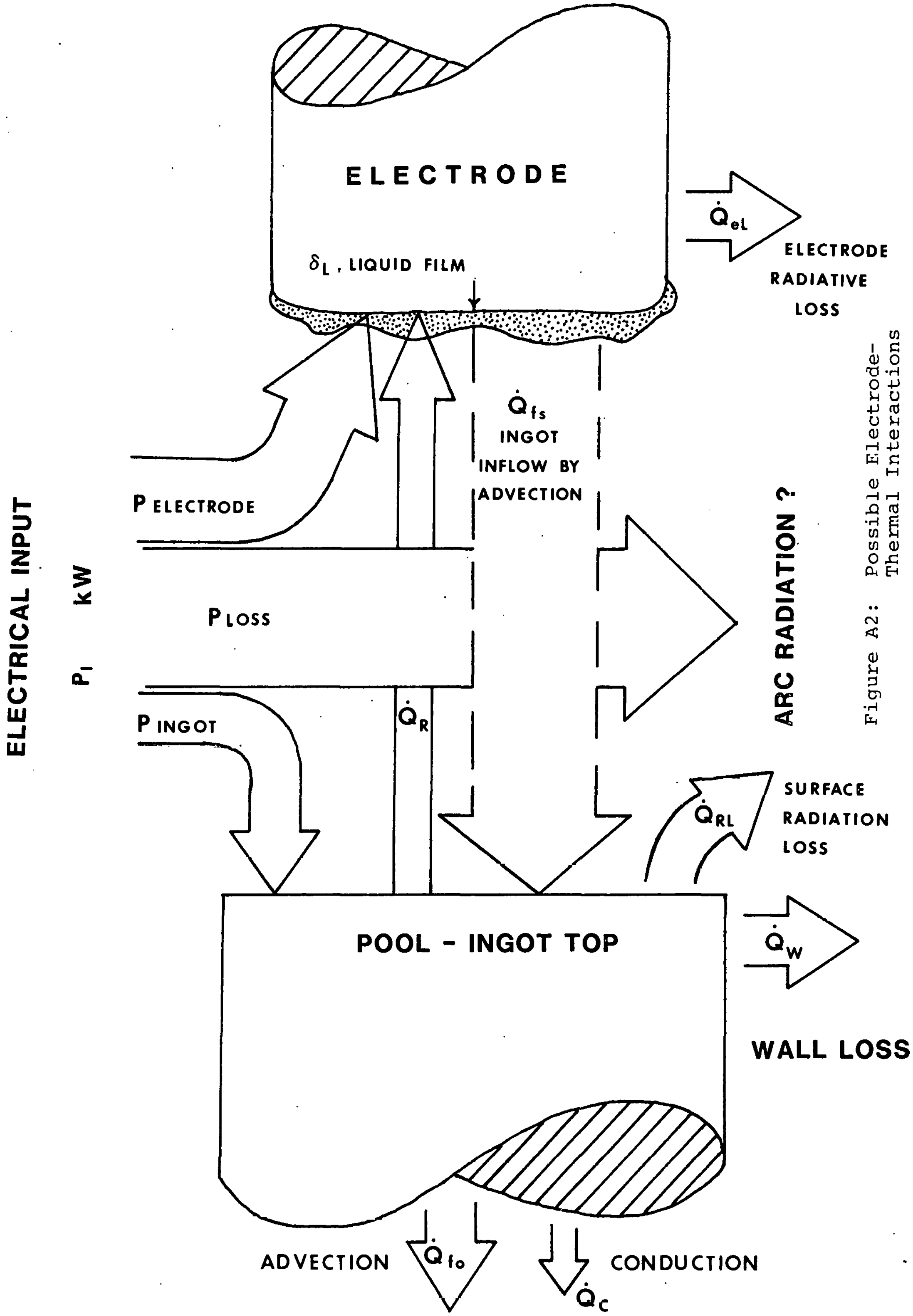

Figure A2: Possible Electrode-Thermal Interactions

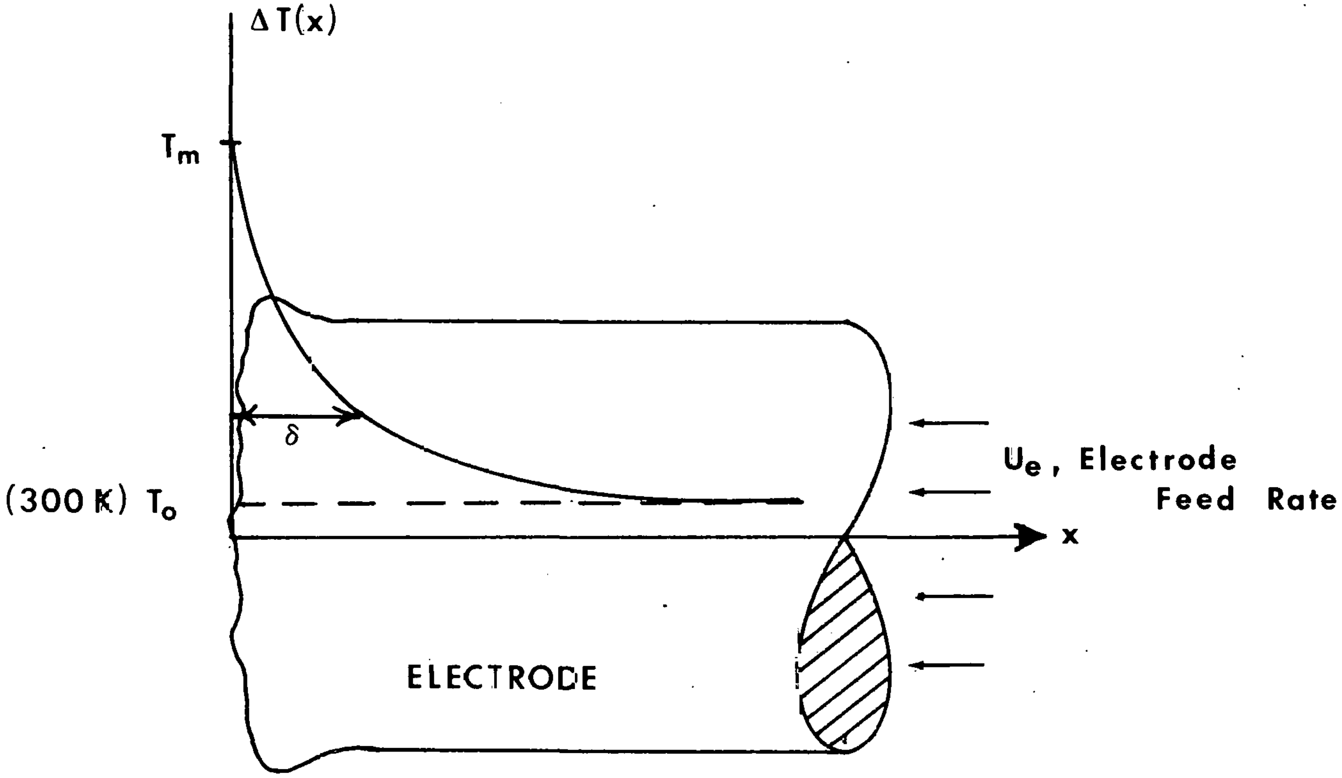

Figure A.3. Electrode at Quasisteady Melt Conditions

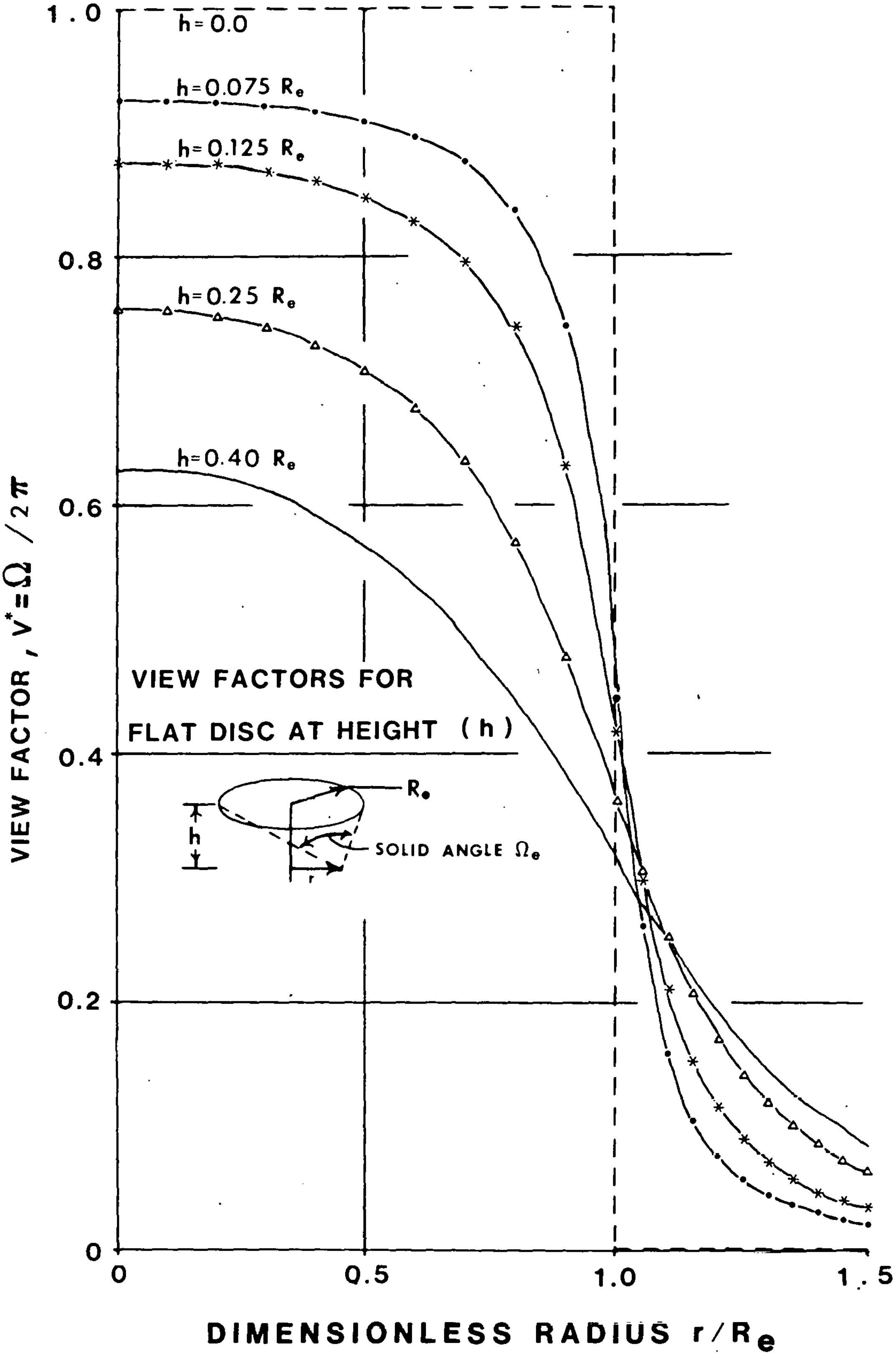

Figure A4: Electrode Viewfactor from Pool Surface

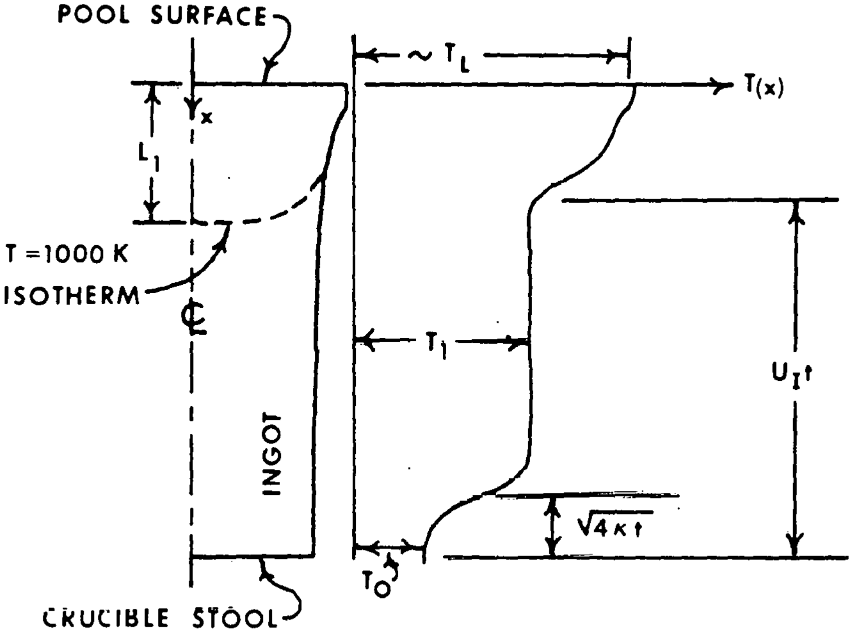

Axial Temperature T(x) in Ingot (Schematic).

$U_I t > \sqrt{4\kappa t}$ for $t > t^* = 4\kappa/U_I^2 \simeq 40s$.

Figure A5: Schematic of Ingot Centerline Temperature as a Function of Distance from Pool Surface

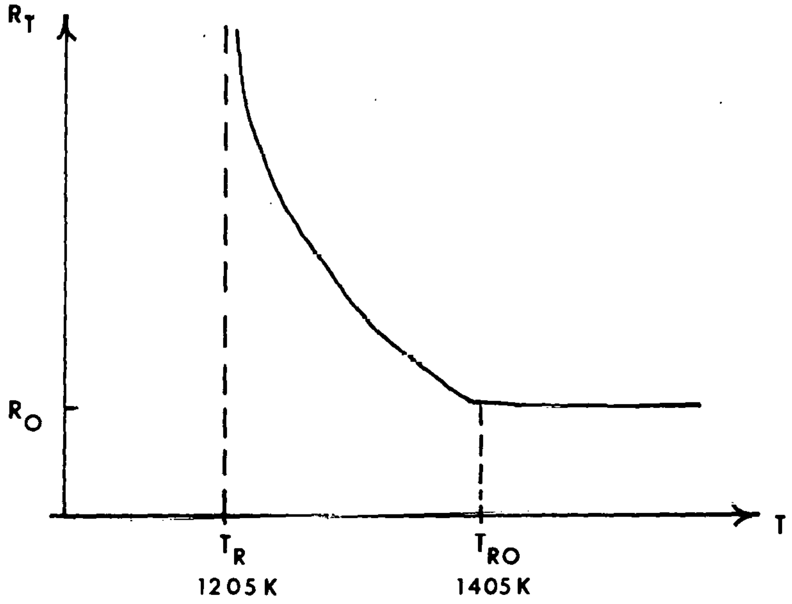

Figure A6: Schematic of Contact Thermal Resistance at the Ingot Crucible Wall as a Function of Temperature

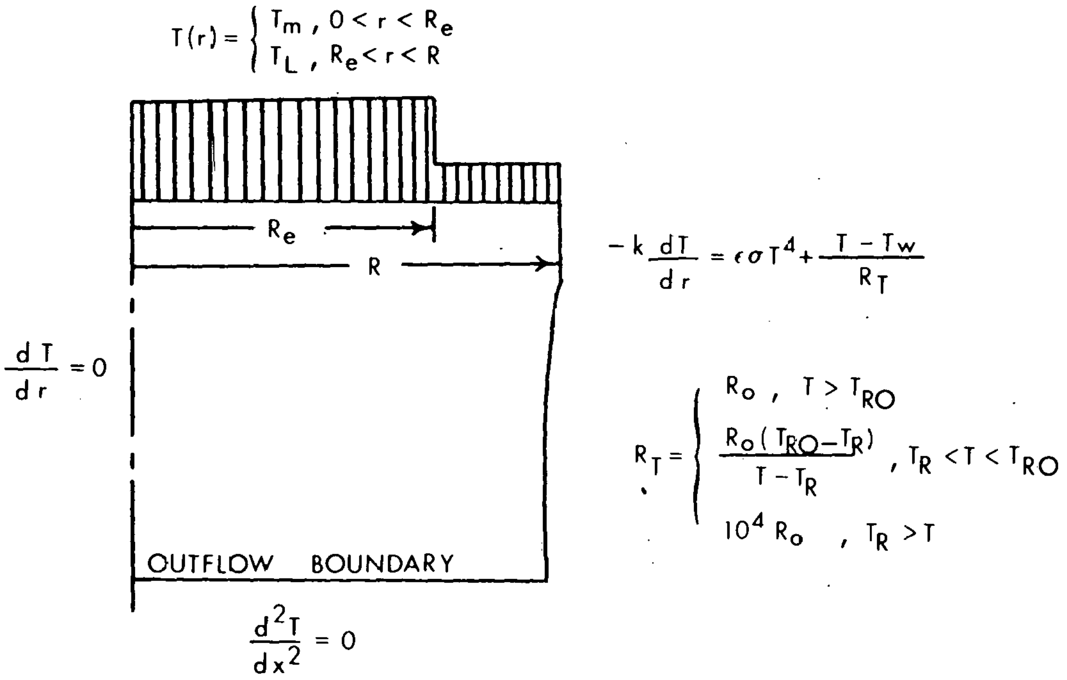

Figure A7: Thermal Boundary Condition Summary

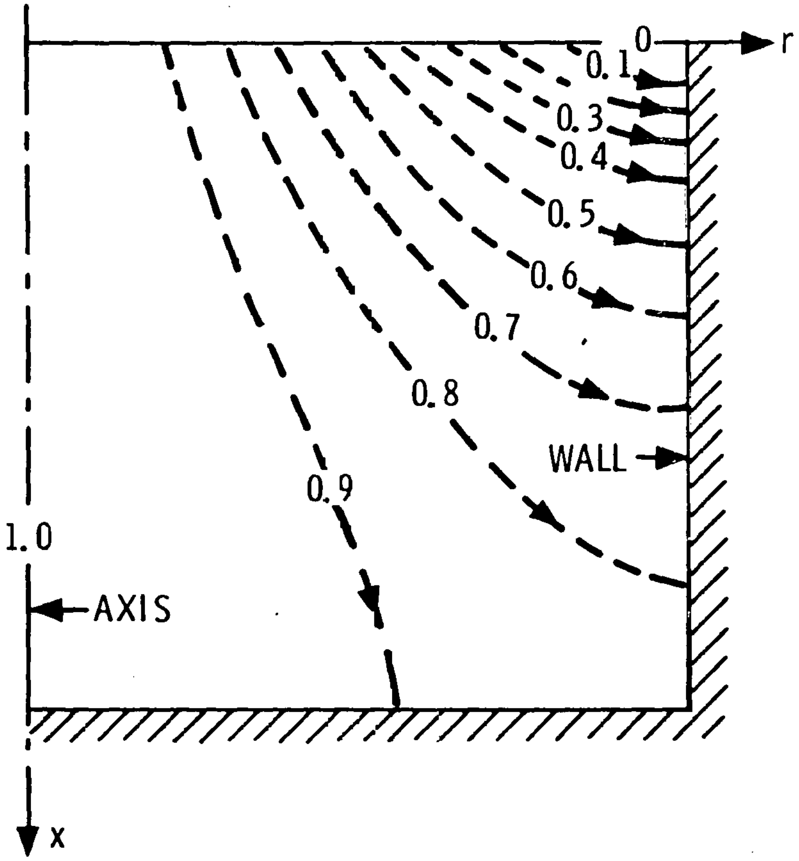

Figure A3: Current Streamlines for Aspect Ratio = 1.0

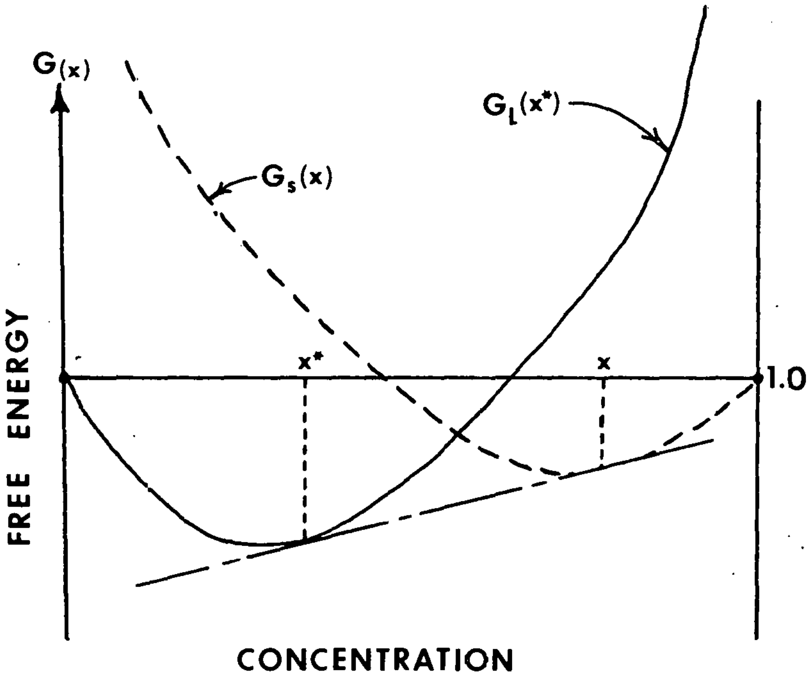

Figure A9: Tangent Rule of Phase Equilibrium

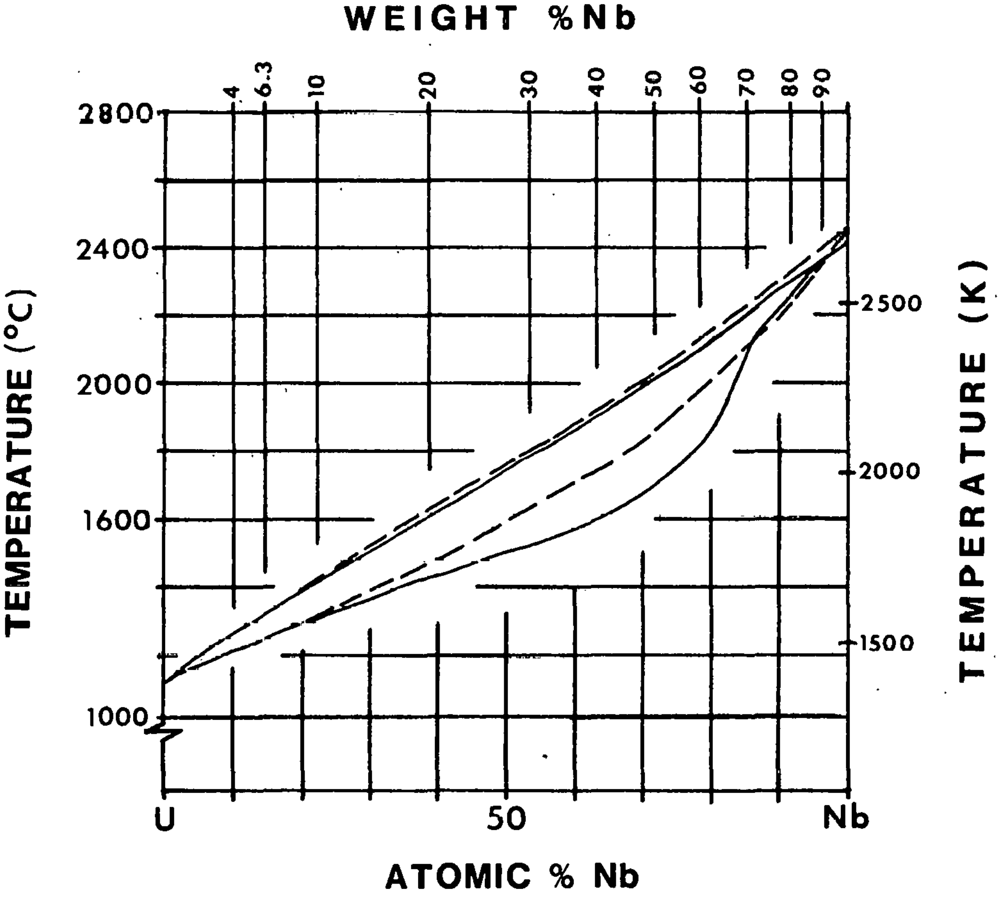

Equilibrium Phase Diagram. ——— Elliott
First Supplement---Present Work

Figure A10: Calculated U-Nb Equilibium Phase
Diagram

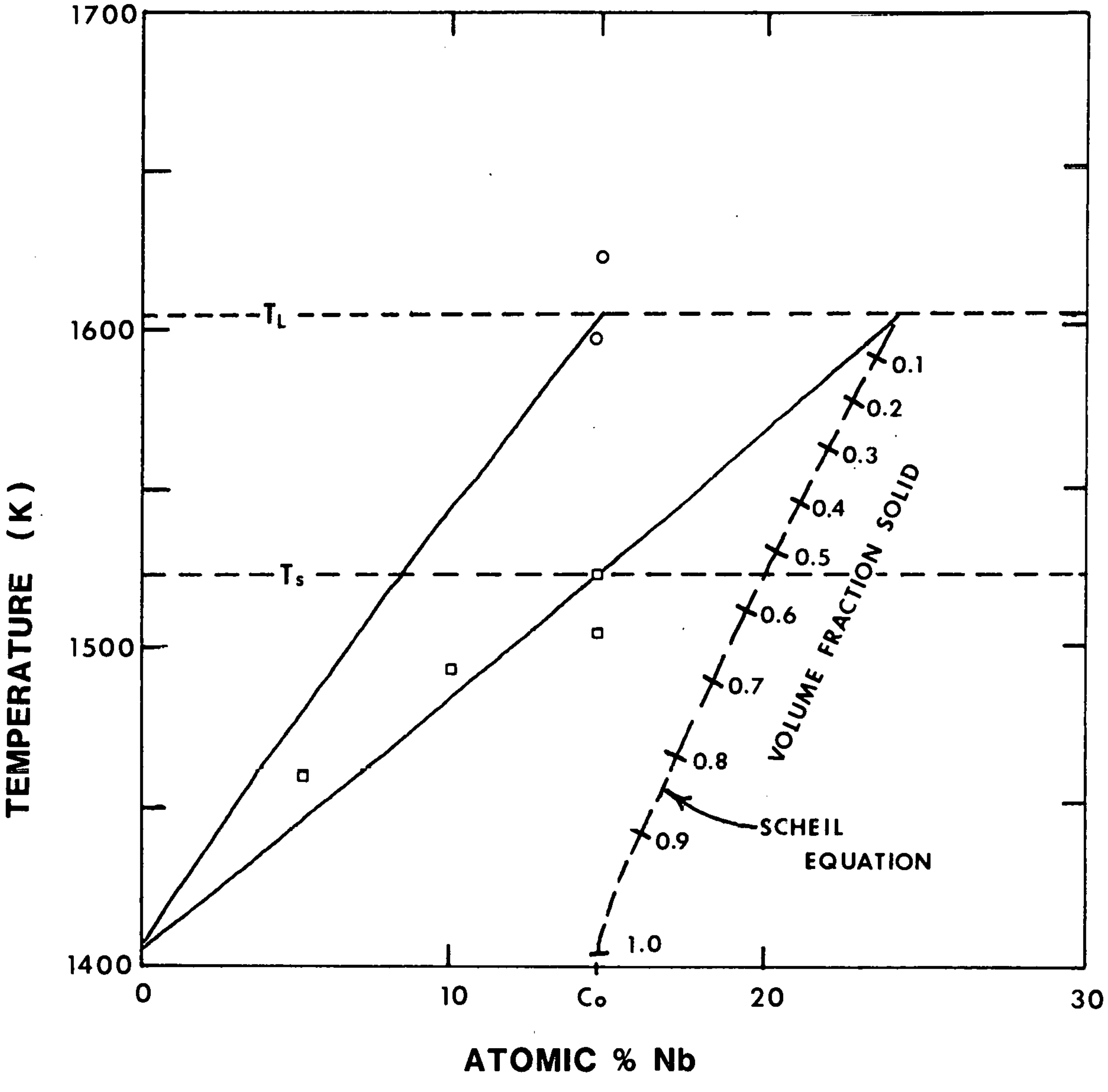

Figure A11
Phase Diagram detail for U-6.3w/oNb alloy. ____ Phase Diagram; -----Nonequilibrium Solidification (Scheil Equation); o Measured Liquidus; ▫ Measured Solidus.

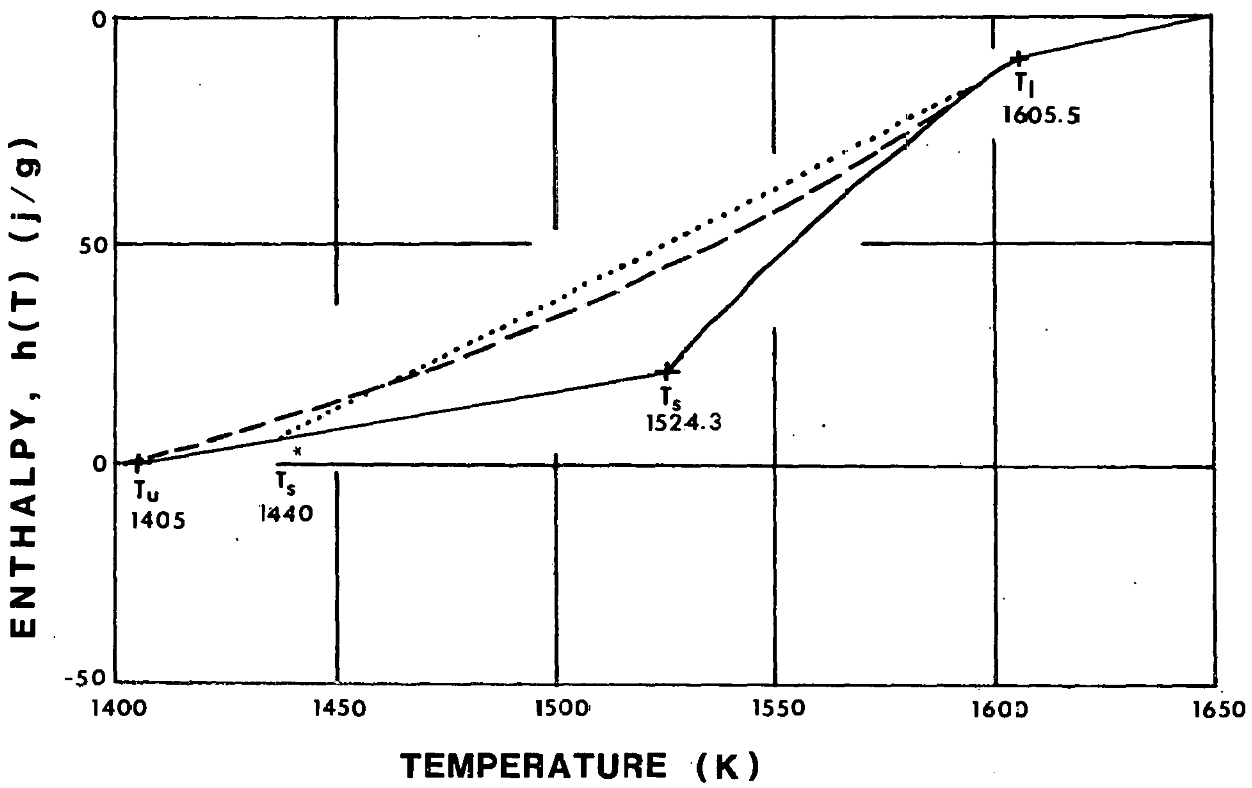

Figure A12

Enthalpy vs. Temperature. ——— h(T) for Equilibrium Phase Diagram; — — — h(T) for Scheil Nonequilibrium Solidification; .... h(T) Linear Fit to Scheil.

Table IV

Energy Budget Computations

POWER	COMPUTATION	SOURCE
P_I	$P_I = VJ_o$	Measured V, J_o
$P_{electrode}$	$= \dot{m}h(T_m)$	Measured $\dot{m}$, Theoretical $h(T)$
$\dot{Q}_w$		Output from Code
$\dot{Q}_{fo}$		
$\dot{Q}_c$		
$\dot{Q}_{fs}$		
P_{ingot}		
P_{loss}	$= P_I - P_{electrode} - P_{ingot}$	

TABLE V

L^{U} = 2400 cal/gm-mole	L^{Nb} = 4000 cal/gm-mole
C^{U}_{ps} = 0.1608 j/gm-K	C^{Nb}_{ps} = 0.3736 j/gm-K
C^{U}_{pL} = 0.1977 j/gm-K	C^{Nb}_{pl} = 0.3871 j/gm-K
T^{U} = 1405 K	T^{Nb} = 2740 K

Distribution:

Union Carbide Corp.
Y-12
P. O. Box Y
Oak Ridge, TN 37830
Attn: W. Dodsen
N. C. Jessen
D. Beck
J. Koger

Rockwell International
Atomics International Division
Rocky Flats Plant
P. O. Box 464
Golden, CO 80401
Attn: Bob Krenzer

Dr. Robert R. Mehrabian
Materials Science and
Standards Division
National Bureau of Standards
B-264 Building 223
Washington, DC 20234

Cameron Iron Works
P. O. Box 1212
Houston, Texas
Attn: N. A. Wilkinson

Oregon Metallurgical Corp.
P. O. Box 580
Albany, Oregon 97321
Attn: George J. Dooley, III

Special Metals Corp.
New Hartford, N.Y. 13413
Attn: J. Pridgeon

J. L. Roberts
Lawrence Livermore Laboratories
University of California
P. O. Box 808
Livermore, CA 94550

Prof. K. E. Torrance
Sibley School of
Aeronautical Engineering
Cornell University
Ithaca, N.Y. 14853

Los Alamos Scientific
Laboratories
Box 1663
Los Alamos, N.M. 87554
Attn: J. Straw, WX-5
J. Wechsler, WX-DO
D. Sandstrom, CMB-6

Massachusetts Institute of Technology
Dept. of Materials Science and
Engineering
77 Massachusetts Ave.
Cambridge, MA 02139
Attn: M. Flemmings
J. Szekeley

1551	D. W. Ballard Attn: F. A. Husenkamp R. Feliciano
1556	S. A. Ingham Attn: G. S. Phipps F. M. Tamashiro
2600	L. E. Hollingsworth
2620	R. J. Detry
2640	J. L. Tischhauser
2646	M. R. Scott
2646	B. M. Marder
2646	A. H. Treadway
2646	E. A. Aronson
4244	G. W. McClure
5500	O. E. Jones
5510	D. B. Hayes
5511	D. K. Gaithing
5511	C. E. Hickox
5512	F. G. Blottner
5513	D. W. Larson
5530	W. Herrmann
5822	K. E. Eckelmeyer
5800	R. S. Claassen
5830	M. J. Davis Attn: R. W. Rohde, 5832 J. Jellison, 5833 D. Mattox, 5834 C. Karnes, 5835 R. Blewer, 5836
5836	J. L. Ledman
5836	F. M. Hosking
5836	R. W. Fisher
5836	A. Netz
5836	J. Maroone
5836	N. Zamora
5836	J. A. Rejent
5836	R. P. Wemple

Distribution: (Con't)

8120	W. E. Alzheimer
8310	D. M. Schuster
8331	R. J. Kei
8331	S. Margolis
8332	R. E. Huddleston
8334	R. Y. Lee Attn: H. D. Jones
5836	F. J. Zanner (4)
2646	L. A. Bertram (20)
3141	C. A. Pepmueller (5)
3151	W. L. Garner (3)
3154-3	R. P. Campbell For DOE/TIC (25)

Org.	Bldg.	Name	Rec'd by *	Org.	Bldg.	Name	Rec'd by *

* Recipient must initial on classified documents.